

Prediction of the Response Behaviour of One-Hit Detectors in Particle Beams

by
ROCHUS HERRMANN

Dissertation for the degree of
Doctor of Philosophy



DEPARTMENT OF PHYSICS AND ASTRONOMY
FACULTY OF SCIENCE AND TECHNOLOGY
AARHUS UNIVERSITY
AARHUS, DENMARK
APRIL 2012

© 2012 Rochus Herrmann
Department of Physics and Astronomy
Aarhus University
Ny Munkegade 120
DK-8000 Aarhus C
Email: rhe@phys.au.dk

Supported by:



This document was compiled and typeset in L^AT_EX 2_ε by the author.

This thesis has been submitted to the Faculty of Science and Technology at Aarhus University in partial fulfilment of the requirements for obtaining a PhD degree in physics. The work has been carried out under the supervision of Søren Pape Møller at the Department of Physics and Astronomy.

Preface

This thesis presents parts of the work and research I have been conducting during my three year PhD project in the Aarhus Particle Therapy Group (APTG) at the Institut for Fysik og Astronomi (IFA).

The data presented in the article:

R. Herrmann, O. Jäkel, H. Palmans, P. Sharpe, and N. Bassler.
Dose Response of Alanine Detectors Irradiated with Carbon Ion
Beams. *Med Phys*, 38(4):1859 – 1866, 2011

have been collected during my studies at the University of Heidelberg and have been essential part of my Masters thesis. The main concepts for evaluation have also been developed there. However, since the article was written during my PhD studies in Aarhus it is listed in the *List of publications*. Nevertheless, in this thesis the content of this article is not discussed and it is referred to as to any other article in literature.



Rochus Herrmann

Aarhus, April 30th 2012

Contents

Contents	v
List of publications	viii
1 Introduction	1
1.1 Radiotherapy in cancer treatment	1
1.2 Radiotherapy with particles	3
1.3 The need for dosimetry	5
1.4 Outline of the thesis	6
2 Interaction of radiation with matter	7
2.1 Photon interactions with matter	7
2.2 Energy deposition of swift particles in matter	9
3 Basics of dosimetry	14
3.1 Particle fluence	14
3.2 Absorbed dose	14
3.3 Linear energy transfer	15
3.4 Relative biological effectiveness	16
3.5 Calorimetry	17
3.6 Ionisation chambers	17
3.7 Solid state detectors in particle beams	18
4 Amorphous track models	22
4.1 Basic assumptions	22
4.2 Target theory	24
4.3 The Butts and Katz model	25
4.4 The relative effectiveness for one-hit detectors	29
4.5 Model by Hansen and Olsen	30
5 The alanine detector	34
5.1 Detection mechanism	35
5.2 Dosimetric characteristics	37
5.3 The NPL alanine dosimeter	42
5.4 Literature data	43
6 Introduction to experiments	46

7 Proton irradiation	48
7.1 Methods	48
7.2 Results	50
7.3 Discussion	51
8 Experiments with stopping particles	53
8.1 Material and Methods	53
8.2 Results	60
8.3 Discussion	65
9 Calculation of detector response	70
9.1 Original Hansen and Olsen model	70
9.2 New implementation	70
9.3 Libamtrack	74
9.4 Lithium formate	75
10 Comparison: Model and Measurement	78
10.1 Alanine - own data	78
10.2 Lithium formate	80
10.3 Alanine response data from literature	81
11 Discussion	86
11.1 Comparison of the modified with the original model	86
11.2 Comparison of model calculations with experimental data	86
11.3 The definition of the relative effectiveness	93
11.4 Detector response prediction with ATMs	94
12 Applications	95
12.1 Ion therapy facility audit with alanine detectors	95
12.2 Estimation of the dose averaged LET with alanine	98
12.3 Analytic expression for the RE	103
13 Conclusions	109
Appendices	112
A Tables	113
A.1 Relative effectiveness of alanine in carbon ion beams	113
A.2 Relative effectiveness of alanine in proton beams	114
A.3 Results of the HIT audit study	115
A.4 Data from literature	116
B Track-structure formulations	119
B.1 Track extension formulae	119

<i>CONTENTS</i>	vii
Acknowledgements	121
Bibliography	123
Acronyms	139
List of Figures	141
List of Tables	143

List of publications

Publications directly related to this thesis

- I A. Ableitinger, S. Vatnitsky, **R. Herrmann**, N. Bassler, H. Palmans, P. Sharpe, O. Jäkel, S. Ecker, Chaudhri N., and D. Georg. Dosimetry auditing procedure with alanine dosimeters for particle therapy. *in preparation*, 2012.
- II **R. Herrmann**, O. Jäkel, H. Palmans, P. Sharpe, and N. Bassler. Dose Response of Alanine Detectors Irradiated with Carbon Ion Beams. *Med. Phys.*, 38(4):1859 – 1866, 2011.
- III **R. Herrmann**, S. Greilich, L. Grzanka, and N. Bassler. Amorphous track predictions in ‘libamtrack’ for alanine relative effectiveness in ion beams. *Radiat. Meas.*, 46(12):1551–1553, 2011.

Additional publications

- IV D. C. Hansen, A. Lühr, **R. Herrmann**, N. Sobolevsky, and N. Bassler. Recent Improvements in the SHIELD-HIT Code. *Int. J. Radiat. Biol.*, 88(1-2):195–199, 2012.
- V **R. Herrmann**, J. Carl, O. Jäkel, N. Bassler, and J. B. B. Petersen. Investigation of the dosimetric impact of a Ni-Ti fiducial marker in carbon ion and proton beams. *Acta. Oncol.*, 49(7):1160–4, 2010.
- VI J. N. Kavanagh, F. J. Currell, D. J. Timson, M. H. Holzscheiter, N. Bassler, **R. Herrmann**, K. M. Prise, and G. Schettino. Experimental setup and first measurement of DNA damage induced along and around an antiproton beam. *Eur. Phys. J. D*, 60(1):209–214, 2010.

1. Introduction

habent sua fata libelli

TERENTIANUS MAURUS

The discovery of the x-rays by Conrad Wilhelm Röntgen in the end of 1895 is considered as the time of birth of radiation research. Research and application of this new topic spread around the world in a speed not seen before and maybe not even after. The discovery of artificial ionising radiation even led to the discovery of natural radioactivity by Henri Becquerel less than a year later [Glasser et al., 1952].

Applications for the new phenomenon were found quickly. The first radiography of a part of the human body is a x-ray picture of the hand of Röntgen's wife from December 1895 [Glasser et al., 1952]. Already in January 1896 Emil Grubbè treated breast cancer with X-rays, not even six weeks after Röntgen published his results [Bernier et al., 2004].

Radiotherapy evolved over the the last century and is now an important aid in the treatment of cancer. In the following section cancer treatment with radiotherapy is introduced and with it the need of the quantification of radiation. The use of accelerated particles for treatment is motivated in Section 1.2. The introduction closes with the rationale for this thesis and an overview of its internal structure.

1.1 Radiotherapy in cancer treatment

Treatment of cancer with radiation has developed to a major component in cancer treatment next to surgery and chemotherapy. It is estimated that approximately half of all patients diagnosed wit cancer receive radiotherapy at some stage during their treatment [Delaney et al., 2005].

The main goal of radiotherapy is the concentration of energy deposition, in the terminology of radiation research referred to as dose, in the tumour and the sparing of healthy tissue. As shown in Figure 1.1, with an increased dose to a target volume the probability of elimination of cancer cells and thus the tumour as their manifestation rises. However, with an increased dose to healthy tissue also the probability of complications and even cancer introduced by the treatment rises. The balance between tumour control on one side and avoidance of radiation damage on the other side has to be ensured.

In internal radio therapy, also called brachytherapy (Greek *brachys*: close, short), the radiation source is placed close to the target, *i.e.* in the patient

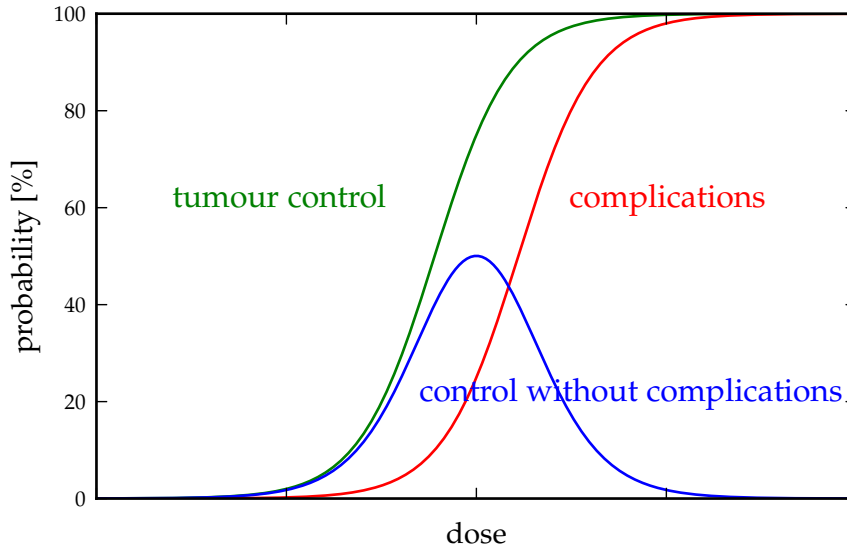


Figure 1.1: Schematic drawing of the probability of radiation effects as a function of dose. The green line represents the chance of tumour control, the red line represents the risk of radiation induce complications. The blue curve shows the probability of tumour control without complications.

thus avoiding the for the radiation need to pass through healthy tissue. External radio therapy is conducted with externally generated radiation fields of photons, electrons or ions. Healthy tissue has to be traversed by the beam in order to reach tumours seated in the body.

Commonly, photons are applied for radiotherapy. They are generated through Bremsstrahlung of decelerated electrons which have been accelerated by a linear accelerator (LINAC). In Figure 1.2 the red line represents a dose distribution along the beam axis of a 6 MeV photon field, an energy used in radiotherapy, in water. The dose maximum, and thus the maximal energy deposition is close to the entrance of the beam into the material. This is a disadvantage if the target of the treatment is a tumour which is located deeper than the dose maximum, as indicated by the grey area in Figure 1.2. To minimise the dose outside the tumour it is irradiated from different angles, such that the fields overlap in the target area and thus create a higher dose in the target with less dose in the healthy tissue. By modulation of the intensity of single fields, dose pattern which correspond to the tumour geometry can be achieved and dose to critical organs can be reduced. This technique is called intensity modulated radiotherapy (IMRT) and currently state of the art in cancer therapy with photons.

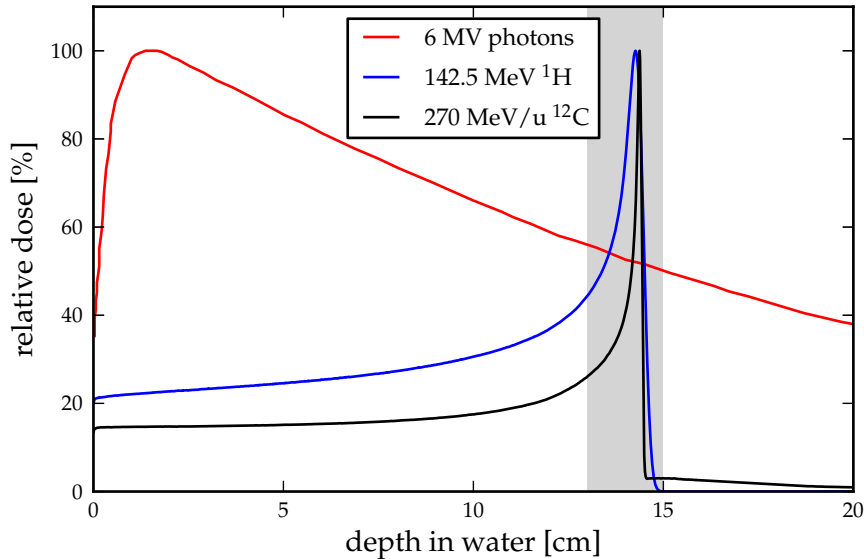


Figure 1.2: Comparison of mono-energetic depth dose distributions of photons, protons and carbon ions in water. The curves are calculated with the Monte Carlo code FLUKA and normalized to their dose maximum.

1.2 Radiotherapy with particles

Ions show a different depth dose profile as photons as demonstrated in Figure 1.2 on the example of protons and carbon ions. They have a finite range and their energy deposition is maximal at the end of their trajectory in the so-called Bragg peak. Based on this inverse dose profile Wilson [Wilson, 1946] suggested the use of energetic protons for radiotherapy in 1946, before accelerators could deliver particle beams with the required energies.

Besides the inverse dose profile particles also show less deflection from their beam path by scattering than photons which allows to irradiate small deep seated volumes with smaller radiation fields. With the variation of the initial particle energy the penetration depth and thus the location of the Bragg peak can be shifted. A superposition of several Bragg peaks, a so-called spread-out Bragg peak (SOBP), can be used to cover a volume with a homogeneous dose. In Figure 1.3a a proton SOBP (red curve) consisting of the superposition of many single Bragg peaks (blue lines) is shown. In this figure it is also visible that the ratio of the maximal energy deposition to the energy deposition in the entrance region is lower than for the mono-energetic case shown in Figure 1.2.

The total integral dose to normal tissue in a treatment with protons is up to a factor of two lower compared to IMRT [Lomax et al., 1999]. However,

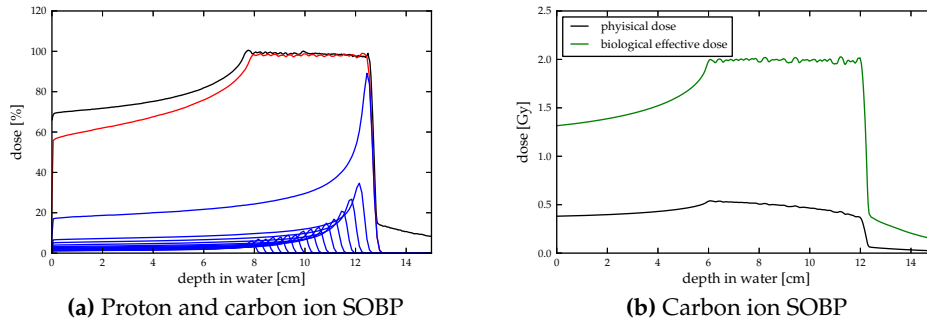


Figure 1.3: Proton and carbon ion SOBPs in water. The red dose distribution in Figure 1.3a represents a proton SOBP build of the superposition of the blue sub-peaks. The black line represents a physical optimized carbon ion SOBP. Figure 1.3b shows a biological optimized carbon ion SOBP. The physical dose (black line) is compared with the biological effective dose (green line). The physical doses in Figure 1.3a were calculated with FLUKA. The SOBP in Figure 1.3b was calculated with TRiP [Krämer et al., 2000].

the dose conformity of proton fields can be matched by IMRT in the most cases. Better results than with IMRT can be achieved by proton beams if the target volume is in the vicinity of critical organs or complex shaped dose distributions are required [Baumert et al., 2001]. The risk of secondary cancer is thus believed to be lower for tumour treatment with protons than for photon treatment [Schneider et al., 2006].

Ions heavier than protons have the advantage of less scattering and a higher ionisation density. This manifests in a narrower Bragg peak and a higher peak to entrance dose ratio. The use of heavier ions and especially carbon ions has also been suggested by Wilson [Wilson, 1946]. However, as seen in Figure 1.2 behind the Bragg peak of carbon ions dose is deposited due to fragmentation products.

The dose advantage of carbon ions over protons vanishes with superposition of several energies to a SOBP, as shown in Figure 1.3a, where the black line represents a carbon ion SOBP. However, due to less scattering a smaller penumbra in deep seated tumours can be achieved than with protons [Scharadt et al., 2010].

The main rationale for the employment of carbon ions is the additional biological effect [Durante and Loeffler, 2010]. A physical dose applied with carbon ions can result in a higher biological effect compared to the same dose applied with protons or photons. This effect is not constant over the whole particle range but is enhanced towards the end of the particle trajectory, in the Bragg peak. An increased physical dose in the peak, due to the stopping particles, is enhanced by an increased biological effect in the same region.

This allows to apply higher effective doses to the target region with same or less effective dose to the surrounding healthy tissue. Thus a higher probability of tumour control at the same or lower probability of side effects can be achieved. Figure 1.3b illustrates the enhanced biological effectiveness of a carbon ion SOBP. The black line represents the physical dose distribution. The dose in the target area is only slightly elevated to the dose in the entrance region. The biological effective dose (green curve), however, has a distinct peak dose compared to the entrance region.

The relative biological effectiveness (RBE), the ratio between the physical and biological effective dose is an important factor for patient treatment. It is, however, not related to one single physical quantity. For patient treatment it is calculated by models which take the energy deposition pattern of ions into account. The uncertainty in this models remain rather large with approximately 20 % [Karger and Jäkel, 2007].

As of today over 95000 patients have been treated with particle beams, 11770 of them with ions heavier than protons [PTCOG, 2012].

The question which treatment is the best can only be answered through comparing clinical trails and also only for specific indications favouring a single kind of treatment. Up to today it is neither answered if carbon ions are superior to protons [Suit et al., 2010] or if radiotherapy with particles has any benefit over photon therapy other than in rare indications [De Ruyscher et al., 2012].

1.3 The need for dosimetry

The successful application of radiotherapy requires an accurate beam delivery, regardless of the radiation type. Already a 5-7 % deviation in dose has an impact on clinical outcome [Brahme, 1984, Papanikolaou et al., 2004]. In the example of head and neck cancer a 5 % under dosage reduces the tumour control probability by 15 % while a 5 % higher dose increases the risk of side effects [Chappell and Fowler, 1994].

Accurate beam delivery, however, relies on the capability to measure dose, dosimetry. The characterisation of radiation fields and the control of these characteristics are major requirements for ensuring accurate dose delivery to the target.

The standard in dosimetry for radiotherapy are air-filled ionisation chambers. These are reliable in photon and ion beams. Due to their size constraints and the need of power supply they are not always suitable for the measurement of complicated radiation fields as used in intensity modulated radio therapy. Solid state detectors provide a higher signal per volume due to higher density. This enables smaller detectors and thus dosimetry with a higher spatial resolution. However, solid state detectors show saturation effects due to the higher signal density [Karger et al., 2010]. These effects are

elevated in particle beams due to higher ionisation density and localised high energy deposition in particle tracks.

Since the 1970ies phenomenological models are applied to predict the response of biological systems and solid state detectors in particle beams. Prominent is the track-structure theory (TST) based on the work of Butts and Katz [Butts and Katz, 1967].

However, the use of solid state detectors and the application of these models for dosimetry remain experimental up to today [Karger et al., 2010].

1.4 Outline of the thesis

This thesis describes the investigation of the use of the alanine detector in clinical relevant particle beams. The alanine detector is a solid state detector known since the sixties of the last century [Bradshaw et al., 1962] and has proven to be reliable in photon dosimetry [ICRU, 2008].

An existing response model from Hansen and Olsen [Hansen and Olsen, 1985] is employed and adapted to the particle energy range of interest. Experiments for verification of the adapted model have been conducted in clinical settings as well as in settings which allow a deeper insight into underlying assumptions. For the purpose of model verification also the lithium formate detector has been employed and included in the response model.

The final goal of the project was to bring the alanine detector from the status of an experimental detector in particle therapy to a level where it can be use in clinical practise. This thesis ends with an example of successful application of detector and response model in clinical settings and a suggestion for further use.

2. Interaction of radiation with matter

Ionising radiation can be divided into two classes: directly and indirectly ionising radiation. Charged particles are considered to be directly ionising, since they themselves Coulomb interact with atoms in matter. Neutral particles such as neutrons or photons, are considered to be indirectly ionising radiation, since they create secondary charged particles which then deposit energy in the target material.

This chapter focuses on interactions of photons and particles with matter in an energy range that is relevant in radiation therapy. Photon energies considered relevant for therapy are energies below ≈ 20 MeV, whereas particle energies are considered relevant when the particles have ranges in water from ≈ 0.1 mm to ≈ 35 cm, for example ≈ 1 to 450 MeV/u for carbon ions.

2.1 Photon interactions with matter

In this section the basic concepts and mechanisms of photon interaction with matter are briefly summarised. Since photon dosimetry is not in the focus of this thesis photon interactions with matter are described merely for completeness.

Photoelectric effect

In the process described as the photoelectric effect, the energy of an incoming photon releases an electron from a target atom. The photon energy is fully absorbed, the remaining energy is transferred to the kinetic energy of the ejected electron. Note that the photon ionises the target atom despite being classified as indirectly ionising.

The cross-section for the photoelectric effect is decreasing with increasing photon energy. The effect is dominant at low photon energies, *e.g.*, below ≈ 20 keV for targets with a low average atomic number Z , such as human tissue.

Compton scattering

A Compton scattering process is the inelastic scattering of a photon with a bound electron. The photon loses some of its energy and is deflected from its original direction. The electron is ejected, thus the atom is ionised.

Compton scattering is the dominant energy loss mechanism of photons in an energy range from ≈ 20 keV to ≈ 10 MeV for targets with a low average atomic number Z .

Pair production

The term pair production describes the generation of an electron / positron pair from a photon in the vicinity of a nuclear Coulomb field. Pair production has an energy threshold of 1.022 MeV, the rest mass of the produced particles. The photon energy exceeding the threshold is transformed into kinetic energy of the produced pair.

Pair production is the dominant photon energy loss mechanism for photon energies above ≈ 10 MeV in low Z materials.

Photo-nuclear interactions

Interactions of energetic photons with nuclei of the target material lead to emission of a nucleon. The nucleus gets excited and emits a proton (γ, p) or a neutron (γ, n). The threshold energy for a photo-nuclear reaction depends on the nucleus and the particular reaction, it is in the order of a few MeV. The contribution of photo-nuclear reactions to the total attenuation coefficient is in the order of a few percent.

Photon attenuation

The intensity I of a photon beam in matter as a function of the depth in matter x can be described by Lambert Beer's law.

$$I(x) = I_0 e^{-\mu(E,Z)x} \quad (2.1)$$

Where I_0 is the initial intensity and $\mu(E, Z)$ the total attenuation coefficient. The total attenuation coefficient is the sum of the attenuation coefficients for all possible interactions.

The actual energy deposition in matter as a function of depth in matter as seen in Figure 1.2 deviates from the pristine Lambert Beer's law in the entrance region of the material volume, since the location of an intensity reducing event, *e.g.* the production of a positron / electron pair, and the locations of energy deposition, *e.g.* through the secondary positron and electron, may differ. In the so-called *build-up* region an equilibrium of energy loss of the radiation field and energy absorption of the material has not established yet. In the distal region, behind the peak, an equilibrium has been established and the energy deposition is also decreasing exponentially with the distance in matter.

2.2 Energy deposition of swift particles in matter

Stopping force

This section's discussion of particles stopping in matter in follows the book of Sigmund [Sigmund, 2004] and the theoretical part of report 49 of the International Commission on Radiation Units & Measurements (ICRU) [ICRU, 1993]. The complex physical concepts behind particle slow-down will not be discussed in detail in this thesis. They will be merely named and the resulting formalism, describing the energy loss will be presented.

The stopping force¹ S of a particle in a material is the average negative energy loss dE of a particle in a material while passing a distance dl . It is defined with a negative sign in order to obtain a positive value of the stopping force. The mass stopping force is the stopping force divided by the density ρ of the target material.

The total stopping force S of a particle in a target material is the sum of the energy loss per distance due to interactions of the projectile ion with electrons in the target, due to interactions with the nuclei and due radiative energy losses.

$$S = \left(\frac{dE}{dx} \right)_{\text{elec}} + \left(\frac{dE}{dx} \right)_{\text{nucl}} + \left(\frac{dE}{dx} \right)_{\text{radiat}} \quad (2.2)$$

The electronic stopping force is the dominant term over a wide energy range. Nuclear stopping contributes less than 0.5 % to the total stopping force at projectile energies with corresponding particle speeds above the speed of orbital electrons in the target. However, for heavy projectiles, nuclear stopping becomes dominant for projectile speeds around and below the Bohr velocity v_0 , which corresponds to a particle energy of 25 keV/u. Radiative energy loss can be neglected for ions at energies available at medical accelerators. However, at energies above 10^6 MeV/u pair creation and Bremsstrahlung dominate the energy loss in heavy materials.

Electronic stopping force

The electronic mass stopping force denotes the energy loss of the traversing particle due to interactions with orbital electrons of the target material. The transferred energy causes excitation or ionisation of a target atom. It can be expressed by Equation 2.3, which is commonly referred to as *Bethe* or *Bethe-*

¹While commonly named *stopping power* from the physics point of view, the term *stopping force* would be more appropriate as discussed by Sigmund [Sigmund, 2000]. In this thesis the author will try to consistently use the nomenclature *stopping force* and thus follow the ICRU report 73. This is also due to his metrical preferences.

Bloch formula.

$$\frac{S_{\text{elec}}(E)}{\rho} = \frac{4\pi e^4}{m_e v^2} \frac{1}{u} \frac{Z}{A} z \left[\ln \left(\frac{2m_e v^2}{I} \right) + \ln \left(\frac{1}{1 - \beta^2} \right) - \beta^2 - \frac{C}{Z} - \frac{\delta(\beta)}{2} \right] \quad (2.3)$$

Here e denotes the elemental electric charge, m_e the electron rest mass, u the atomic mass unit, v and z the speed and effective charge of the projectile ion, respectively, and Z and A the atomic number and the number of nucleons of the target material, respectively.

The concept of the effective charge z is an attempt to account for electron capture and charge shielding for low projectile energies. However, it is also used as a free parameter to fit stopping force formalisms to empirical data [Hubert et al., 1989, Fettouhi et al., 2006].

The first three terms in the brackets are commonly referred to as “Bethe formula”. I denotes the mean excitation energy, which is a property of the target material. The I -value can be theoretically calculated as mean oscillator strength, or extracted from penetration depth measurements. Even though the I -value has a non-negligible impact, *e.g.* on particle range calculations, which vary in the millimetre range for different recommended values [Andreo, 2009], it is not well established for all materials. For water, different values are stated in literature [ICRU, 1993, Sigmund et al., 2009, Kumazaki et al., 2007, Paul et al., 2007] ranging from 75 ± 3 eV to 80.8 eV. The second and third term in the brackets are relativistic corrections.

The shell correction term (C/Z) becomes relevant for lower energies, it corrects for atomic bindings in the material. The “density effect” ($\delta(\beta)/2$) is due to medium polarisation at high particle speeds.

Figure 2.1 shows the electronic mass stopping force of carbon ions in water from different sources. These sources are discussed later in this section.

The Bethe formula agrees with measurements over the intermediate energy range, above the stopping force maximum and below the onset of radiation losses. For lower energies Equation 2.3 diverges and is not valid any more.

For energies below the stopping force peak, the stopping force scales linearly with projectile speed. The uncertainties of calculations in this regime may be up to 20% [Fettouhi et al., 2006]

The isotopic effect on the stopping force amounts to maximal 0.25 % for stable isotopes and is generally neglected.

Nuclear stopping force

Nuclear stopping describes the energy loss due to the interaction of the projectile ion with nuclei of the target atoms. This is mainly due to elastic scattering of the projectile on the Coloumb potential of a nucleus. Under the assumption of negligible quantum effects this problem is treated with classical binary elastic scattering theory. However, screening of the Coulomb

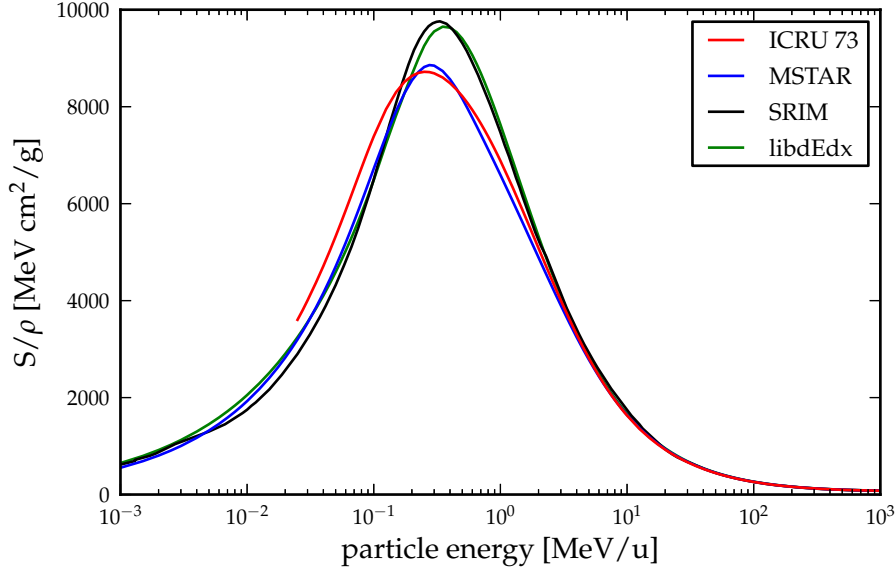


Figure 2.1: Electronic mass stopping force of carbon ions in water as a function of the particle energy from four different sources. See text for description.

potential of the projectile due to electron capture, and thus the concept of an effective charge, is highly relevant for nuclear stopping.

In this model, inelastic interactions such as nuclear fragmentation are excluded.

Stopping in compounds

The stopping force formula as introduced in Equation 2.3 yields values for elemental targets only. For compounds, Bragg's additivity rule [Bragg and Kleeman, 1905], a mass weighted linear combination of the stopping forces of the atomic constituents, can be applied. Be c a compound of N constituents i with the mass a_i , respectively. The mass stopping force $\left(\frac{S}{\rho}\right)_c$ of c is then

$$\left(\frac{S}{\rho}\right)_c = \frac{\sum_i^N a_i \left(\frac{S}{\rho}\right)_i}{\sum_i^N a_i}, \quad (2.4)$$

where $\left(\frac{S}{\rho}\right)_i$ is the stopping force of constituent i . This approximation neglects differences in the chemical bonding structure of compounds. How-

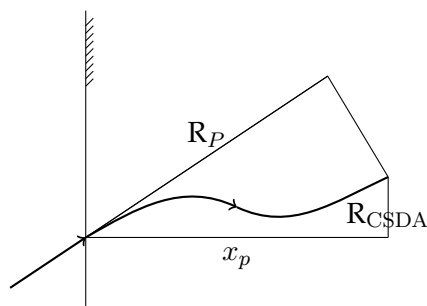


Figure 2.2: Schematic drawing to illustrate the range definitions.

ever, it is a reasonable first order approximation for the stopping force in compounds where data are missing.

Range

When the stopping force is known, the range of a particle with energy E_0 along the path can be obtained by integrating the inverse of the stopping force over the energy from E_0 to $E = 0$,

$$R_{\text{CSDA}} = \int_0^{E_0} \frac{dE}{S_{\text{total}}(E)}. \quad (2.5)$$

This is commonly called the continuous slowing down approximation (CSDA), since no fluctuations in energy loss are considered.

The *projected range* R_P is a projection of the stopping point of the particle onto the direction at particle impact. If the particle impacts the material at a right angle, the projected range equals the penetration depth x_p . The different range concepts are visualised in Figure 2.2.

Stopping force sources

Several stopping force calculation codes exist. Some are purely motivated by theory, while others are based on experimental data. In this paragraph the codes and tables used for calculations in this thesis and their restrictions are described. A full discussion of codes can be found in references [Sigmund et al., 2005, Paul, 2010].

For protons and alpha particles, stopping force and range (STAR) tables are provided by the National Institute of Standards and Technology (NIST). These tables are called PSTAR and ASTAR [Berger et al., 2005], respectively and are identical with the values given in the ICRU report 49 [ICRU, 1993]. The energy range of the provided data spans from 1 keV to 10000 MeV for protons and from 0.25 keV/u to 250 MeV/u for alpha particles.

Values of the electronic stopping force for ions from lithium to argon are provided by the MSTAR code [Paul and A., 2001], which applies a charge

scaling on the stopping force of helium ions, and the values tabulated in the ICRU report 73 [Sigmund et al., 2005] and its erratum [Sigmund et al., 2009], which are based on theoretical considerations. While the ICRU report covers particle energies from 0.025 to 1000 MeV/u, the MSTAR code provides values for a range from 0.0001 to 1000 MeV/u. All codes and tables mentioned so far in this section are included in the open-source library libdEdx [Lühr et al., 2011], which provides a single interface to all of them. The library also includes an implementation of the Bethe-Bloch formula, employing the Lindhard-Scharff low-energy extension. The results of this Bethe-Bloch implementation is shown in Figure 2.1.

The SRIM (stopping and range of ions in matter) code [Ziegler et al., 2010] provides electronic and nuclear stopping power for all ions in an energy range from 1 eV to 2 GeV based on scaling procedures.

An example of the numerical deviations between codes is shown in Figure 2.1. Those deviations result in range calculation uncertainties in the order of a few percent [Lühr et al., 2011].

3. Basics of dosimetry

Radiation dosimetry is –strictly speaking– the determination of the quantity *absorbed dose*. Detectors able to measure this quantity are referred to as *dosimeters*. However, also the determination of related quantities is commonly referred to as dosimetry. In this chapter the basic concepts and quantities of dosimetry will be introduced. Beyond the basic concepts this summary mainly focuses on topics relevant to problems addressed in this thesis. The definitions and descriptions will follow the ICRU definitions in the Report 60 on fundamental quantities and units [ICRU, 1998] if not mentioned otherwise.

3.1 Particle fluence

The number of particle that enter a volume of interest is a crucial quantity for all dosimetric considerations. The *particle fluence* or simple *fluence*, Φ , is defined as the amount of particles ΔN crossing a sphere of cross-sectional area Δa ,

$$\Phi = \lim_{\Delta a \rightarrow 0} \frac{\Delta N}{\Delta a} . \quad (3.1)$$

Fluence is measured in units of $1/\text{cm}^2$. The *planar particle fluence* refers to the number of particles traversing a plane. This definition is dependent on the angle of incident. For a perpendicular angle of incident the planar fluence equals the fluence as defined in Equation 3.1.

3.2 Absorbed dose

The absorbed dose D is the mean imparted energy $d\bar{\epsilon}$ per mass dm . The imparted energy ϵ is the sum over the energy deposited by all energy depositing events in a volume,

$$D = \frac{d\bar{\epsilon}}{dm} . \quad (3.2)$$

Dose is expressed in the unit gray (Gy), which is defined as J/kg. Dose is a macroscopic, non-stochastic quantity. The microscopic equivalent to dose is the specific energy z

$$z = \frac{\epsilon}{m} , \quad (3.3)$$

the quotient of the imparted energy to mass of the volume the energy is imparted. The specific energy is a stochastic quantity. The mean value of the specific energy \bar{z} converges to the dose D for increasing volumes.

In the case of a charged particle equilibrium the dose equals the product of particle fluence and mass stopping force

$$D = \sum_i \int_E \Phi_{i,E} \cdot \frac{S_i(E)}{\rho}, \quad (3.4)$$

where $\Phi_{i,E}$ denotes the fluence of particle i with energy E and $S_i(E)$ the stopping force of that particle.

Dose to water

For dose comparison it is essential to report in which material the dose is measured, since the same radiation field deposits a different amount of dose in different materials. In order to compare dose values commonly the equivalent dose in water is reported and dosimeters are calibrated to dose to water.

The ratio between the dose to material a to dose to material b is in first approximation well described by the ratio of stopping forces of the radiation in question in the materials, respectively. It is defined as the ratio of the sum over all particles of the fluence-weighted stopping forces in the medium, respectively.

$$S_{a,b} = \frac{\sum_i \int_0^\infty \Phi_{a,i}(E) S_{a,i}(E) / \rho \, dE}{\sum_i \int_0^\infty \Phi_{a,i}(E) S_{b,i}(E) / \rho \, dE} \quad (3.5)$$

Note, that the fluence ($\Phi_{a,i}$) is the same in numerator and denominator. For charged particles the influence of the stopping-force ratio increases with the differences in material compositions. For protons in clinical settings the impact of the a conversion from dose to tissue to dose to water up to $\approx 10\%$ for bony tissue [Paganetti, 2009]. For carbon ions effects of up to 8% are expected in bony tissue [Herrmann et al., 2009].

A correction for the change in fluence between materials ($\Phi_{a,i}$) is the fluence correction factor (FCF). For further reading on the FCF the articles by Palmans *et al.* [Palmans et al., 2002] and Lühr *et al.* [Lühr et al., 2011b] are recommended.

3.3 Linear energy transfer

The linear energy transfer LET_Δ is the amount of energy lost by a particle in a material dE , due to secondary electrons with an energy less than Δ , over a distance dx [ICRU, 1998]. For $\Delta \rightarrow \infty$ the LET_Δ gets numerically equal to the electronic stopping force. In fact, the terms are often used as

synonyms. In this thesis when referring to linear energy transfer (LET) it is always referred to the LET_{∞} . The LET is also sometimes called restricted linear electronic stopping force.

The definition above is just unambiguous for a single ion. In volumes where a mixed radiation field exists an average LET has to be calculated. There are two weighting methods. First, by deposited energy, the so-called dose-averaged LET and second, by particle fluence, the so-called tracklength-averaged LET.

The dose-averaged LET is defined as

$$LET_{DA} = \frac{\sum_{i,E} \Phi_{i,E} \cdot \left(\frac{dE}{dx} \Big|_{i,E} \right)^2}{\sum_{i,E} \Phi_{i,E} \cdot \frac{dE}{dx} \Big|_{i,E}} \quad (3.6)$$

where $\Phi_{i,E}$ denotes the fluence of the particle i with kinetic energy E and $\frac{dE}{dx} \Big|_{i,E}$ its stopping force.

In contrast the tracklength-averaged LET is defined as

$$LET_{TA} = \frac{\sum_{i,E} \Phi_{i,E} \cdot \frac{dE}{dx} \Big|_{i,E}}{\sum_{i,E} \Phi_{i,E}} \quad (3.7)$$

The average LET is often used to characterise a radiation field as being *low-LET* or *high-LET*. Photon radiation, electron and proton beams are referred to as low-LET radiation, whereas heavier ions are referred to as high-LET radiation. However, strict relations between LET and biological effects, as RBE or oxygen enhancement ratio (OER), do not exist [Kraft et al., 1992]. Nevertheless, these effects are often described as a function of the averaged LET [Wilkens and Oelfke, 2004, Sørensen et al., 2011, Wenzl and Wilkens, 2011].

3.4 Relative biological effectiveness

The macroscopic dose is insufficient in describing the effects of radiation of different kind onto biological systems. The same macroscopic dose applied with two different kinds of radiation may result in a different response of the biological system, *e.g.* the percentage of killed cells.

The relative biological effectiveness (RBE) is used to compare the effectiveness of one radiation quality with a reference radiation. Due to historic reasons γ -rays emitted from ^{60}Co sources are often used as reference. This cobalt isotope emits γ -rays of 1.17 and 1.33 MeV.

The RBE is defined as the ratio of the dose deposited by the reference radiation D_{60Co} to the dose by the test radiation D_x , which result in the same

biological effect,

$$RBE = \frac{D_{60Co}}{D_x} \Big|_{\text{iso-effect}} \quad (3.8)$$

The RBE of a radiation quality strongly depends on the chosen biological endpoint. The RBE of 11 MeV/u carbon ions on Chinese hamster ovary cells (CHO-K1) ranges, *e.g.*, from 5.4 for the 50 % survival fraction endpoint to 3.4 for 1 % survival fraction endpoint with 250 kV x-rays as reference radiation [Weyrather et al., 1999].

3.5 Calorimetry

The most direct way of measuring deposited energy and thus dose is calorimetry. Under the assumption that the whole deposited energy is transferred into heat, the temperature rise in a volume of known mass is measured. If the specific heat capacity c_p of the absorber is known, the rise in temperature ΔT translates linearly into dose,

$$D = c_p \Delta T \quad .$$

With calorimetry it is possible to directly measure the dose to water, if the sensitive volume is filled with water. There are also calorimeters with a sensitive volume of graphite. The procedure requires that the irradiated volume is thermally isolated from its environment, and the apparatus is in thermal equilibrium with the environment [ICRU, 2008]. These requirements make calorimetry laborious and not suited for all purposes. Thus, for practical use outside of primary standard laboratories different approaches have to be applied.

However, calorimetry is suitable for dosimetry in particle beams, since corrections of maximal 1 % for energy loss to chemical bindings are independent of the radiation type [Palmans et al., 1996, Giesen et al., 2007].

3.6 Ionisation chambers

Ionisation chambers are based on the ionisation of matter by radiation, which first has been observed by J. Perrin in 1896 [Glasser et al., 1952]. If this ionisation occurs in a volume where an electric field is applied the created charge separates and can be measured at the electrodes. If the average energy required for one ionisation and the charge collection efficiency is known, the energy deposited in the volume can be determined.

Ionisation chambers exist in several designs, *e.g.* with cylindrical outer electrodes and a central electrode in the middle or two parallel plane electrodes. Different designs have different properties and can be chosen ac-

ording to the requirements. However, they all function following the above mentioned principle.

Air-filled ionisation chambers are considered as the gold standard in dosimetry for radiotherapy. Corrections for environmental influences and possible recombination of the charge have to be applied, though.

Ionisation chambers filled with a liquid provide the advantage that, due to a higher ionisation density, the active volume can be reduced and a higher spatial resolution can be achieved. However, due to the higher ionisation density charge recombination effects are also increased [Tölli et al., 2010].

Ionisation chambers are reusable and offer an instantaneous dose measurement, contrary to passive detector systems. A drawback is the need of a power supply.

In particle beams the charge recombination is pronounced [Kanai et al., 1998] and additional uncertainties are introduced [Andreo et al., 2004].

3.7 Solid state detectors in particle beams

Solid state detectors are detectors which determine dose based on energy deposition in an active volume of condensed matter. The advantage of solid state detectors over air-filled ionisation chambers is their higher ionisation density and thus the possibility to achieve smaller detectors and thus higher spatial resolution for dosimetry. The advantage is bought with a higher sensitivity towards radiation quality, commonly referred to as *LET-effects* [Karger et al., 2010]. However, since the term *LET-effects* might imply that those effects would be directly and only dependent on LET and thus tends to be misleading, it will not be used in this thesis.

Most solid state detectors irradiated with particle beams show a response dependency not only on dose, but also on the nature of the radiation field. A typical symptom is a decreased ratio between the detector signal in the Bragg peak to the detector signal in the plateau of a depth dose curve compared to the dose ratio.

This phenomenon is –at least for ions heavier than protons– reported for most solid state detectors such as diamond detectors [Sakama et al., 2005], diodes [Kaiser et al., 2010], films [Spielberger et al., 2002, Kirby et al., 2010], thermoluminescent dosimeters (TLDs) [Geiß et al., 1998, Holzscheiter et al., 2004], optical stimulated luminescence (OSL) [Edmund et al., 2007, Klein et al., 2011], gel detectors and also EPR dosimeters as alanine [Bradshaw et al., 1962, Waligorski et al., 1989, Bassler et al., 2008, Herrmann et al., 2011b]. These effects of reduced effectiveness towards certain radiation types is expressed in the relative effectiveness (RE).

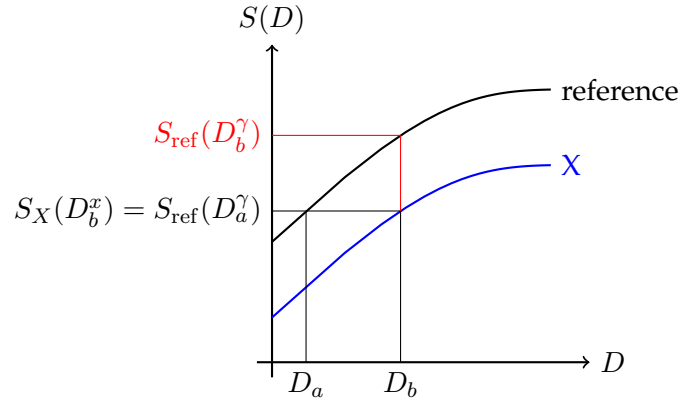


Figure 3.1: Schematic illustration of both RE definitions

Relative effectiveness

In order to describe the behaviour of a dosimeter in a radiation x different from the reference radiation, the quantity of relative effectiveness (RE) η is used which puts the different detector responses into relation. However, even though the concept of the RE is often used in literature there is no unique definition for the RE. Basically there are two definitions used.

The iso-response definition,

$$\eta_{\text{iso-response}} = \frac{D_{\text{ref}}}{D_x} \Big|_{\text{iso-response}}, \quad (3.9)$$

is orientated at the definition of the RBE. It is the ratio of the dose applied with the reference radiation D_{ref} and the dose of the radiation x , D_x , which yield the same detector response. The RBE can be seen as the biological counterpart to the RE.

The second definition uses the ratio of the response of the detector irradiated with the reference radiation, $S(D_{\text{ref}})$, to the response after irradiation with radiation x , $S(D_x)$, at the same nominal dose.

$$\eta_{\text{iso-dose}} = \frac{S(D_0^x)}{S(D_0^{\text{ref}})} \Big|_{\text{iso-dose}} \quad (3.10)$$

Figure 3.1 illustrates the two definitions. The black line represents the detector response $S(D)$ as a function of dose deposited by the reference radiation. The blue line describes the response behaviour towards radiation x .

While Katz [Katz, 1978] made no differentiation between RE and RBE and thus used for both the iso-response definition, Waligorski [Waligorski et al., 1989] defined the RE as iso-dose ratio and made a clear distinction between the RE and the

RBE. In literature both the iso-response [Fattibene et al., 2002, Gerstenberg et al., 1990, Hansen, 1984, Jirasek and Duzenli, 2002, Katz, 1978, Kirby et al., 2010, Martisíková and Jäkel, 2010, Olsen and Hansen, 1985, Simmons and Bewley, 1976, Zhao and Das, 2010] and the iso-dose definition [Edmund et al., 2007, Hansen et al., 1987, Olko, 1999, Olsen and Hansen, 1990, Palmans, 2003, Waldeland et al., 2010, Waligorski et al., 1989] can be found to a similar amount.

In special cases both definitions yield the same numerical value. However, this is not general applicable. Section 4.4 discusses the implication of the choice of definition for one-hit detectors.

The *iso-dose* definition can be motivated for theoretical considerations, where one is interested in the response of a detector to one dose value applied by different radiation types. For all practical means however the *iso-response* is preferable. The main argument for this will in the following be elaborated on the example of the situation illustrated in Figure 3.1.

Given a detector calibrated to a reference radiation. The dose D_b is applied with a radiation x , different from the reference radiation. The detector readout yields a detector response $S_x(D_b)$, on which the calibration is applied. This yields the dose applied by reference radiation D_a corresponding to the measured signal $S_{\text{ref}}(D_a) = S_x(D_b)$. If the iso-response RE of a detector towards radiation x is known the absorbed dose to the detector can be determined by

$$D_b = D_a \cdot 1/\eta_{\text{iso-response}} \quad (3.11)$$

If, on the other hand, only the iso-dose RE is known in this example the applied dose D_b can not be derived.

In order to be precise when speaking of detector response or signal a new term shall be introduced here, the response equivalent dose (RED). When speaking of detector response or signal it will refer to the actual signal at the detector readout, *e.g.* the integral glow curve for TLDs, the absorption spectrum for electron spin resonance (ESR) dosimeter or the collected charge for a ionisation chamber. RED denotes the dose value in gray, which one receives applying the calibration onto the detector signal. The RED deviates from the physical dose by the factor η , the RE. Equation 3.9 reads then as

$$\eta = \frac{RED}{D}. \quad (3.12)$$

In this thesis **always the iso-response definition** of the relative effectiveness will be used, if not mentioned differently.

Relative effectiveness in a mixed radiation field

The relative effectiveness in a mixed particle field follows the definition in Equation 3.9. If track overlapping effects can be neglected the average rela-

tive effectiveness $\bar{\eta}$ can be defined as

$$\bar{\eta} = \frac{\sum_i \sum_j \eta_i(E_j) D_{i,j}}{D_{\text{total}}}, \quad (3.13)$$

where $\eta_i(E_j)$ is the relative effectiveness of the particle i with kinetic energy j and $D_{i,j}$ is the dose deposited by this particle. D_{total} is the total deposited dose [Katz, 1993].

4. Amorphous track models

4.1 Basic assumptions

Amorphous track models, also called track-structure models, try to predict the response of a system to particle irradiation based on a phenomenological approach. The theory originates in the work of Butts and Katz [Butts and Katz, 1967] on the RBE of heavy ions on biological systems. Amorphous track models are based on two main assumptions:

- I The energy deposition around a particle trajectory can be described by a continuous, averaged radial dose profile.
- II The detector responds locally in the same manner to energy deposited by secondary electrons, regardless of their origin.

The release of secondary electrons through a heavy charged particle (HCP) and the energy deposition by those are stochastic processes. Figure 4.1a shows one history of a Monte Carlo simulation of a 100 MeV/u carbon ion traversing water. The figure illustrates the energy deposition around a particle track projected on one plane. There is a dense electron distribution close to the ions trajectory and just a few secondary electrons with high energies emerging to further distances. Also the scattering of the secondary electrons is illustrated. The simulation has been conducted with the TRAX Monte Carlo code¹ [Krämer, 1995].

Averaging over many particle tracks an average dose distribution around a particle track can be assumed. This is comparable with the description of the energy loss of a particle by the stopping force which also does not describe the stopping of a single particle but the mean value of the energy loss.

The radial dose distribution (RDD) is assumed to be the homogeneous distribution of the energy deposition around a particle trajectory due to secondary electrons. Figure 4.1b shows the RDD for 100 MeV/u carbon ions in water, calculated with TRAX averaged over 10000 particle histories. This amorphous δ -electron halo around the particle trajectory gives the models base on this assumption their names.

Following assumption II the characterisation of a detector in a photon radiation field is sufficient to describe the response of this detector in any other radiation field, since—in this picture—the detector response is only dependent

¹<http://bio.gsi.de/DOCS/TRAX/NEW/DOCS/trax.html>

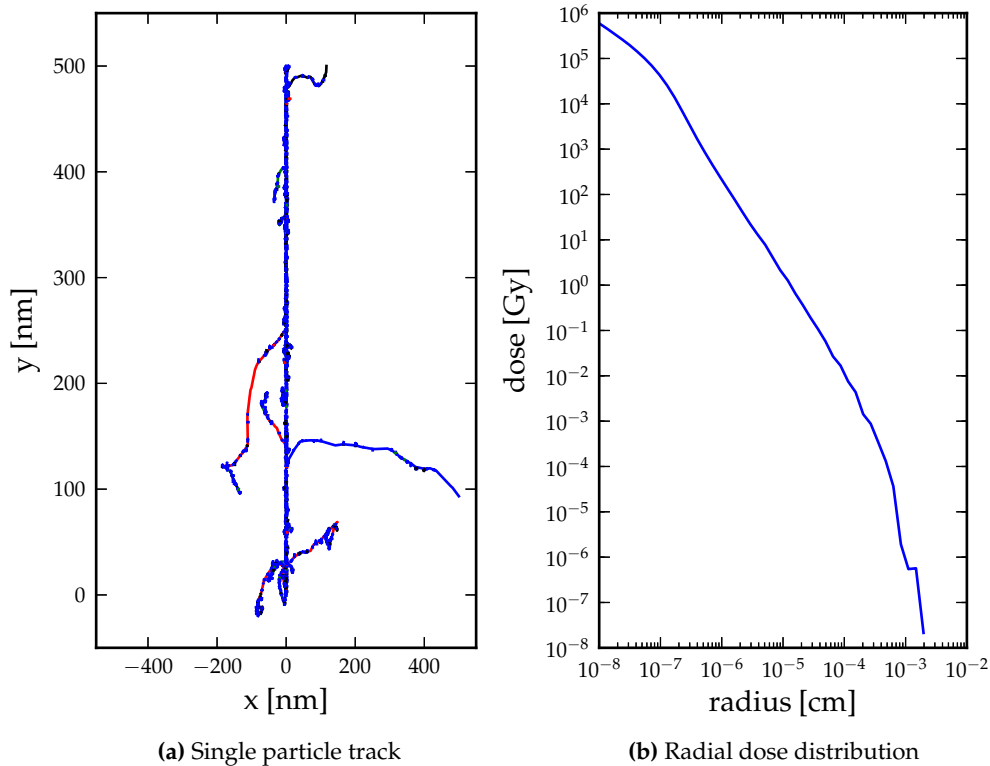


Figure 4.1: Graph 4.1a shows the energy distribution around a single ion trajectory of a 100 MeV/u carbon ion in water. Figure 4.1b shows the correspondent RDD as a function of the distance from the trajectory. Both graphs are calculated with TRAX.

on the local dose level. Differences in the macroscopic response to the same amount of macroscopic dose deposited by different types of radiation are explained with different dose distribution patterns. The local dose around a particle trajectory varies over orders of magnitude as seen in Figure 4.1b while in photon radiation fields the dose is considered to be deposited homogeneous on a microscopic level due the increased scattering of photons.

A precondition of assumption II is that the energy spectra of secondary electrons are comparable for photon and HCP radiation, or that the detector response is insensitive to the kinetic energy of energy depositing electrons.

Amorphous track models are regarded as phenomenological models since the detector is only described by its photon response characteristic.

The original model by Butts and Katz and the underlying assumptions are discussed in detail in the next sections.

4.2 Target theory

Target theory is a formalism developed to describe the behaviour of radiation sensitive systems under radiation, technically speaking the shape of dose-response relations of the systems. The formalism was developed for biological systems and attempts to give some physical meaning to the parametrisation of the dose-response behaviour. This section explains the basic concepts of target theory, in order to familiarise the reader with terminology still used in the detectors description. This section is mainly based on the book by Dertinger and Jung [Dertinger and Jung, 1969] but does not follow it in all conclusions.

In target theory a system is considered to consist of sensitive, spherical, *active* elements, also called targets, which are embedded in a passive matrix. Radiation can trigger an effect in a sensitive element, *inactivate* the element, if at least a certain number n energy depositing events, so-called *hits*, occur. A hit is an event in which at least an energy larger or equal the minimal required energy E_{\min} is deposited in the target.

Under the assumptions of Poisson distributed hits, the probability P of exactly n hits after an applied dose of D is given as

$$P(n) = \frac{(vD)^n e^{-vD}}{n!} \quad (4.1)$$

where vD denotes the average number of hits. v is the *target volume* measured in *hit per gray*. The target volume is abstract concept and is further discussed later in this section.

If a target required n hits to be inactivated, targets with $n-1$ hits or less are not affected. Be N the number of affected targets, and N_0 the total number of targets then the fraction of affected targets can be expressed as the sum over all targets receiving less than n hits:

$$\frac{N(D)}{N_0} = 1 - e^{-vD} \sum_{k=0}^{n-1} \frac{(vD)^k}{k!} \quad (4.2)$$

For the case of already one hit being sufficient for triggering an effect, Equation 4.2 simplifies to

$$\frac{N(D)}{N_0} = 1 - e^{-vD}. \quad (4.3)$$

If the number of inactivated elements can be quantified the system can be used as a detector and Equation 4.3 describes its dose-response behaviour. Such a detector is commonly referred to as *one-hit detector* or *single-hit detector*. The dose-response of one-hit detectors can be characterised by the D_{37} value. D_{37} is the dose at which $\approx 63\%$ of the saturation signal is reached. In the case of biological system this means 37% of the system, *e.g.* cells survived. The

D_{37} values is the reciprocal of the target area v , thus

$$\frac{N(D_{37})}{N_0} = 1 - e^{-1} \approx 0.63$$

The D_{37} value is also referred to as *characteristic dose*. At a dose D_{37} in average every element received one hit.

Since a hit is related to an energy deposition, dose is in target theory regarded as hit per volume. Thus the geometrical size of the target volume can be estimated with the D_{37} value and the average energy of one hit ξ . Under the assumption of a spherical target the radius of a target a_0 can be calculated as

$$a_0 = \sqrt[3]{\frac{3}{4\pi} \cdot \frac{1}{\rho} \cdot \frac{1}{D_{37}} \cdot \xi} \quad , \quad (4.4)$$

where ρ denotes the density of the detector material.

A step towards generalisation is from multi-hit detectors to multi-target detectors, in which an effect occurs, if m targets receive at least n hits. The probabilities multiply, thus the relative number of affected elements can be expressed as

$$\frac{N(D)}{N_0} = \left(1 - e^{-vD} \sum_{k=0}^{n-1} \frac{(vD)^k}{k!} \right)^m \quad . \quad (4.5)$$

Multi-hit detectors show supralinear dose response, which in particle beams can lead to a relative effectiveness above unity. An example for a multi-hit detector are TLDs, whose dose-response can be described as a combination of one-hit and two-hit behaviour [Katz, 1978, Geiß et al., 1998].

4.3 The Butts and Katz model

Based on target theory Butts and Katz [Butts and Katz, 1967] developed a response-model for one-hit detectors and later on also for systems showing multi-hit response, as cells [Katz, 1978]. The derivation of the one hit model shall be introduced in this section.

Assuming a charged particle equilibrium in a mono-energetic charged particle radiation field, following Equation 3.4 dose can then be expressed as the product of the fluence and the mass stopping force,

$$D = \Phi \frac{S}{\rho} \quad .$$

This in mind the characteristic dose D_{37} can be related to a characteristic fluence Φ_{37} which is the reciprocal of the activation cross section $\sigma = 1/\Phi_{37}$. The activation cross-section towards a radiation x is related to the characteristic dose as

$$\frac{1}{D_{37,x}} = \sigma_x \left(\frac{S}{\rho} \right)^{-1} \quad (4.6)$$

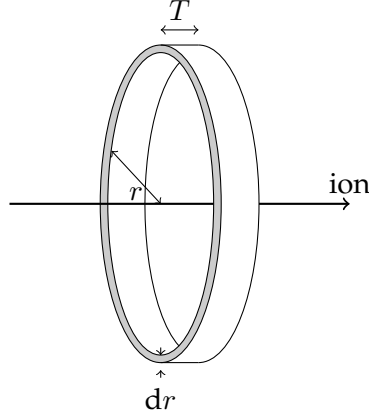


Figure 4.2: Cylindrical iso-dose shell around an ion trajectory.

Activation cross section

Given a radial dose distribution $D_\delta(r)$ the number of effects invoked by δ -electrons in a concentric cylindrical shell with an inner radius r , outer radius $r + dr$ and a length T be $d\mathfrak{N}$. The number of effects $d\mathfrak{N}$ is the product of the volume V of the shell, the amount of elements per volume N_0 and probability P of an element getting activated, as given in Equation 4.7.

$$d\mathfrak{N} = VN_0P \quad (4.7)$$

$$= (2\pi T r dr) N_0 \left(1 - e^{-\frac{D_\delta(r)}{D_{37,\gamma}}} \right) \quad (4.8)$$

Figure 4.2 illustrates this setting. The depth of the shell T has to be chosen in a way that the particle speed and thus the stopping force can be assumed to be constant.

Note that in Equation 4.8 the dose deposited by the secondary electrons of the primary ion $D_\delta(r)$ is put into relation with the characteristic dose at photon irradiation $D_{37,\gamma}$ and thus assumption II is applied.

An integration of Equation 4.8 over all radii r yields the total amount of effects \mathfrak{N} for one traversing ion. The activation cross section σ in Equation 4.9 is given as the ratio of the total amount of effects and the amount of elements per area N_0T

$$\sigma = \frac{\mathfrak{N}}{N_0T} = 2\pi \int_0^\infty r dr \left(1 - e^{-D_\delta(r)/D_{37,\gamma}} \right) \quad (4.9)$$

Radial dose distribution

The cross-section σ_ω for the emission of a δ -electron with a kinetic energy in the interval $[\omega; \omega + d\omega]$ at a transit of a HCP is calculated by Butts and

Katz [Butts and Katz, 1967] using the solution of the Kepler problem. The central force in this picture is the Coulomb force.

$$\sigma_{\omega} = \frac{2\pi e^4}{m_e c^2} \cdot \frac{Z_{\text{eff}}^2}{\beta^2} \cdot \frac{d\omega}{\omega^2} \quad (4.10)$$

here Z_{eff} denotes the effective charge of the ion, β its speed relative to the speed of light, e the elemental charge and m_e the mass of an electron.

The emission cross-section σ_{ω} multiplied by the electron density N_e of the material yields the δ -electron distribution $dn = \sigma_{\omega} \cdot N_e \cdot d\omega$. dn is the number of emitted electrons in the energy interval $[\omega; \omega + d\omega]$. The maximum energy ω_{max} of a secondary electron is determined by a classical central hit between ion and electron, and thus

$$\omega_{\text{max}} = 2m_e c^2 \cdot \frac{\beta^2}{1 - \beta^2}, \quad (4.11)$$

The range of electrons in matter is described by power law expression fitted to experimental data

$$r = k \cdot \omega^{\alpha}, \quad (4.12)$$

where k is a fitted parameter in units of [length · energy^{-α}]. In their original work Butts & Katz found α to be equal one by fitting experimental data. Later other authors found different values.

Equation 4.12 implies that an electron passing the distance dr deposits an energy

$$d\omega = (k^{-1} dr)^{\alpha^{-1}} \quad (4.13)$$

An integration over the energies in the interval $[\omega(r); \omega_{\text{max}}]$ yields the number of electrons n passing a shell of thickness r ,

$$n[\omega(r); \omega_{\text{max}}] = 2\pi \frac{N_e e^4}{m_e c^2} \cdot \frac{Z_{\text{eff}}^2}{\beta^2} \left[\frac{1}{\omega(r)} - \frac{1}{\omega_{\text{max}}} \right]. \quad (4.14)$$

Here $\omega(r)$ is the minimal energy of an electron needed to pass a distance of r .

By combining Equation 4.12 and Equation 4.14 one receives the energy deposited in a shell, division by the shells mass yields the deposited dose D_{δ} .

$$D_{\delta}(r, \beta, Z_{\text{eff}}) = \frac{N_e e^4}{m_e c^2} \cdot \left(\frac{Z_{\text{eff}}}{\beta} \right)^2 \cdot \frac{1}{\rho} \cdot \frac{1}{\alpha} \cdot \frac{1}{r} \left(1 - \frac{r}{r_{\text{max}}} \right)^{\alpha^{-1}} \quad (4.15)$$

Equation 4.15 yields the dose to a point, thus mimicking a physical radial dose distribution. The average dose to an extended target can be obtained by convoluting the target geometry with the *physical radial dose distribution*, yielding an *effective radial dose distribution*. For simplicity a cylindrical targets with an radius a_0 and the symmetric axis parallel to the ion trajectory is postulated. As illustrated in Figure 4.3 the area $dA = 2\phi t dt$ of

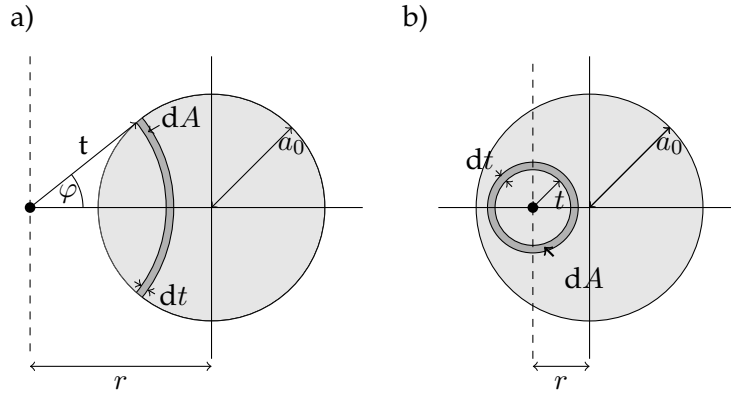


Figure 4.3: Geometrical consideration for the determination of dose to extended targets. In case a) $r + t > a_0$, case b) $r + t \leq a_0$. Graph adapted from [Hansen, 1984]

the cylinder with its centre in distance r to the ion path receives the same dose [Katz et al., 1972a]. Thus the average dose to the extended target at distance r from the ions path $\bar{D}_\delta(r)$ is given as

$$\bar{D}_\delta(r, \beta, Z_{\text{eff}}, a_0) = \frac{1}{\pi a_0^2} \int_{r-a_0}^{r+a_0} D_\delta(t, \beta, Z_{\text{eff}}) 2\varphi t dt \quad . \quad (4.16)$$

Insertion of Equation 4.16 in Equation 4.9 yields the activation cross-section for an extended target.

The relative effectiveness

Butts and Katz did not distinguish between relative effectiveness and relative biological effectiveness. They defined the effectiveness of a detector towards radiation i relative to a radiation j as the ratio of the sensitivities κ of the detector towards the radiation, respectively.

$$\eta_{i,j} = \frac{\kappa_i}{\kappa_j} \quad (4.17)$$

In the case of an one-hit detector the sensitivity equals the characteristic dose. Thus for a one-hit detector Equation 4.17 yields:

$$\eta_{i,\gamma} = D_{37}^\gamma \cdot \sigma_i \left(\frac{S}{\rho} \right)^{-1} \quad (4.18)$$

Ion-kill/ γ -kill

The presented model had been developed for one-hit detectors. It is not sufficient to describe the response behaviour of detectors which show multi-hit,

or multi-target characteristics, *i.e.*, a value large one for the n and/or m parameter in Equation 4.5. To account for the different characteristic the so-called *ion-kill*/ γ -*kill* concept was introduced [Katz et al., 1971].

The concepts differentiates between elements which show an effect directly due to a single traversing ion (*ion-kill*) and elements which are affected due to a cumulative effect of overlapping particle tracks (γ -*kill*). Even though attributed to δ -rays, the latter mode is called γ -*kill* since the relative effectiveness of this mode is set to unity, equal to γ -rays. A fraction of σ/σ_0 of the deposited dose is allocated for the ion-kill mode and the remaining dose fraction $(1 - \sigma/\sigma_0)$ is allocated to the γ -kill mode. σ denotes the activation cross-section as calculated in Equation 4.9 and σ_0 denotes the *saturation cross-section* which is empirical determined. Be $\Pi_{\text{ion}} = e^{-\sigma\Phi}$ the probability for an element not to be affected by the ion-kill mode, and Π_γ the probability of not being affected by the γ -kill mode then

$$\frac{N}{N_0} = \Pi_{\text{ion}} \times \Pi_\gamma \quad (4.19)$$

gives the probability of a sensitive element to not be affected. Here N denotes the number of affected elements and N_0 the number of total elements. Since the response of a detector system depends on the amount of activated elements the detector response S of a system described by the ion/ γ -kill mode equals

$$S = 1 - \Pi_{\text{ion}} \times \Pi_\gamma \quad (4.20)$$

The introduction of the γ -kill mode allows to describe the response of cells [Katz et al., 1971, Katz, 1978] but also physical multi-hit detectors as TLDs [Edmund et al., 2007]. However, the physical and biological motivation remains controversial. An overview on the discussion can be found in [Katz, 2003, Scholz and Kraft, 2004].

In this thesis only one-hit detectors are investigated thus the γ -kill approach is not applied and will not be further discussed.

4.4 The relative effectiveness for one-hit detectors

Following TST the resulting dose response relation of an one-hit detector shows itself an exponential behaviour, only with a different characteristic dose. The implications on the definition on the RE are discussed in this section.

Given an one-hit detector with a characteristic dose towards a reference radiation of $D_{37,\gamma}$ and a characteristic dose towards a test radiation of $D_{37,x}$. Target theory assumes a finite number of active elements and thus a maximal detector signal which is independent from the radiation quality. To keep the definitions as general as possible a saturation detector signal of S_0^γ for the reference radiation and S_0^x for the test radiation are assumed.

The definitions of the RE given in Section 3.7 can then be transformed by inserting the one-hit response characteristic. The iso-dose definition (Equation 3.10) yields

$$\begin{aligned}\eta_{\text{iso-dose}} &= \frac{S_x(D)}{S_\gamma(D)} \\ &= \frac{S_0^x \left(1 - e^{-\frac{D}{D_{37}^x}}\right)}{S_0^\gamma \left(1 - e^{-\frac{D}{D_{37}^\gamma}}\right)}\end{aligned}\quad (4.21)$$

$$\approx \frac{S_0^x}{S_0^\gamma} \cdot \frac{D_{37}^\gamma}{D_{37}^x}, \quad \text{for } D \ll D_{37} \quad . \quad (4.22)$$

The iso-response (Equation 3.9) yields

$$\begin{aligned}\eta_{\text{iso-response}} &= \frac{RED_{\text{ref}}}{D} \\ &= \frac{-D_{37}^\gamma \ln\left(1 - \frac{S_x(D)}{S_0^\gamma}\right)}{D}\end{aligned}\quad (4.23)$$

$$\begin{aligned}&= \frac{-D_{37}^\gamma}{D} \cdot \ln\left[1 - \frac{S_0^x}{S_0^\gamma} \left(1 - e^{-\frac{D}{D_{37}^x}}\right)\right] \\ &= \frac{D_{37}^\gamma}{D_{37}^x}, \quad \text{for } S_0^x = S_0^\gamma \quad .\end{aligned}\quad (4.24)$$

In the case of an identical saturation signal both definitions yield the same numerical value doses low compared to D_{37} . For higher doses however $\eta_{\text{iso-dose}}$ approaches asymptotically $S_x(D)$ and finally becomes one, while $\eta_{\text{iso-response}}$ stays constant.

In the case of different saturation signals $\eta_{\text{iso-dose}}$ still approaches asymptotically $S_x(D)$ but the RE is reduced by the saturation signal ratio. $\eta_{\text{iso-response}}$ decreases for high doses if $S_0^\gamma > S_0^x$. If the saturation signal of the test radiation is higher than for the reference radiation $\eta_{\text{iso-response}}$ becomes undefined.

4.5 Model by Hansen and Olsen

J. W. Hansen and K. J. Olsen adapted the track-structure model for one-hit detectors and applied it to dye films and alanine dosimeters.

Besides the determination of model parameter as D_{37} , they introduced some changes, which are listed below. This points are addressed in the main publication on the model [Hansen and Olsen, 1984] and in the PhD thesis of Johnny W. Hansen [Hansen, 1984]. Later a model for the calculation of the signal stability for alanine has been added [Hansen and Olsen, 1989] which is also introduced in this section.

Deviations from the original TST

The main change compared to the model by Butts and Katz is in the formulation of the radial dose distribution (RDD). Under the assumption of an infinitesimal short track-thickness dT , the integral of the dose to a point-target (Equation 4.15) should be identical with the stopping force which is not the case. The integrated point-target distribution yields values lower than the stopping force. The deduction of Equation 4.15 included some approximations *inter alia* the negation of the interaction of the projectile with nuclei of the material and the binding energy of the electrons. These assumptions mainly affect the region close to the projectile trajectory. The model attributes the difference in energy to these approximations and thus adds the missing energy to the region where the distance r from the particle trajectory is lower than the size of the active element a_0 . This creates a *core* with increased dose D_{core} compared to the distribution given in Equation 4.16. The amount of the difference between the formulations varies for different energies of the primary ion as shown in Figure 4.4.

Note, that the term *core* here refers to the region close to the target trajectory with constant dose due to the extension of the target in an effective RDD and is used out of convenience. It does not reflect the use of the *core/penumbra* model in the description of the physical RDD to a point target.

The final formulation of the RDD used in the model is:

$$D(r) = \begin{cases} D_{\text{core}} & : r \leq a_0 \\ \bar{D}_\delta(r) & : a_0 < r < r_{\text{max}} \\ 0 & : r > r_{\text{max}} \end{cases} \quad (4.25)$$

where \bar{D}_δ is the the extended target distribution (Equation 4.16) and D_{core} is chosen thus that

$$D_{\text{core}} = S/\rho - 2\pi \int_{a_0}^{r_{\text{max}}} \bar{D}_\delta(r) r dr \quad (4.26)$$

The formulation in Equation 4.25 resembles the formulation by Chatterjee and Schaefer [Chatterjee and Schaefer, 1976]. It differs however in essential points. First the Chatterjee RDD has a core-radius which is proportional to the projectile speed while here the radius a_0 is considered to be a material property and thus is fixed. Second the Chatterjee *a priori* attributes 50 % of the LET to the core region and the other half to energy deposition through electrons similar to Equation 4.15.

A further change regarding the RDD is the calculation of the maximal track extension. It follows Equation 4.14. However, fitting Equation 4.12 to experimental data they received a value for α of 1.676 and found that the k factor is proportional to the reciprocal of the density of the target medium [Hansen and Olsen, 1984].

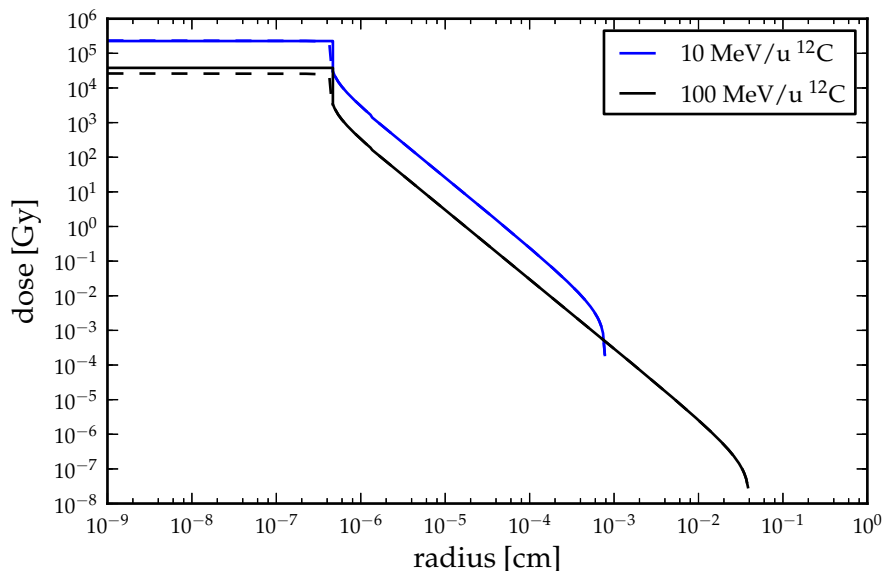


Figure 4.4: Radial dose distribution as a function of the distance from the particle track for carbon ions of 10 MeV/u and 100 MeV/u in alanine. The dashed lines represent the RDD resulting from Equation 4.16. The solid lines represent the RDD adapted to the stopping force as described in Equation 4.25.

An other detail is the calculation of the effective ion charge Z_{eff} which contributes to the height of the radial dose distribution and the stopping force calculations. Hansen and Olsen used the parametrisation by Ziegler [Ziegler, J. F., 1977], which differentiates between protons, helium ions, lithium ions and heavier ions for the calculation of Z_{eff} .

Model for signal stability

The electron paramagnetic resonance (EPR) signal in alanine is fading due to recombination of radicals. This process depends on the concentration, and thus average distance of radicals. The amount of radicals produced is dependent on the applied dose, and thus also the signal stability. As discussed previously a traversing HCP results in a local dose distribution with high differences in local dose, implying that also the concentration of radicals varies around a particle track. A higher signal fading for HCP than for equivalent photon doses was observed and attribute to this concentration pattern.

Given a function $K(t, D)$ describing the percentile signal fading as function of time t and dose D a recombination cross-section $\sigma_R(t)$ as function of

time can be derived similar to Equation 4.9.

$$\sigma_R(t) = \sigma \cdot \frac{1}{r_{max}} \int_0^{r_{max}} K(t, D(r)) dr \quad (4.27)$$

Here σ denotes the activation cross-section, r_{max} the maximal range of a secondary electron and $D(r)$ the dose at a distance r from the trajectory of the primary particle.

The response equivalent detector response RED as a function of time t can be expressed as

$$\begin{aligned} RED(t) &= D \cdot \eta(t) \\ &= D \cdot D_{37}^\gamma \cdot \sigma_R(t) \cdot \left(\frac{S}{\rho}\right)^{-1} \end{aligned} \quad (4.28)$$

Hansen and Olsen determined the function $K(t, D)$ from alanine irradiation with 10 MeV electrons. They found that $K(t, D)$ resembles a second order polynomial of t . This model showed general agreement with measured response data from HCP irradiation [Hansen and Olsen, 1989].

5. The alanine detector

Alanine is the model system for the detector response calculations presented in this thesis. The experiments described have been conducted with alanine dosimeters.

The amino-acid L- α -alanine ($\text{CH}_3\text{CH}(\text{NH}_2)\text{COOH}$) (see Figure 5.1) is the simplest amino acid. Pristine, it appears in crystalline form. Its use as dosimeter was first described by Bradshaw *et al.* in 1962 [Bradshaw *et al.*, 1962]. It has been used for dosimetry since. Dosimetry with alanine is based on radical formation induced by irradiation and quantified by the EPR method.

α -alanine exists in different configurations (D, DL, L and β), of which the L- α -alanine is the most used due to high signal yield and low zero dose signal [Regulla and Deffner, 1982]. Pure alanine powder can be used for dosimetry. Commonly, the powder is blended with a dry binding agent as paraffin wax [Arber and Sharpe, 1993], polyethylene [Gall *et al.*, 1996], cellulose [Hansen, 1984] or polyvidone [Hansen *et al.*, 1987] and processed into an appropriate form. This can be the form of rods, pellets or films. Binding agents are required to have minimal influence on the EPR signal. In order to increase the sensitivity of alanine blends with other materials *e.g.* boron or gadolinium are used [Marrale *et al.*, 2007, Marrale *et al.*, 2011].

Alanine has also been used in gel form [Olsson *et al.*, 2002, Ciesielski *et al.*, 1988], the advantage of possible three dimensional dosimetry is bought with inconveniences at the EPR readout, since the samples have to be dried or frozen [Olsson *et al.*, 1996].

Dosimetry with alanine is considered to be suitable as transferable and reference standard for photon dosimetry [ICRU, 2008, ISO/ASTM, 2002, ISO/ASTM, 2004]. It is also used as secondary standard [Anton, 2005] and has been applied for audit of radiotherapy units [Schaeken *et al.*, 2011,

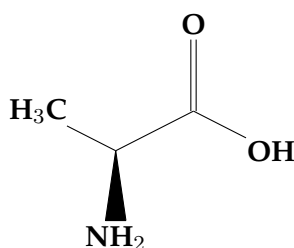


Figure 5.1: Structural formula of L- α -alanine

Budgell et al., 2011]. Alanine even is used as *in vivo* dosimeter for brachytherapy [Schaeken and Scalliet, 1996, Schultka et al., 2006].

5.1 Detection mechanism

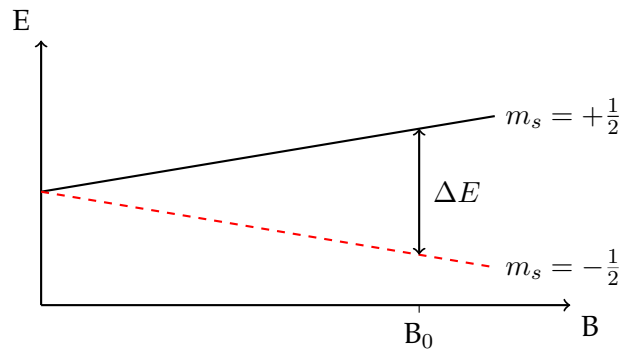


Figure 5.2: Schematic drawing of the split of the energy level for two different spins of a free electron in a magnetic field with flux density B as described in Equation 5.1.

Radical formation

Under irradiation a chemical radical formation process is induced in alanine, which results in a dissociation of alanine into radicals, molecules with an unpaired electron. While there is a dominant radical produced by deamination, which accounts for $\approx 60\%$ of the total amount of radicals [Malinen et al., 2003b], two further radicals have been identified [Sagstuen et al., 1997].

The contribution of the radical types to the absolute measured signal depends on the readout settings [Malinen et al., 2003a]. The radicals are considered to have different stability characteristics over time [Koizumi et al., 1996] and when heated up [Malinen et al., 2003a]. Their relative production may depend on the radiation quality [Malinen et al., 2003b, Ciesielsk et al., 1998].

Electron paramagnetic resonance spectroscopy

The electron paramagnetic resonance (EPR) spectroscopy or also called electron spin resonance (ESR) spectroscopy has been discovered 1944 by Y. K. Zavoisky. It can be used to determine the amount of radicals in a solid. This method uses the splitting of energy levels of an electron in a magnetic field, the anomalous Zeeman effect.

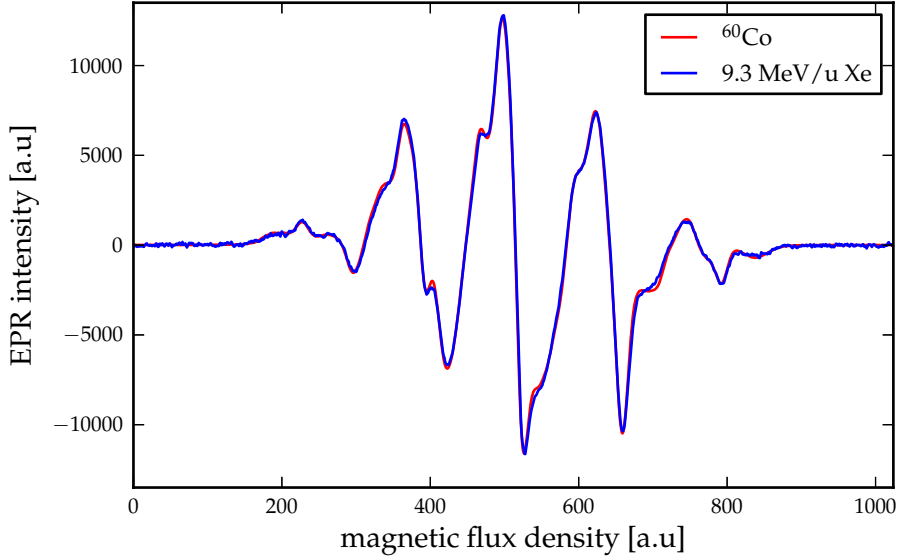


Figure 5.3: First derivative of an EPR absorption spectra as a function of the magnetic flux density of two irradiated alanine samples. The red spectrum originates from a dosimeter irradiated with γ -rays from a ^{60}Co source, the blue spectrum is due to irradiation with 9.3 MeV/u xenon ions. The absorbed dose to water in the pellet irradiated from a ^{60}Co source was 12 kGy.

Unpaired electrons align their magnetic momentum in an external magnetic field. The energy difference ΔE of the two spin states and thus magnetic orientations in a magnetic field can be described as

$$\Delta E = \mu_B g_e B_0, \quad (5.1)$$

where μ_B denotes the Bohr magneton, g_e the Landé factor of an electron and B_0 the magnetic flux density. The relation is illustrated in Figure 5.2, where m_s denotes the spin quantum number of the electron. Given the electrons are Boltzmann distributed in a thermal equilibrium, more electrons will be in the state with lower energy. Thus, if an electromagnetic wave fulfils the resonance condition ($\Delta E = h\nu$), part of it gets absorbed while lifting electrons into the higher energy level. The absorption of the electric field is an measure for the amount of unpaired electrons.

Since the modulation of the flux density of a magnetic field is technical easier to accomplish than the modulation of a stable high frequency (HF) wave, commonly the frequency is fixed and the HF field is generated by a klystron. An absorption spectrum is recorded by measuring the absorption while scanning the magnetic field strength linear.

Commonly the first derivative of the absorption spectrum is used. Fig-

Figure 5.3 shows such derivative spectra for two different radiation types. The resonance peak in the EPR spectrum is split due to the hyperfine interaction between the unpaired electron and nuclear magnetic moments. The peak-to-peak amplitude is proportional to the total amount of radicals per mass, if the shape of the spectrum does not change, which is assumed for average doses. To determine the total amount of radicals the integral of the spectrum has to be taken and to be compared with a reference sample where the amount of radicals is known. This method is less precise for low doses and more labour-intensive, since the whole spectrum has to be scanned, contrary to just the peak region. However, if the shape of the spectrum changes it is preferable [Ahlers and Schneider, 1991].

As seen in Figure 5.3 the first derivatives of absorption spectra for different beam qualities deviates at the non-centre peaks. These changes in the spectrum shape could be due to a change in the ratio of radiation induced radical species or due changes in the environment around radicals due to damages to the crystal lattice, or both.

5.2 Dosimetric characteristics

Alanine characteristics in photon and electron beams

The exponential behaviour of the alanine detector response on dose $S(D)$ has first been described by Roblat and Simmons [Roblat and Simmons, 1963]. It mimics the one-hit characteristics stated in Equation 4.3 and is well described by the following equation

$$S(D) = S_0 \left(1 - e^{-\frac{D}{D_{37}}} \right) \quad , \quad (5.2)$$

where S_0 denotes the maximum detector response, D the dose and D_{37} the characteristic dose of the detector. The value of D_{37} towards ^{60}Co is in the order of 100 kGy. The actual value of D_{37} varies at different authors. A collection of values directly or indirectly given in literature is shown in Table 5.1, together with the acquiring method where known. The deviation between the authors may be due to different alanine type or binding agent.

With a D_{37} value in the order of 100 kGy the alanine dose response can be approximated to be linear in clinical settings with less than 0.5 % deviation from linearity for a dose of 100 Gy. Be $S_{lin}(D)$ a linear dose-response relation and $S_{nlin}(D)$ a non-linear relation then we define the deviation from linearity as

$$dev_{lin} = 1 - \frac{S_{lin}}{S_{nlin}} \quad (5.3)$$

However, the saturation of alanine is not reached by activation of all possible active centres, as assumed in target theory. Saturation in alanine is an equilibrium between radical producing processes and processes leading to

author	D ₃₇ [kGy]	method
Bartolotta ^a <i>et al.</i> [Bartolotta <i>et al.</i> , 1984]	72.6 ± 1.6	p2p
Bermann ^b	110.0	
Kojima ^a <i>et al.</i> [Kojima and Tanaka, 1989]	81.0 ± 2.6	p2p
Krushev ^a <i>et al.</i> [Krushev <i>et al.</i> , 1994]	195 ± 15.4	
Hansen and Olsen [Hansen and Olsen, 1985]	105.0	p2p
Regulla ^a [Regulla and Deffner, 1982]	207.7 ± 5.7	p2p
Snipes and Horan [Snipes and Horan, 1967]	120.4	
Waldeland <i>et al.</i> [Waldeland <i>et al.</i> , 2011]	56.6	p2p
Waldeland <i>et al.</i> [Waldeland <i>et al.</i> , 2011]	87.1	integral
Waligórski ^b <i>et al.</i> 1981	75.0	
NPL Batch 65	63.1 ± 0.3	p2p

Table 5.1: D₃₇ values as found in literature. *p2p* denotes measurements at which the peak-to-peak amplitude has been used as measure, *integral* if the integral of the EPR spectrum has been used.

^adata extracted from graph in paper, uncertainty due to fitting procedure.

^boriginal article not available, value given in Waligórski *et al.* [Waligórski *et al.*, 1989]

a radical deterioration [Rotblat and Simmons, 1963, Snipes and Horan, 1967, Hansen and Olsen, 1985, Olko, 1999]. The maximum fraction of alanine molecules transformed into radicals has been measured to be 0.365 % [Rotblat and Simmons, 1963]. This number agrees in its order of magnitude with calculations done by Olko [Olko, 1999]. He calculated, that at saturation dose an energy of 210 eV has been deposited in a 6 nm sphere containing approximately 760 alanine molecules. A required energy of 51 eV [Rotblat and Simmons, 1963] or 60 eV [Hansen and Olsen, 1985] for initiation of radical formation results in a radical fraction of 0.526 % and 0.461 %, respectively.

Following Rotblat and Simmons one assumes a constant radical creation rate λ_+ and a deterioration rate λ_- that is linearly dependent on the amount of existing radicals N . The produced radicals per deposited dose D can be described as

$$\frac{dN}{dD} = \lambda_+ - \lambda_- N \quad . \quad (5.4)$$

Solving this differential equation yields

$$N = \frac{\lambda_+}{\lambda_-} \left(1 - e^{-\lambda_- D} \right) \quad . \quad (5.5)$$

Comparing with Equation 5.2 one finds that the maximum response S_0 is the ratio of radical creation to destruction rate and λ_- is the multiplicative

inverse of the characteristic dose D_{37} . Implication for the maximal response S_0 are discussed in a later section.

The detector effectiveness of alanine relative to ^{60}Co is below unity for X-rays between 50-200 kV [Waldeland et al., 2010]. For 4 and 6 MV γ rays as well as 6 and 20 MeV/u electrons an identical detector sensitivity has been reported [Hansen and Olsen, 1985]. However, recently a correction factor of 1.012 ± 0.010 for electrons between 6 and 22 MeV has been found [Vörös et al., 2012].

No significant dose rate dependency is known for rates up to $5 \cdot 10^7$ Gy/s.

Alanine characteristics in hadron beams

Already Bradshaw *et al.* in 1962 irradiated alanine with proton beams and found a different sensitivity towards proton beams than towards ^{60}Co radiation [Bradshaw et al., 1962]. The measured RE of alanine for ion beams is always equal or below unity in accordance with TST. Section 5.4 gives an overview on effectiveness measurements for ion beams.

Saturation signal of alanine

Following TST and target theory the maximal detector signal S_0 should be equal for all radiation qualities. This is based on the assumption, that there is a finite number of active elements, which, at full saturation, are all activated.

Following Equation 5.5 S_0 should change in the same way as the sensitivity of the detector changes towards different radiations. The ratio of the maximum response of two radiation qualities would then equal the relative effectiveness as defined in Equation 4.17. κ_i being $1/D_{37}^i$, or λ_-^i in the nomenclature of Equation 5.5.

The alanine detector mimics a one-hit detector, but as already pointed out by others [Hansen and Olsen, 1985, Olko, 1999], it does not fulfil all postulates of target theory, since by far not all possible *active elements* contribute to the detector signal at saturation. Krushev [Krushev et al., 1994] even observed a decline in the signal after a dose of 0.8 MGy applied with ^{60}Co γ -rays. A similar behaviour has been observed by Henriksen [Henriksen, 1966].

Hansen and Olsen [Hansen and Olsen, 1985] reported a maximal response dependent on radiation type, which they later on [Olsen and Hansen, 1985] speculated could be due to dose rate effects.

For heavy ions the response as function of dose is – to the knowledge of the author – only determined by Hansen and Olsen [Hansen and Olsen, 1985] up to saturation dose. For 2.5 MeV/u oxygen and 4 MeV/u sulphur ions the decrease of the signal at very high doses is reported. The extracted data is shown in Figure 5.4. The lines are fits, the solid line is a fit following the one-

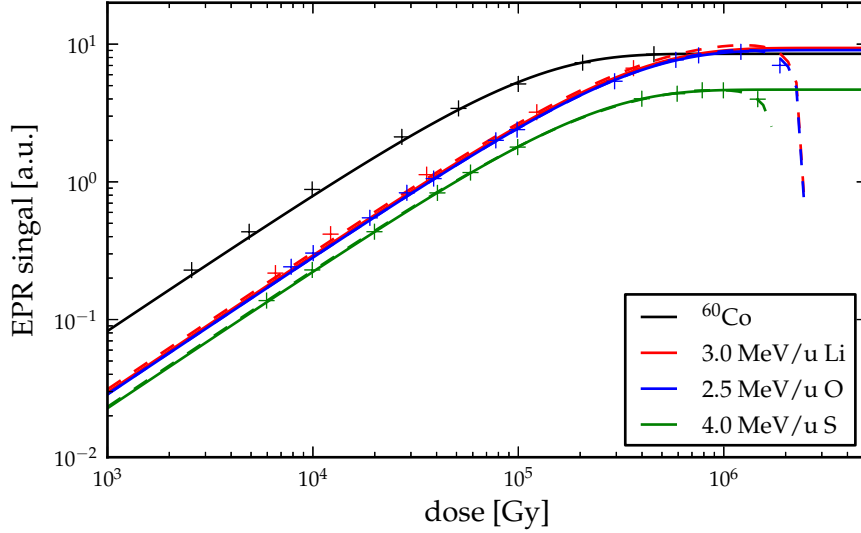


Figure 5.4: The dose-response behaviour of alanine for different ions. Data points are extracted from reference [Hansen and Olsen, 1985]. The solid lines represent fitted one-hit response functions, the dashed lines are fitted with Equation 5.6.

hit characteristic. For this fit the data points after the maximum response have been excluded. The dashed line shows a fit to function

$$f(D) = S_0 \left(1 - \exp \left[-D/x_1 + (D/x_2)^2 \right] \right) \quad (5.6)$$

The reason of the decline of the detector signal at very high doses is not clear yet. It may be due to enhanced signal fading, or, in the picture of Equation 5.5, the radical production rate λ_+ may also be dependent on the existing amount of radicals.

While the ratio S_0^{ion}/S_0^{60Co} for sulphur ions equals the RE and thus would support Equation 5.5 the maximal response for oxygen ions is even above the maximal response towards ^{60}Co which is a finding contrary to theory and not supported by other measurements. As seen in in Figure 5.5 the saturation level influences the behaviour of the the relative effective as a function of dose for high doses.

Signal stability

The signal readout of alanine detectors with the ESR method is non-destructive and can be repeated *ad libitum*, which makes alanine systems a candidate for inter-laboratory comparison. However, radicals

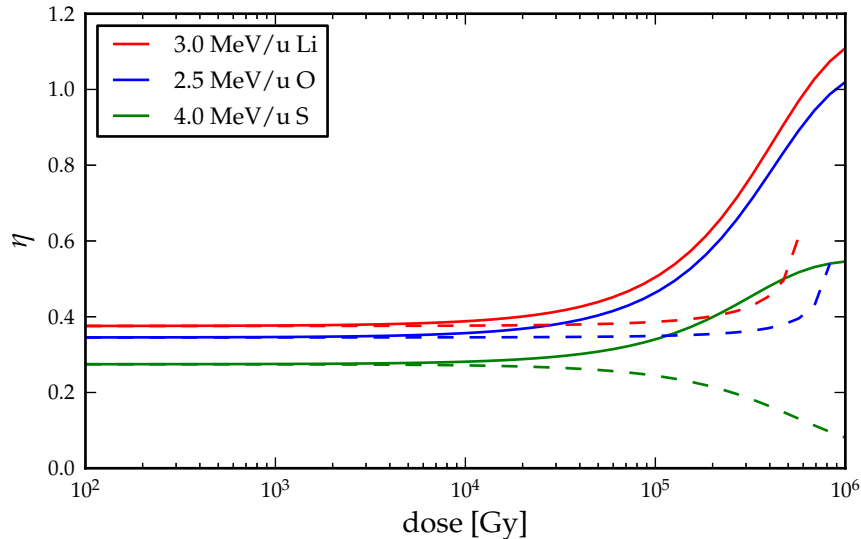


Figure 5.5: The relative effectiveness corresponding to the data represented in Figure 5.4. The solid lines are calculated following the iso-dose definition, the dashed lines are calculated following in iso-response definition.

are meta-stable. Radical recombination is hampered by the distance between radicals and by being embedded in a solid, but is not prohibited. With disappearance of radicals, also the detector signal fades. The fading process is reported to be a two stage process [Hansen et al., 1987, Kojima et al., 1992], attributed to the different radical species in the samples. Several factors have an influence on the signal fading, namely, dose, humidity, pre-irradiation storage [Arber and Sharpe, 1993], temperature, ambient light [Hansen and Olsen, 1989, Wieser et al., 1993], radiation quality [Hansen et al., 1987], temperature, dosimeter composition and even detector shape [Sleptchonok et al., 2000]. While the signal fading generally is regarded as being negligible at moderate doses (below a few kGy) [ICRU, 2008, Regulla, 2009], Sleptchonok *et al.* [Sleptchonok et al., 2000] expressed some doubts after a meta-study and own experiments. They concluded, that fading has to be considered.

The signal fading for alanine detectors irradiated with particles has been reported to be more pronounced than the fading for photons at same dose levels, which is attributed to the high dose regions in the particle track [Hansen et al., 1987, Hansen and Olsen, 1989, Olsen and Hansen, 1990]. Based on their model for response prediction in particle beams Hansen and Olsen developed a model for prediction of signal fading [Hansen and Olsen, 1989]. Figure 5.6 shows the predicted signal

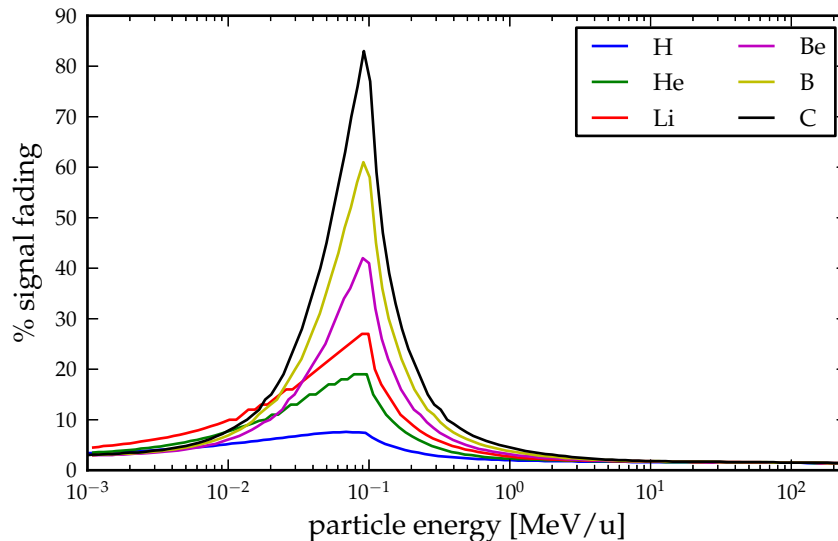


Figure 5.6: Percentage signal fading in alanine 800 h after irradiation as a function of particle energy. The signal fading has been calculated with the model by [Hansen and Olsen, 1989].

fading 800 h after irradiation in percent for the lightest six ions as a function of particle energy. However, the fading reported by their group has been observed at very high dose and low – in terms of range – particle energies, *e.g.* 16 % signal fading for 16 MeV/u proton beams at a dose of 0.5 MGy and 22 % signal fading for 3 MeV/u lithium ions at a dose of 1 MGy after 4000 h [Hansen et al., 1987]. Recent experiments with carbon ions at doses below 100 Gy did not show signal fading in a time period from 8 to 660 h after irradiation [Herrmann et al., 2011b].

5.3 The NPL alanine dosimeter

The alanine measurements which are presented in this work have been conducted with alanine pellets provided by the National Physical Laboratory (NPL). These pellets are produced by Harwell Dosimeters Ltd. They consist of 90.9 % by weight L- α -alanine and 9.1 % by weight high melting point (98°C) paraffin wax. The average mass density is 1.23 g/cm³. The detectors have a thickness of 2.27 mm and a diameter of 5.05 mm. Dosimeters are conditioned at 55% relative humidity for 10 weeks prior to use in order to reduce post-irradiation fading. They are calibrated towards dose to water in a ⁶⁰Co field, the recommended dose range is from 5 Gy to 70 kGy [Sharpe and Septhon, 1999]. Figure 5.7 shows the dose response char-

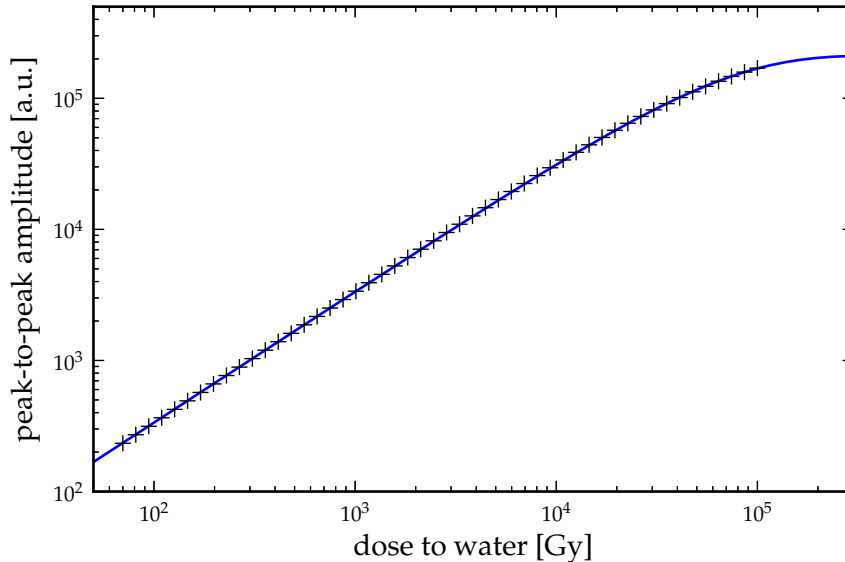


Figure 5.7: Peak to peak amplitude of the first derivative of a EPR absorption spectrum of alanine as a function of absorbed dose to water. Measured for the NPL alanine dosimeters, batch 65, irradiated with ^{60}Co emitted γ -rays. The black crosses indicate the measured values, the blue line a fit according to Equation 5.2.

acteristic of the detectors, measured with the peak-to-peak method. The graph includes a fit following the one-hit characteristic Equation 4.3. The characteristic dose D_{37} resulting of the fit is 63.1 kGy.

Irradiations should be conducted at temperatures below 70 °C. A deviation from reference temperature results in a signal difference of 0.143% per °C [Sharpe et al., 2009]. The pellets are not perfect cylindrical, the edges are slanted. While this does not influence photon dosimetry it has an impact when aligning pellets for depth dose measurements in particle beams [Herrmann et al., 2011b]. The detector readout is done following the standard procedure as described in [Sharpe and Septhon, 1999].

5.4 Literature data

Experimental determinations of the RE of alanine in ion beams have been conducted earlier by different authors.

Two different kinds of relative effectiveness data sets exist. The first variant is the dose response of alanine towards a selected beam quality *e.g.* particle and particle energy, which allows to determine the RE as a function of dose. The second variant is the RE of alanine as function of the particle en-

label	author
a	Bartolotta <i>et al.</i> [Bartolotta et al., 1999]
b	Bradshaw <i>et al.</i> [Bradshaw et al., 1962]
c	Cuttone <i>et al.</i> [Cuttone et al., 1999]
d	Ebert <i>et al.</i> [Ebert et al., 1965]
e	Fattibene <i>et al.</i> [Fattibene et al., 2002]
f	Olsen <i>et al.</i> [Olsen and Hansen, 1990]
g	Onori <i>et al.</i> [Onori et al., 1997]

Table 5.2: Legend of Figure 5.8

ergy. Since the measurements are always bound to particle energies provided by available accelerators, for the second variant just a view systematical data points for ion species are available, namely for protons and carbon ions. A collection of data of alanine relative effectiveness in different ion beams is compiled in Table A.5.

Dose-response curves for photons and electrons at different energies are reported by several authors. The only data set on a dose escalation study for particle irradiation –known to the author– was conducted by Hansen and Olsen [Hansen and Olsen, 1985].

Waligórski *et al.* [Waligorski et al., 1989] presented an overview over the data on the RE available in 1989. Where not explicit given, he extracted the values from the original articles, respectively. The data set includes protons, heavy ions and neutrons. In 1990 additional data for heavy ions were published [Olsen and Hansen, 1990]. To the knowledge of the author no relative effectiveness data for ions heavier than protons have been published since.

The most recent overview on data on the RE of alanine towards proton was published by Palmans *et al.* [Palmans et al., 2007], including preliminary, unpublished data from measurements at proton energies below 60 MeV. However, these data are only included in a graph, not listed.

Onischuk *et al.* [Onischuk et al., 2010] recently reported alanine irradiation with protons at energies between 6-25 MeV. However, they neither provide values of the RE, nor enough information to extract it from the given data. This also applies for depth dose measurements of protons beams with alanine reported by Nichiporov *et al.* [Nichiporov et al., 1995] and Gall *et al.* [Gall et al., 1996].

The existing data for protons stopping in the detector are scattered and partially contradict each other. They are shown in Figure 5.8.

Alanine measurements in antiproton beams have been reported by Bassler *et al.* [Bassler et al., 2008]. However, the RE here is given around the peak of an antiproton depth dose curve, thus in a strongly mixed radiation field. RE values for a single particle type can not be extracted from these

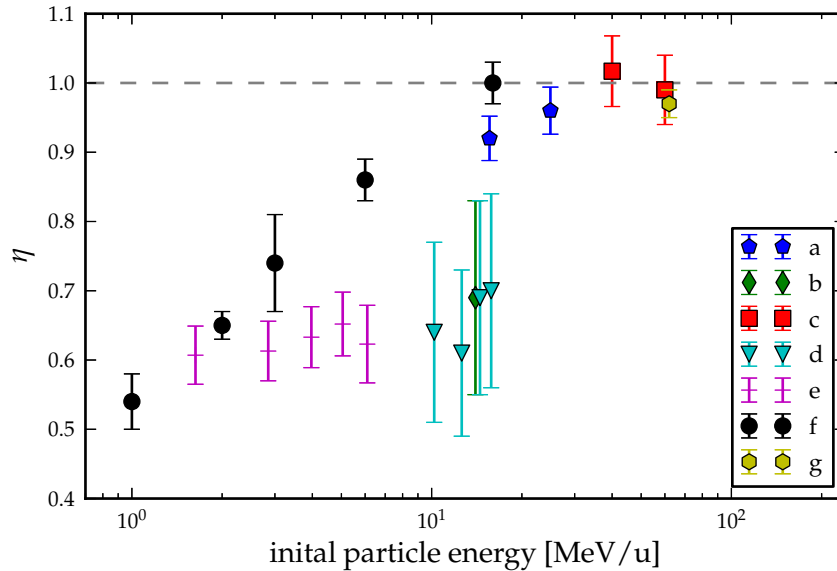


Figure 5.8: Relative effectiveness of alanine in proton beams as function of their initial energy. The authors are listed in Table 5.2, values in Table A.5, respectively.

measurements.

Response predictions for alanine

The one-hit characteristics, together with the high characteristic dose and the stable readout protocol make alanine a good candidate for a model system for amorphous track models (ATMs).

Previously other authors have calculated the RE of alanine. The first response prediction for alanine has been done by Katz *et al.* [Katz, 1978], they used their track-structure model to calculate the relative effectiveness of alanine in a 220 MeV/u oxygen ion beam.

Based on the model by Katz *et al.*, Hansen and Olsen [Hansen and Olsen, 1984], Waligòrski *et al.* [Waligòrski *et al.*, 1989] and Ohno *et al.* [Ohno *et al.*, 2001] calculated the RE of alanine and compared their results with measured data.

Olko [Olko, 1999, Olko, 2002] published calculations of the RE of alanine based on microdosimetric theories.

Palmans [Palmans, 2003] suggested a fit function for the RE for protons as a function LET weighted effective energy based on the available literature data.

However, due to the sparse RE data available for alanine at clinical relevant energies, these models have not been tested in clinical settings yet.

6. Introduction to experiments

The data on response behaviour of alanine in ion beams available in literature are not sufficient to pass judgement on a response model, even less on single aspects of it. In order to be able to investigate the influence of basic model assumptions further experiments have to be conducted in regimes, where these assumptions are dominating the final result of the model, respectively. Some experimental settings to extract information are

- i low LET particles at low fluences, especially in the energy range at which the RE approaches unity
- ii high LET particles at low fluences
- iii fluences at which the onset of track-overlap effects becomes measurable

Under the assumptions of TST, the implications of these constellations are explained in the following.

ad i: Experiments in this regime are suitable to investigate the validity of the RDD formulations in the *core* region.

The response of a perfect detector would be linear with dose, regardless of the applied dose, thus the RE would be unity for all particle energies.

A *semi-* perfect detector would have a linear dose-response up to a saturation dose D_{sat} and would then immediately be saturated. A detector like this would have a relative effectiveness of unity for particle energies at which the core dose is below or equal the saturated dose ($D_{\text{core}} \leq D_{\text{sat}}$).

Following the assumptions of TST the relative effectiveness of a one-hit detector becomes unity, when the maximal dose in a RDD is in the dose range, where the detector response can be assumed to be linear with dose, *ergo* $D_{\text{core}} \ll D_{37}$.

The results of response models in the energy region around and below the particle energy where the relative effectiveness of a detector becomes unity is thus very sensitive to the used parameterisation of the effective RDD and especially the value of D_{core} . Since most RDD models are normalised on the stopping force, D_{core} is determined through the choice of the a_0 -value.

ad ii: The influence of the model description of the *core* region of a RDD is minimal in beams of particles with a RDD that has an energy deposition close to the particle trajectory so high that saturation is reached in this part of the

detector. In this regime the maximal extension of the radial dose distribution influences the results of model calculations maximal.

ad iii: At high fluences the probability that a point in a detector receives dose contributions from more than one crossing particle increases. As long as the sum of dose contributions in a point is in a dose range, where the detector response is linear with dose the detector response and thus the RE is not influenced. If, however, the fluence is high enough, that the dose level is raised into the sub linear response range, the detector response is affected, the RE decreases.

Overlapping tracks can be neglected in alanine dosimeters over a wide fluence range, due to the high characteristic dose of alanine. The size of the region in a particle track with non linear dose response or even saturation is very small, thus a high fluence is required to see effects of overlapping tracks in alanine. The onset on these effects, however, is dependent on the maximal width of the RDD. Experiments in the fluence regime where overlapping tracks affect the detector response would be suitable for the determination of the maximal extension of the RDD.

For all experiments it would be desirable to be conducted in the track-segment regime, *i.e.* having a mono-energetic, single particle field in the detector. If the particles undergo significant energy loss additional factors, as particle transport influence the results. However, due to the finite detector thickness mono-energetic measurements in the track-segment regime are just possible for constellation i, *i.e.* particle energies with a penetration depth much higher than the detector thickness.

The saturation dose, and thus the D_{37} value, of a one-hit detector strongly influences its response-behaviour. Conducting response experiments with different one-hit detectors with different D_{37} would allow to isolate detector specific behaviour from artefacts introduced by basic assumptions of the TST.

In the following two chapters two experiments conducted during this PhD project will be introduced. Chapter 7 deals with experiments conducted with protons at energies between 110 to 220 MeV. These experiment is intended to fulfil the requirements of setting i and yield information on the a_0 value.

Chapter 8 presents an experiment with heavy ions at low energies. Besides the alanine detector, lithium formate detectors were employed. These detectors show a one-hit behaviour similar to alanine, but at a lower characteristic dose. This experiment was intended to fulfil setting ii and iii.

7. Proton irradiation

7.1 Methods

The Heidelberg Ion-Beam Therapy Center (HIT) is a synchrotron based medical facility which provides carbon ion beams with particle energies from 80 to 430 MeV/u and proton beams with particle energies from 50 to 220 MeV/u. Since November 2009 at HIT cancer patients are treated with carbon ions and protons.

Homogeneous radiation fields are created by the active raster-scan method, in which single Gaussian shaped pencil beams are superimposed. The method is considered to be *active*, since range modulation is achieved by energy modulation of the synchrotron. Beam delivery is called *passive* if the energy of a beam is degraded by inserting material.

Irradiations of alanine detectors have been conducted at the quality assurance (QA) beamline of the HIT facility. The room is kept at a constant temperature. The iso-centre of the beam is indicated by a laser system. The beam exits the beamline through an exit window and a monitoring system consisting of Multiwire Proportional chambers (MWPCs) and ionisation chambers. The water-equivalent path-length (WEPL) – the distance in water by which the particle range in water is reduced – of the beam exit system and the air distance to the iso-centre corresponds to 2.9 mm [Parodi et al., 2010].

Setup

Alanine detectors provided by NPL as described in Section 5.3 were used in this experiment. The readout was conducted at NPL, following the standard procedure.

In a single irradiation two alanine pellets were mounted in a polymethyl methacrylate (PMMA) holding plate, which was placed in front of a PTW¹ Markus Chamber of type 23343. The protection cap of the Markus chamber was mounted. The chamber was separated from the second pellet in beam direction by a Gafchromic film (see Figure 7.1).

The absorbed dose to water deposited in the Markus chamber $D_{w,Q}$ was determined following Equation 7.1 as recommended by the International Atomic Energy Agency (IAEA) [Andreo et al., 2004],

$$D_{w,Q} = M_Q \cdot N_{D,w} \cdot k_Q \quad . \quad (7.1)$$

¹PTW Freiburg GmbH (PTW)

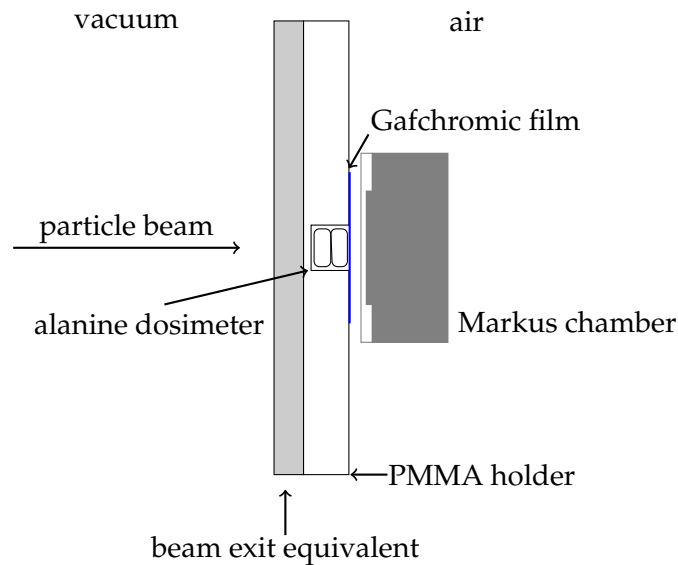


Figure 7.1: Schematic drawing of the geometry implemented in the FLUKA dose calculations.

M_Q denotes the corrected ion chamber reading and $N_{D,w}$ the calibration factor for ^{60}Co radiation as provided by the manufacturer. The ion chamber reading has been corrected for recombination, the factor has been determined using the two-voltage method described by Boag and Curren [Boag and Curren, 1980]. The value of the correction factor k_Q has been chosen according to the IAEA recommendations [Andreo et al., 2004]. The calibration factor of the Markus chamber is traceable to the Physikalisch-Technische Bundesanstalt (PTB) but the calibration of the alanine pellets is traceable to the NPL and thus to different primary standards. This factor of uncertainty is included in the calculations.

The irradiation fields were manually planned and consisted of an equally weighted superposition of pencil beams. The fields were designed to yield an area of homogeneous particle intensity of at least 1 times 1 cm² around the iso-centre, in which the pellets were placed. All detectors were irradiated with mono-energetic proton fields at particle energies from 110 to 220 MeV in steps of 10 MeV. The planned dose to the first detector in beam direction was 20 Gy.

Dose calculations

The Monte Carlo particle transport code FLUKA [Battistoni et al., 2007, Fassò et al.,] version 2011.2.11 has been applied for particle transport and energy deposition calculations.

The exact beam positions and particle numbers at each position were ex-

tracted from the accelerator log files. The beam shape as specified in the control files was used. The information was used for the definition of primary particles in FLUKA via a modified *source* user-routine. This routine allows to define individual radiation fields in FLUKA, other than the predefined. Scripts were written to extract the information from the accelerator log and control files and transform them into an appropriate format. This format is then read by a FLUKA executable, which has been compiled with the mentioned *source* user-routine.

The shape of a single pencil beam is assumed to be Gaussian. The full width at half maximum (FWHM) of the beam intensity distribution is used to describe it. This parameter is known at the iso-centre, whereas the known particle energy is the extraction energy of the synchrotron. Between these two positions are different materials in which the particles lose energy and undergo scattering. Here we follow the method proposed by Parodi *et al.* [Parodi *et al.*, 2010]. Since the information on particle scattering and thus beam widening in the beam exit (monitor system & exit window) and the air distance between beam exit and iso-centre is already included in the FWHM. These materials are not included in the simulations. To account for the energy loss in these elements a 2.9 mm slab of water is placed in front of the iso-centre [Parodi *et al.*, 2010]. The particle beams are assumed to be parallel, which is justified by the small field sizes used in the experiments. The momentum spread ($\Delta p/p$) is estimated to be $\approx 0.1\%$ and is included in the simulations.

In order to prevent the need for conversions from dose to air to dose to water in the Monte Carlo calculations, the Markus chamber has been replaced by a volume filled with water. The volume has the same area facing the beam as the sensitive volume of the chamber. At the effective point of measurement [PTW Freiburg, 2005] the dose has been scored. Thus the FLUKA calculations directly yield the dose to water as measured by the Markus chamber. This method has been previously applied for carbon ions [Herrmann *et al.*, 2011b].

7.2 Results

After irradiation the detectors were shipped to NPL and were read out there. As previously shown [Herrmann *et al.*, 2011b], signal fading can be neglected at the applied doses. The dose deposited in the alanine detectors was calculated with FLUKA, relative to the dose deposited in the Markus chamber. The dose measured with the Markus chamber has been multiplied by these ratios in order to obtain the dose in the pellets, respectively.

Following the iso-response definition of the RE (Equation 3.9) η is the ratio between the RED and calculated the dose. Figure 7.2 shows the measured RE as a function of the mean proton energy in a detector. Error bars in energy

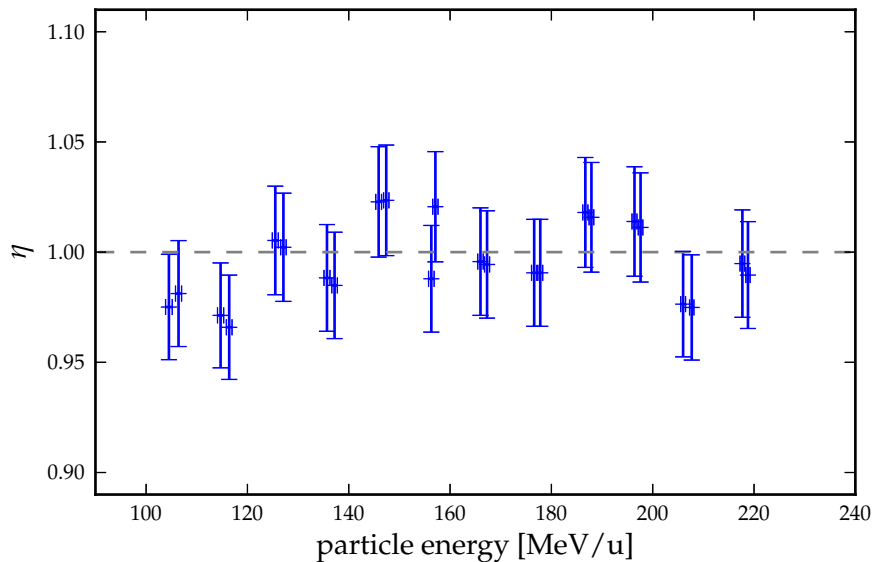


Figure 7.2: Measured relative effectiveness of alanine in proton beams as a function of the particle energy. Error bars in the energy direction indicate the width of the energy distribution (1σ) in a detector.

direction indicate the width (1σ) of the energy distribution in one alanine detector. The values are listed in Table A.2.

The standard uncertainty of the Markus chamber measurements in proton beams was estimated to be 2.4 % (1σ), following the recommendations in IAEA TRS-398 [Andreo et al., 2004]. The precision of the RED given by NPL is better than 0.05 Gy. The combined uncertainty on the measured RE values is 2.45 % (one-standard deviation).

7.3 Discussion

All but two measured values for the relative effectiveness are distributed around unity within their uncertainties (one standard deviation). They agree with the RE of unity for 160 MeV protons reported by Berman [Waligorski et al., 1989]. The RE for lowest two energies show a slight tendency to a value below unity, which can be interpreted as the onset of the transition to a RE below unity. This is in contrast to measurements by Olsen [Olsen and Hansen, 1990], Cuttone [Cuttone et al., 1999] and Onori [Onori et al., 1997] which report RE values of unity for lower energies. However, in consideration of the uncertainties of this measurement, as well as of the reported uncertainties by the other authors this is not significant.

The goal of the experiment to characterise the transition of the RE from

unity to lower values has not been fully achieved. The measurement of the RE for proton energies down to 50 MeV, which would be available at the HIT facility, was hindered by beam time limitations and shifts in the internal schedule of the facility.

8. Experiments with stopping particles

8.1 Material and Methods

The RADEF facility

At the Department of Physics of the University of Jyväskylä, Finland, a K-130 cyclotron is located, which provides beams for the RADiation Effect Facility (RADEF), an irradiation side for ion irradiation studies of semiconductor materials certified by the European Space Agency (ESA).

RADEF provides seven different ion species, xenon being the heaviest, with energies up to 9.3 MeV/u.

At RADEF the particle fluence is measured by a combined collimation and fluence measurement system, as schematically shown in Figure 8.1. The extracted particle beam is widened by wobbler magnets. The resulting radiation field is then shaped by four collimators. On each of these collimators a scintillation crystal is mounted. The scintillators are equipped with photomultipliers and have a counting area of 0.5 cm². The fluence in the target is estimated by the average of the fluences measured with the four scintillators [Virtanen, 2006]. The beam can either be extracted through an exit window or the target area can be evacuated thus eliminating the need for an exit window.

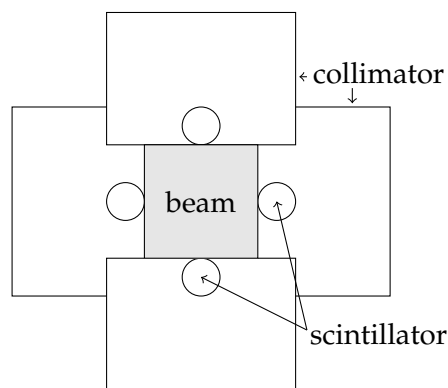


Figure 8.1: Sketch of the combined collimation and fluence measurement system at RADEF, following the description by Virtanen *et al.* [Virtanen, 2006]

Dosimeter

Alanine

Alanine pellets provided by NPL, as described in Section 5.3 were used. The pellets are part of batch 66 which shows the same dose-response behaviour as batch 65 [Sharpe, 2012].

Lithium formate

Irradiation of poly-crystalline lithium formate monohydrate ($\text{HCO}_2\text{Li} \cdot \text{H}_2\text{O}$) induces the building of stable radicals in the material, making it a candidate for ESR dosimetry. The ESR spectrum shows a single absorption peak and no disruption of the spectrum due to hyperfine coupling. Due to its high sensitivity it can be used at dose levels down to 0.5 Gy [Vestad et al., 2003, Vestad et al., 2004]

The dose-response characteristic of lithium formate after ^{60}Co irradiation mimics an one-hit detector and is well described by Equation 5.2. The characteristic dose D_{37} for peak-to-peak assessment of the EPR spectrum is 40.8 kGy and 53.5 kGy after evaluation of the area under the absorption spectrum [Waldeland et al., 2011].

The lithium formate detectors used in this experiment were provided and readout by The Norwegian Radium Hospital, Oslo University Hospital.

The peak-to-peak amplitude of the detectors were used for dose assessment. The amplitude was corrected for the fraction of irradiated volume using the penetration depth calculated with the methods discussed in Sub-section “range calculations”.

For calibration pairs of two lithium formate detectors were irradiated with 6 MeV electrons at known doses of 0.5, 1.0 and 2.0 kGy. The relative effectiveness of lithium formate towards MeV/u electron beams is 0.99 ± 0.03 [Malinen et al., 2007].

The assumption of linear dose response is not valid any more in dose levels reached in the experiment. It would introduce an error of 15% at a dose of 15 kGy. Therefore the one-hit response function (Equation 5.2) with the D_{37} reported from the same group [Waldeland et al., 2011] was fitted to the calibration data. Figure 8.2 shows the reference measurements and the fitted calibration curves, the linear regression in black and the one-hit characteristic in red. The inverse function of the one-hit fit was used to translate the corrected EPR signal into dose.

The stopping force of lithium formate was calculated applying Bragg’s additivity rule on stopping force values extracted from the SRIM 2011 code [Ziegler et al., 2010]. Since lithium formate is a monohydrate, the stopping force for the formate and the water molecule were determined separately and then combined following Bragg’s rule. This is done since water is a material that shows large deviations from Bragg’s rule [ICRU, 1993].

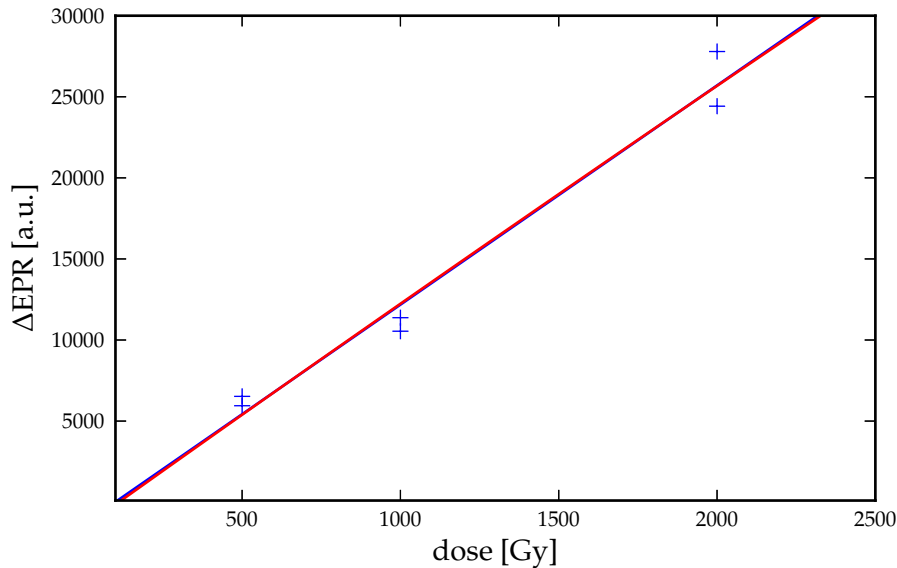


Figure 8.2: Peak-to-peak amplitude as function of dose of the lithium formate samples irradiated with electrons and used for calibration. The black line represents a linear fit to the data, the red line a fit of an one-hit dose response curve.

EPR readout

EPR detectors exposed to radiation fields which result in a homogeneous dose over the whole detector have a homogeneous radical distribution in the whole detector volume. During readout the detectors are carefully placed and the position of the EPR cavities is adjusted to face the maximal intensities of the HF electric field and the magnetic field.

In the here described experiment high dose gradients exist in the pellets, with a small part of the detector contributing the major part to the EPR signal. Thus the orientation of the pellet in the cavity may have an impact on the resulting readout. To correct for this effect the alanine detectors were readout twice, once in every orientation. The average of the measurements was used for dose determination.

Fluorescent nuclear track detectors

Fluorescent nuclear track detectors are doped aluminium oxide single crystals ($\text{Al}_2\text{O}_3:\text{C,Mg}$). When irradiated, existing colour centres are transformed into stable luminescent centres. These luminescent centres can be excited with light at a wave length of 620 nm and emit light at 750 nm. The readout with confocal microscopy is non destructive [Akselrod and Sykora, 2011].

ion	energy MeV/u
$^{15}\text{N}^{+4}$	9.3
$^{56}\text{Kr}^{+15}$	9.3
$^{82}\text{Fe}^{+22}$	9.3
$^{131}\text{Xe}^{+35}$	9.3

Table 8.1: Ions used for detector irradiation.

ion	Mylar [μm]	Kapton [μm]	E_{in} [MeV/u]	$E_{\text{out,SRIM}}$ [MeV/u]	E_{range} [MeV/u]
Fe	10.0	50.0	9.3	5.19	5.8
Kr	2.5	50.0	9.3	5.01	5.0
Xe	25.0	20.0	9.3	5.87	6.4

Table 8.2: Degradation material and thickness. $E_{\text{out,SRIM}}$ denotes the particle energy calculated based on the degradation thickness. E_{range} denotes the particle energy derived from the penetration depth in Al_2O_3 .

Accuracy of optical microscopy is limited by Abbe's law, which states that the best resolution achievable is half the wavelength of the light used for observation.

The used detectors were rectangular ($4 \times 6 \text{ mm}^2$) and $500 \mu\text{m}$ thick, they have a density of 3.97 g/cm^3 . The readout was conducted at the Deutsches Krebsforschungszentrum (DKFZ) following the procedure described by Greilich *et al.* [Greilich *et al.*, 2012b].

Experimental setup

The ions and their non-degraded energies used in the experiment are listed in Table 8.1. Degradation were created on side by placing mylar and kapton foils 1 cm in front of the detectors. Table 8.2 lists the approximated thickness of the used degradation material. The radiation fields for the experiments were created using a wobbler magnet. The radiation fields were sized 2.5 times 2.5 cm^2 . The samples were irradiated in an evacuated volume. Thus no material had to be placed between the accelerator and the target which minimised the energy spread in the beam.

The detectors have been mounted in a PMMA plate in a pattern as shown in Figure 8.3. The EPR detectors were always irradiated in pairs of two, lithium formate on position I and III, alanine on position II and IV.

The fluorescent nuclear track detectors (FNTDs) were irradiated in or-

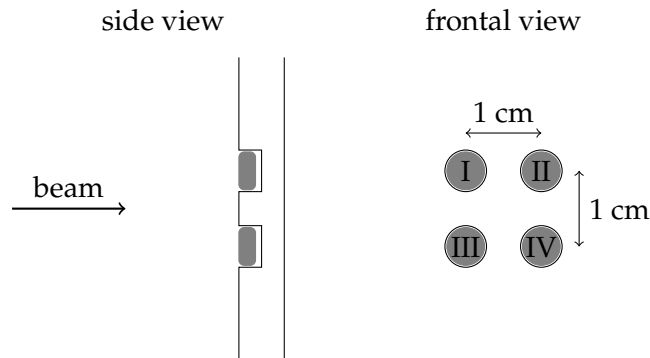


Figure 8.3: Drawing of the detector setup in frontal and side view.

thogonal and parallel orientation to the particle beam for iron, krypton and xenon ion beams, non-degraded and degraded, respectively. They were not employed for irradiation with nitrogen ions.

Irradiation programme

Detectors were irradiated using nitrogen, iron, krypton and xenon ion beams at an energy of 9.3 MeV/u. Additionally, for all ions but nitrogen irradiations with the beam energy degraded by insertion of thin foils 1 cm in front of the detectors were conducted.

The applied fluences had been planned to yield detector responses similar to the response towards 10 Gy ^{60}Co irradiation.

Additionally, a dose escalation study with 9.3 MeV/u xenon ions was conducted with a particle fluence up to $2.78 \cdot 10^9 \text{ cm}^{-2}$.

Fluence verification

Detectors were employed to estimate the penetration depth of the particles and to verify the fluence and field size. The field size was determined with Gafchromic films. The depth and fluence were measured employing FNTDs.

For fluence determination with FNTDs, detectors were irradiated with full detector front facing the particle beam. On readout the number of particle tracks in an area of known size was counted using the *Mosaic particle tracker* plugin [Sbalzarini and Koumoutsakos, 2005] for image evaluation software ImageJ¹. The number of particles divided by the counting area yields the fluence. Here a parallel beam with an angle of incident of 90° is assumed. The detectors were scanned in two orthogonal directions.

The size of the radiation field were verified with self developing GAFCHROMIC[®] HS radiochromic dosimetry films. The films have a 40 μm

¹<http://rsb.info.nih.gov/ij/>

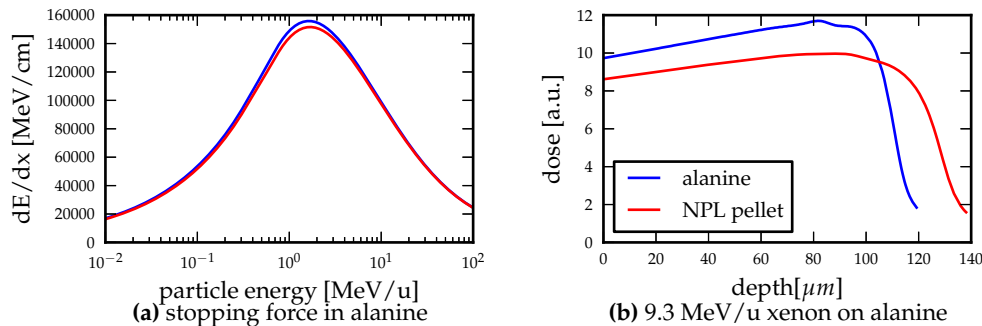


Figure 8.4: Comparison of the stopping force of xenon in pristine alanine and the NPL dosimeter material (Figure 8.4a) and its impact on the depth dose distribution of 9.3 MeV/u xenon (Figure 8.4b). Both calculations have been done for a density of 1.23 g/cm^3 .

thick active layer pack in two approximately $97 \mu m$ thick polystyrene layers. The film changes its colour from light blue to dark blue when irradiated. The best response is achieved when using the red channel in a scan by flatbed scanner [ISP Technologies inc., 1996].

Range calculations

For range calculations stopping force tables generated by the SRIM 2011 code [Ziegler et al., 2010] were used. SRIM data have been shown to be in good agreement with measured stopping force values in silicon for ions and energies used at RADEF [Javanainen et al., 2009]. Furthermore SRIM provides stopping force values for all used ions. As already mentioned in Chapter 2 the deviation in stopping force between isotopes is negligible.

In order to estimate the accuracy of the used stopping force values and thus the particle range estimates, range calculation were compared with the penetration depth measured with FNTDs.

The particle range was calculated following the CSDA. Stopping force tables were exported from SRIM. In order to use these data in own calculations, spline and material routines from the libdedx² [Lühr et al., 2011] program library were utilised. The output of the resulting code has been compared with original SRIM range values and Monte Carlo calculations using the Monte Carlo code Shield-HIT version 10a (Shield-HIT10a) [Dementyev and Sobolevsky, 1999, Hansen et al., 2012a, Hansen et al., 2012b].

The range calculations of the own code deviate by less than 0.1 % from the values provided by SRIM demonstrating that the tables were properly

²program code available under <http://sourceforge.net/apps/trac/libdedx/>

implemented.

Shield-HIT10a provides the opportunity to include generic stopping force tables for ions up to argon. Input tables holding SRIM stopping force values were generated. By using the same stopping force values, a comparison of a depth dose curve calculated with Shield-HIT10a with one calculated using the own CSDA implementation can give an estimate of deviations created by neglecting energy fluctuations and scattering in the CSDA. Nitrogen was used for the comparison since it has the largest penetration depth and thus would be expected to show the largest deviation between CSDA and Monte Carlo (MC) calculations.

Both calculations based on SRIM stopping powers showed no deviations. Based on this comparison all particle transport calculations for experiments with ions at energies below 10 MeV/u are in the following done with the own CSDA code.

As already observed by Palmans [Palmans, 2003] the composition of alanine dosimeters has an impact on the resulting stopping force. Figure 8.4a shows the stopping force of pure alanine (blue line) and the pellet mixture of the used pellets (red line), towards xenon ions, both with the same density. The stopping force of the pellet material was calculated using Bragg's rule. The main deviations are in the energy region below 10 MeV/u. While negligible in the track-segment regime this deviation has a high impact on the range of stopping particles as shown in Figure 8.4b.

Determination of the relative effectiveness

The RE is determined following Equation 3.9. Both detector signal and dose have to be corrected since only a sub volume of the detectors was irradiated. The relative effectiveness thus is the ratio of effective response equivalent dose RED_{eff} and the effective dose D_{eff}

$$\eta = \frac{RED_{\text{eff}}}{D_{\text{eff}}} \quad (8.1)$$

The average dose to the irradiated volume D_{eff} is

$$D_{\text{eff}} = \Phi \cdot \frac{E_{\text{kin}}}{R} \cdot \frac{1}{\rho} \quad (8.2)$$

where Φ denotes the particle fluence, E_{kin} the total kinetic energy of the particle, R the penetration depth of the particle and ρ the density of the detector.

To obtain the RED_{eff} , however, the effective detector signal has to be derived from the total detector signal of the whole dosimeter. The effective signal is the total signal multiplied by the ratio of the irradiated mass to the total mass, which for a cylinder equals the ratio of penetration depth R to the detector thickness T as shown in Figure 8.5a. However, the alanine detectors do not have the shape of a perfect cylinder. Their edges are slanted as

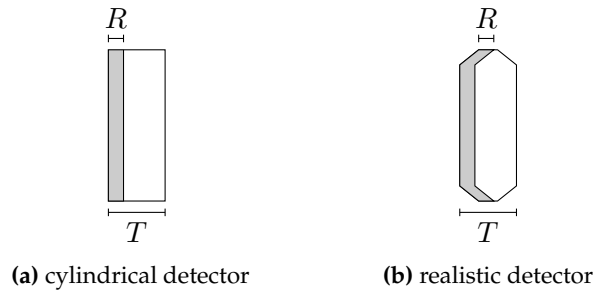


Figure 8.5: Illustration of the ratio of irradiated volume to total detector volume. R denotes the penetration depth and T the detector thickness. Figure 8.5a illustrates the case of a cylindrical detector, Figure 8.5b the case of a detector with slanted edges. The sketches are not to scale.

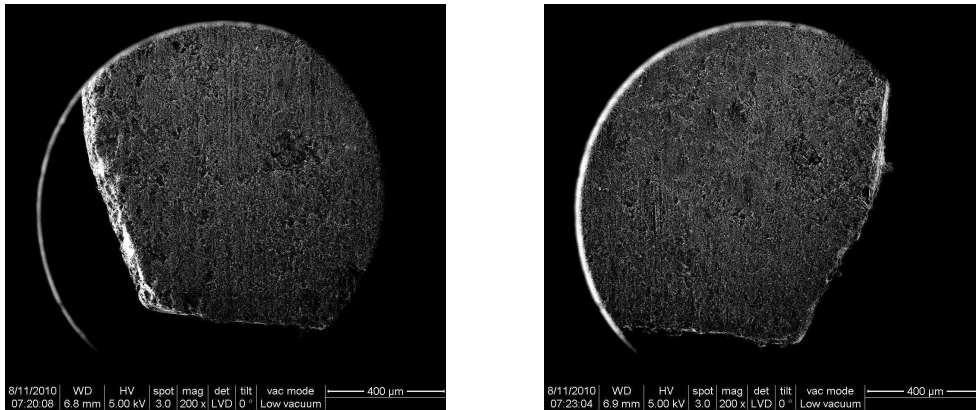


Figure 8.6: AFM-picture of the edges of one alanine pellet, showing the slanted edges as indicated in Figure 8.5b can be seen. Courtesy Jacques Chevallier, IFA, Aarhus University

shown in Figure 8.6. As illustrated in Figure 8.5b the R/T ratio is not equal to the mass ratio for such a geometry. The deviation from the ratio of irradiated mass to total detector mass deviates from the ratio of penetration depth to detector thickness by 4 %. The RED_{eff} of the alanine detectors have been corrected for this effect.

8.2 Results

Field homogeneity

The measurement response of detectors of the same kind irradiated in the same field vary up to 19 %. The spatial resolved fluence measurements with

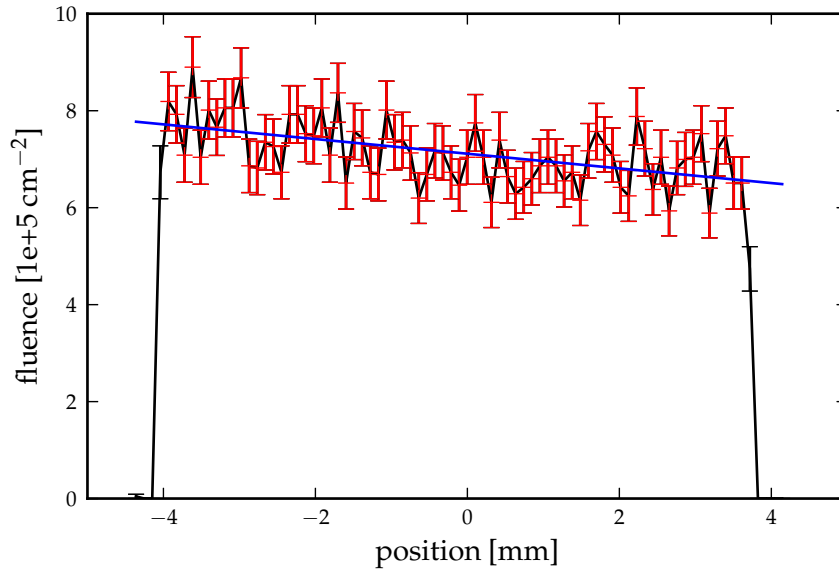


Figure 8.7: Example for the fluence distribution along the central axis of a FNTD irradiated with 9.3 MeV/u iron ions. The measured fluence is plotted as a function of the measurement position on a FNTD. The black line connects all measured fluence values, the data marked red are used for determination of the average fluence. The blue line represents a linear regression based on the red data points..

FNTDs show gradients up to $9.4 \text{ cm}^{-2} / \text{mm}$ over a distance of 2 mm and up to $2.4 \text{ cm}^{-2} / \text{mm}$ over a distance of 3.5 mm. An example of the fluence distribution measured on a FNTD irradiated with 9.3 MeV/u iron ions is shown in Figure 8.7.

Particle fluence

Fluence measurements with FNTDs and corresponding fluences provided by the accelerator logging system are listed in Table 8.3. The fluence value for 9.3 MeV/u xenon ions is the average of measurements with four FNTDs. The measurements for the other ions are based on the irradiation of one FNTD, respectively.

The measured values are generally below the nominal values. The average ratio between nominal fluence and measured fluence is 0.878 ± 0.051 . This value has been used to correct the nominal fluence in all following calculations.

ion	Φ_{nominal} [cm ⁻²]	Φ_{FNTD} [cm ⁻²]	deviation
Fe 5.8	$5.04 \cdot 10^5$	$4.04(0.42) \cdot 10^5$	-19.8 %
Fe 9.3	$7.45 \cdot 10^5$	$7.07(0.56) \cdot 10^5$	-5.1 %
Kr 9.3	$7.12 \cdot 10^5$	$6.49(0.54) \cdot 10^5$	-8.8 %
Xe 6.4	$5.16 \cdot 10^5$	$4.63(0.56) \cdot 10^5$	-10.3 %
Xe 9.3	$1.14 \cdot 10^6$	$9.94(1.27) \cdot 10^5$	-12.8 %

Table 8.3: Fluences measured for five different ion combinations. Φ_{nominal} denotes the fluence as given by the accelerator log system, Φ_{FNTD} the average particle fluence counted on FNTD. The value in brackets gives the sample standard deviation of the fluence values measured on the FNTD.

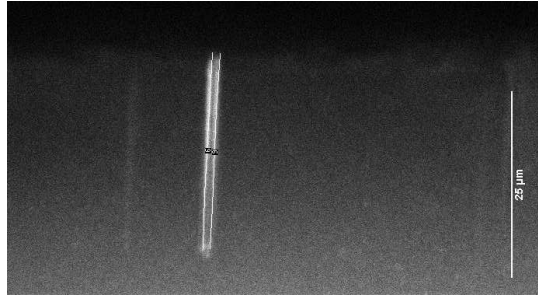


Figure 8.8: Picture of two 5 MeV/u krypton tracks in a FNTD. The particles are coming from the upper side of the picture and flying downwards.

Particle range

Non-degraded beams Range calculations with non-degraded particle beams in aluminium oxide deviate less than 4.5 % from the measured range. Values are listed in Table 8.4. Figure 8.8 shows a picture of a FNTD with two visible particle tracks.

The largest deviation between measured and calculated range is for xenon ions, while the deviations for iron and krypton are within the experimental uncertainties.

Degraded beams Table 8.2 lists the ion with the employed degrader material and the particle energy after passing the nominal thickness of the degrader material, $E_{\text{out,SRIM}}$, as calculated with the SRIM code, respectively. These energy values do not comprehend with particle ranges measured in FNTDs.

E_{range} denotes the particle energies deducted from the penetration depth measured in the FNTD. The CSDA range as a function of particle energy was

ion	energy [MeV/u]	R _{meas} [μm]	uncert [μm]	R _{calc} [μm]	dev [%]
⁵⁶ Fe	5.8	31.28	± 1.20	31.24	-0.13
⁵⁶ Fe	9.3	53.56	± 1.51	53.92	0.67
⁸² Kr	5.0	27.93	± 1.68	28.14	0.75
⁸² Kr	9.3	52.38	± 2.0	52.05	2.49
¹³¹ Xe	6.4	35.20	± 1.21	35.09	-0.31
¹³¹ Xe	9.3	54.82	± 1.69	49.47	-4.53

Table 8.4: Measured and calculated particle ranges in Al₂O₃, with $\text{dev} = \frac{R_{\text{calc}} - R_{\text{meas}}}{R_{\text{meas}}} \cdot 100$

calculated and compared with the particle range measured in the FNTDs. Figure 8.11 shows the deviation between the calculated ranges as a function of energy and the measured penetration depths for degraded iron, krypton and xenon ions in Al₂O₃. The E_{range} values are the energy values which correspond to the measured penetration depth. They are listed in Table 8.2 and used for all following calculations.

The setup with degrader of the nominal thickness has been simulated with FLUKA to estimate a possible fluence decrease introduced through scattering. The calculations showed that there were no changes in particle fluence due to out-scattering in the part of the target area where the detectors were placed.

Signal stability

Figure 8.9 shows the detector signal for alanine relative to the first measurement for a series of measurements conducted at different times after the irradiation. The first measurement has been conducted latest two days after irradiation. The particle energy has been 9.3 MeV/u for all displayed measurements. The dose values given in the legend denote the average dose in the irradiated volume. The data points for irradiations with iron and krypton ions and xenon ions at a dose of 998 Gy are the average over four dosimeters. The other values are the average of two dosimeter dosimeter irradiated in the same radiation field. The uncertainty of the measurements is 3% at one standard deviation.

Relative effectiveness

Table 8.5 lists the measured relative effectiveness of alanine for the applied ion/energy combinations, respectively. Table 8.6 lists the same for lithium formate detectors. Figure 8.10 shows the measured RE towards 9.3 MeV/u xenon ions as a function of dose for alanine and lithium formate.

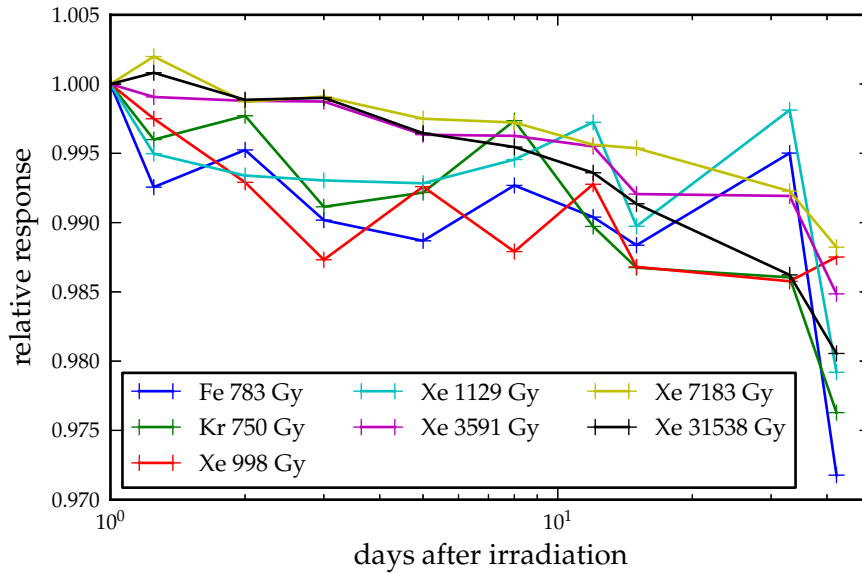


Figure 8.9: Detector response of alanine dosimeters relative to the first measurement as a function of time after irradiation. The uncertainties of 3% are not plotted.

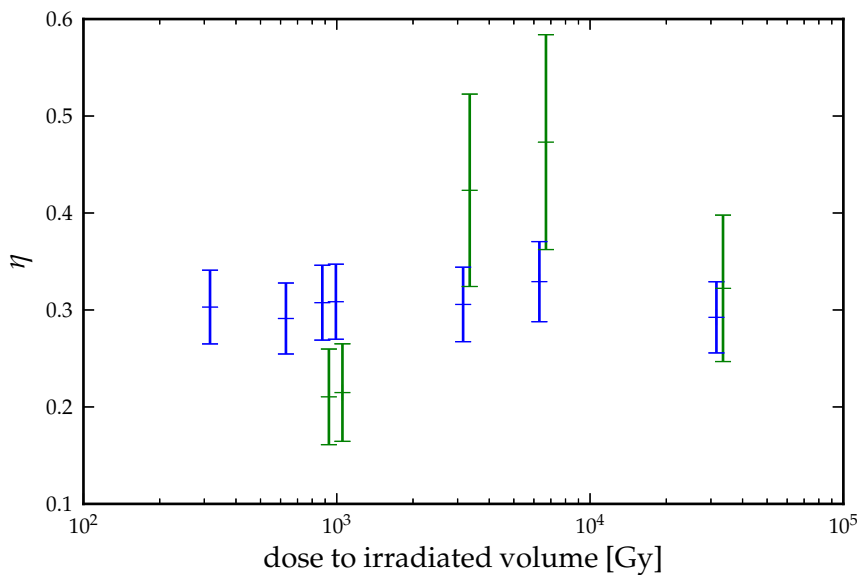


Figure 8.10: The relative effectiveness of alanine (blue) and lithium formate (green) towards stopping xenon with an initial energy of 9.3 MeV/u as a function of dose to the irradiated volume. Error bars indicate one standard deviation.

ion	energy [MeV/u]	η	σ_η
N	9.3	0.36	0.05
Fe	5.8	0.18	0.03
Fe	9.3	0.30	0.04
Kr	5.0	0.31	0.04
Kr	9.3	0.27	0.03
Xe	9.3	0.31	0.04

Table 8.5: Relative effectiveness of alanine. σ_η denotes one standard deviation.

ion	energy [MeV/u]	η	σ_η
N	9.3	0.66	0.15
Fe	5.8	0.62	0.15
Fe	9.3	0.31	0.08
Kr	5.0	0.66	0.16
Kr	9.3	0.41	0.10
Xe	6.4	0.39	0.10
Xe	9.3	0.33	0.08

Table 8.6: Relative effectiveness of lithium formate. σ_η denotes one standard deviation.

8.3 Discussion

Particle fluence and field homogeneity

Detectors irradiated with the same field should yield the same detector response within the uncertainties of the readout procedure. However, signals of detectors irradiated in the same field are different up to 19 %. This is observed regardless of detector type. However, the fluctuations for lithium formate detectors are higher than for alanine detectors. Additionally, some fluence measurements with FNTDs show fluence gradients over the detector as shown in Figure 8.7. The size of the variations varies, however, there is a tendency that the detectors placed in position I and II have a lower signal than the once placed in position III and IV. The FNTDs have always been placed in the centre of the radiation field, between the positions I to IV, however their alignment was not controlled. If gradients appear on a FNTD, they are always only in one dimension.

Since the gradients in the FNTD fluence measurements agree with the differences between detector measurements at different positions it is assumed that there is a linear gradient over the whole radiation field. For the calculation of the RE thus the average RED of two detectors was always used.

Under the assumptions that the radiation field had a linear fluence gradient in one direction and that the FNTDs have been placed in the centre of the radiation field, the average fluence measured with the FNTDs is estimated to be the average fluence of the whole radiation field.

The values measured with the FNTDs are below the nominal fluence given by the accelerator control system. The counting efficiency of the detectors is assumed to be 100 %. The average deviation of nine fluence measurements from the nominal fluence was used as correction factor to yield the actual fluence for all measurements.

Range calculations

The calculated range values agree better than 5 % with the values obtained with the FNTDs. However, this only proves that the stopping force values for Al_2O_3 provided by SRIM agree with these measurements. Al_2O_3 is a crystal, thus molecular bounding of electrons does not influence the stopping force. For alanine and lithium formate one would expect slightly higher deviations due to the electron configuration in the molecules, which is not considered in stopping force calculations based on Bragg's rule. This effect, however, can not be quantified here.

The on-side manufacturing of the degrader induced uncertainties in the degrader thickness and thus in the particle energy after the degrading foils. As described in the Section 8.2 the energy of the degraded beams has been estimated based on the penetration depth measured in the FNTDs. Figure 8.11 shows the deviation of a calculated penetration depth R_{calc} from the measured values as function of the corresponding energy. The actual particle energies were determined at the minimal deviation. The dashed lines indicate 5 % deviation between measured and calculated range.

An estimated uncertainty in the particle range calculations of 5 % results in an energy uncertainty of ≈ 6.5 % for degraded beams.

For here reported measurements with effective doses below 10 kGy the effective dose as well as the effective RED are linear dependent on the penetration depth. In the determination of the RE following Equation 8.1 the penetration depth is reduced from the fraction. As discussed before the linear RED dependence on range is not valid for the measurements at the highest dose of 32 kGy. The estimated range uncertainty of 5 % has an impact of below 0.5 % on the determination of the RE at this dose level.

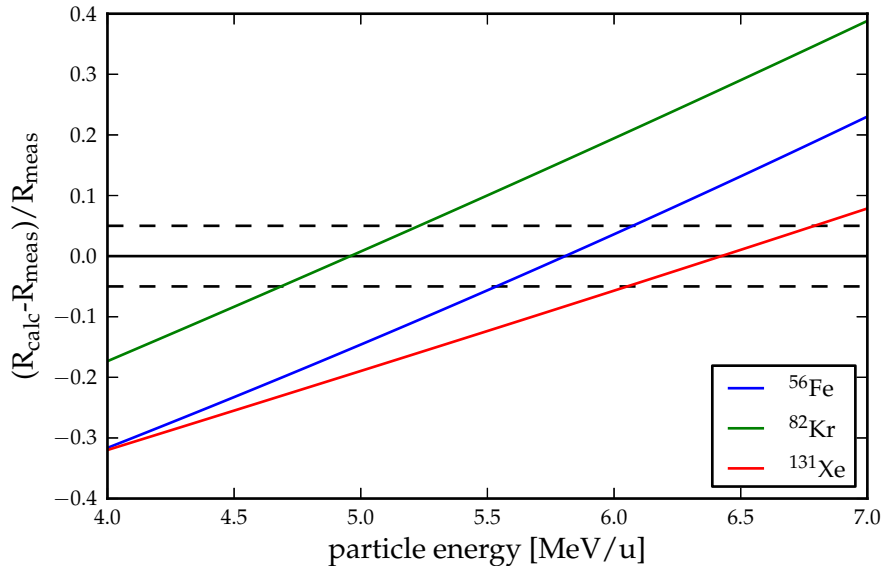


Figure 8.11: Deviation particle ranges calculated as a function of particle energy from measured values in degraded beams. The slashed lines indicate 5 % deviation.

Signal stability

For a time period from one to forty-two days after the irradiation the measured signal of alanine varies less than 2.8 % from the first measurement. While below the uncertainty of the measurement, there is a tendency to a fading of signal. This tendency, however, seems to be independent from particle type and applied dose. No significant difference between dosimeters irradiated with 998 Gy to 31538 Gy has been found.

The investigations on signal fading after carbon ion irradiation [Herrmann et al., 2011b] were done at relative high particle energies (80 -400 MeV/u) and thus do not provide any information on possible signal fading in the peak region of a depth dose distribution. However, findings in this experiment allow to conclude, that compared to photon irradiation no increased signal fading is to be expected in clinical settings, also not in the Bragg peak, regardless of dose or particle type.

Relative effectiveness

Table 8.7 lists the estimated uncertainties of the measured RE values. The high uncertainty on the lithium formate readout is due to a problem in the sample support system of the readout device. A part of it had to be replaced during the measurements. This changed the calibration of the device and

	alanine		lithium formate	
	degraded	9.3 MeV/u	degraded	9.3 MeV/u
particle energy	6.5 %	0.1 %	6.5 %	0.1 %
RED	3.0 %	3.0 %	20.0 %	20.0 %
fluence	12.2 %	12.2 %	12.2 %	12.2 %
combined	14.1 %	12.6 %	24.3 %	23.4 %

Table 8.7: Uncertainty budget for the determination of the RE. All values represent one standard deviation.

happened before the reference samples have been scanned. The EPR measurements of the lithium formate detectors are not finished yet. Therefore, the data set has to be considered as preliminary.

For the calculation of the RE of lithium formate towards 9.3 MeV/u xenon ions the measurements at the two lowest doses have been used. The RE is 0.21 ± 0.05 if only the irradiations with the two lowest doses are considered and 0.33 ± 0.08 if all xenon measurements are included.

Generally, the RE is expected to decrease with decreasing particle energy. However, the measured RE for the degraded krypton beam in alanine and for all degraded beams in lithium formate is higher than for the not degraded beams. This indicates that the dose to the pellet may have been underestimated. Reasons for this could be an overestimation of the energy absorption in the beam degrader. This however, would affect alanine and lithium formate measurements to the same amount and is thus unlikely, since not observed here. Variations in the particle fluence, with a higher fluence at the positions I and III, in addition to the inhomogeneities already discussed can also be ruled out, since such would affect the measurements at higher ion energies to the same amount. Additionally, such variations between the detector position were not seen in the case where alanine pellets were placed in all four positions. An increased signal fading for detectors irradiated with degraded beams, prior to the first measurement, can also be ruled out, since such would result in a decrease of the RE. It might thus be, that the inhomogeneities in radiation field have been more random than estimated or the precision of the lithium formate readout has been worse than estimated.

The measured RE value for 9.3 MeV/u nitrogen is above the values reported for higher energy nitrogen beams [Waldeland et al., 2010]. For this value the same considerations as in the previous paragraph apply. It would be expected to be lower.

Dose dependency of the relative effectiveness

Variations of the relative effectiveness for higher doses in alanine can not be seen. Possible effects of overlapping tracks are expected to be observed in lithium formate at lower doses than for alanine. Due to the high fluctuations in the measured values for the RE of lithium formate, no conclusions can be drawn out of these data.

9. Calculation of detector response

In this chapter the computer codes used in this thesis for calculation of the relative effectiveness are introduced.

9.1 Original Hansen and Olsen model

The original model by Hansen and Olsen [Hansen and Olsen, 1985] has been written in Cobol and is presented in detail in the dissertation of Johnny W. Hansen [Hansen, 1984]. Later on the code has been translated into Turbo Pascal. The concept of the model and its deviations from the original work of Butts and Katz are presented in Section 4.5.

For reference the model has now been reprogrammed in C. Thus the only changes done in this implementation is the reorganisation of the code and a transfer of the used parameters to the International System of Units (SI units).

Figure 9.1 shows a comparison of the reprogrammed code with results from the original code published in [Bassler et al., 2008]. The figure compares the RE as a function of the particle energy ($\eta(E)$) calculated for the six lightest ions. Solid lines represent calculations with the original code, dashed lines represent calculations with the re-implementation. The lines overlap over a wide energy range. They only deviate at particle energies below 0.1 MeV/u.

The code does not account for relativistic effects and thus works only for energies below ≈ 465 MeV/u. At this energy the non-relativistic calculated speed reaches the speed of light.

Note also that the calculated RE values for protons exceed unity which is in contradiction to the target theory for one-hit detectors.

Hansen and Olsen estimated the accuracy of their calculations to be within 10 % [Olsen and Hansen, 1985] and mainly accounted this to uncertainties in the stopping force.

9.2 New implementation

The reference implementation as described in the previous section has been used as basis for further development.

The original code had some numerical approximations to minimise calculation time and memory use. These approximations have been replaced by

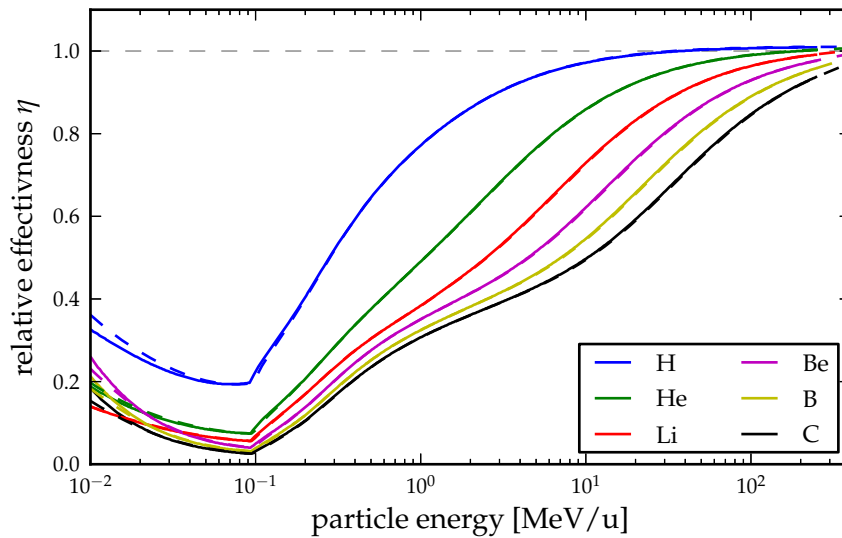


Figure 9.1: Comparison of the results of the RE calculations as a function of particle energy for infinitesimal thin alanine targets of the original code (solid lines) from Hansen [Hansen, 1984] and the re-implementation (dashed lines). The graph shows calculations for the lightest six ions.

exact expressions where the amount of saved resources did not justify the introduced uncertainties measured at the availability of computational power today. Numerical approximations have also been replaced where they hindered generalisation of the code, *e.g.*, for detectors which can not be described as one-hit detectors.

The calculation of the relative particle speed β is now done relativistic which allows to calculate the response for higher particle energies. The implementation of the RDD has been improved and the deviation between the integrated energy of a RDD and the stopping force eliminated. This discrepancy is in the original code the reason for the appearance of RE values above unity.

The original stopping force formulation has been replaced by the libdEdx library which allows to choose between different stopping force sources. Additionally, stopping force values generated by the SRIM 2011 [Ziegler et al., 2010] code have been implemented.

RDD formulations by other authors have been implemented. Those are the formulations suggested by [Waligorski et al., 1986] and [Katz et al., 1996] which describe physical dose distributions which have to be convoluted with the size of the target area according to Equation 4.16 to receive a effective dose distribution. Descriptions of the effective RDD by au-

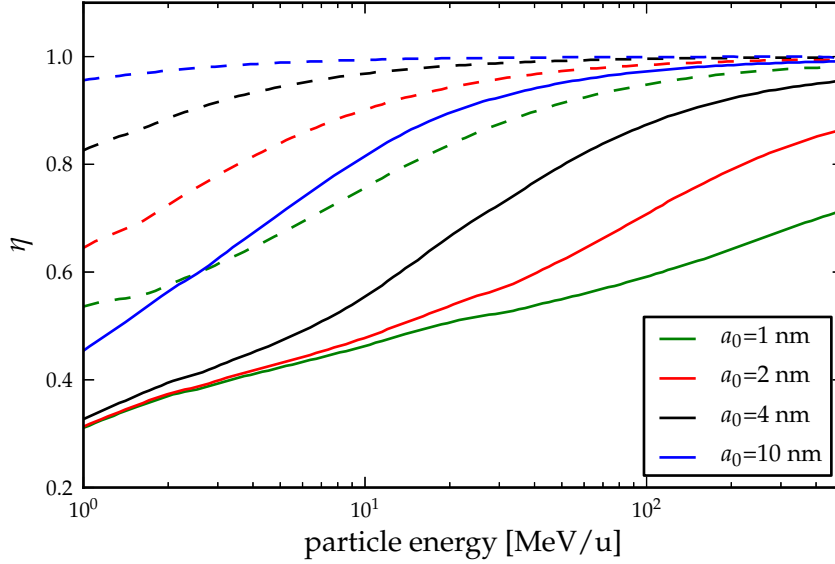


Figure 9.2: The RE of alanine towards carbon ions (solid lines) and protons (dashed lines) for different values of a_0 as a function of the particle energy. The correspondent RDDs for carbon ions are shown in Equation 9.3.

thors [Scholz and Kraft, 1996, Edmund et al., 2007, Elsässer et al., 2008] are also included.

At a fixed value for a_0 the RDD formulations for extended targets of Hansen, Waligórski, Katz and Edmund deviate in the maximum dose for a distance $r \leq a_0$ from the ion path and in the transition region $a_0 < r \lesssim 3 \cdot a_0$. The integral dose of the RDD models by Katz and Waligórski do not agree with tabulated stopping force values. The stopping force, however, does directly influence the RE (Equation 4.18). The RDDs are thus adjusted to the stopping force by adding the difference between the integrated RDD and the stopping force to the core region, as done by Hansen.

New formalisms for the calculation of the track width have been implemented [Tabata et al., 1972, Waligorski et al., 1986, Scholz and Kraft, 1996, Elsässer et al., 2008]. The formulae for the formalisms are listed in Appendix B.

Variations in the used a_0 values have a high impact on the RE as shown in Figure 9.2. This is caused by the variation of the maximum energy in the core for different values of a_0 which is demonstrated in Figure 9.3 for the improved Hansen formulation.

With a variation of the a_0 value the results of RE calculation with the stopping force adapted RDD formulations for [Waligorski et al., 1986], [Katz et al., 1996], [Edmund et al., 2007] and the adapted Hansen RDD can

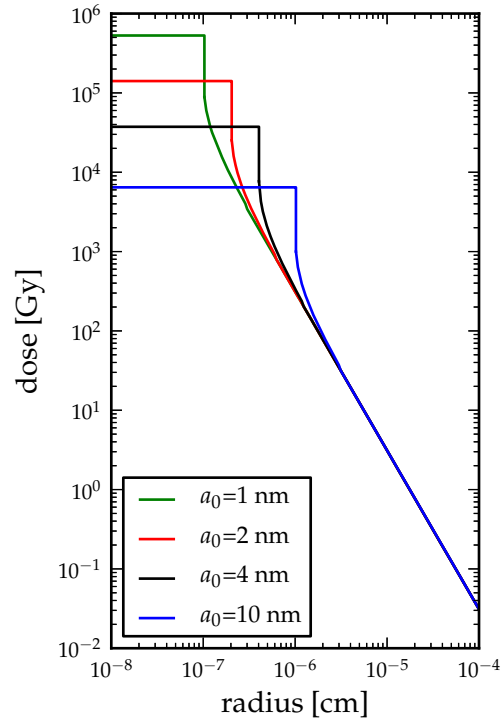


Figure 9.3: Radial dose distributions of 100 MeV/u carbon ions in alanine calculated for different values of a_0 . This RDDs have been calculated with the improved Hansen formula (Equation 4.25).

be assimilated. Therefore only the improved formulation by Hansen is used for the further presented calculations.

The a_0 value for the alanine RE calculations has been adapted for the composition and the characteristic dose of the NPL dosimeter. The optimal a_0 value has been found through a χ^2 goodness of fit test of the calculated RE towards measured carbon ion RE data [Herrmann et al., 2011b]. The best agreement was found for an a_0 value of 4.4 nm for the Hansen formulation, regardless of the electron range formulation.

Target theory (Equation 4.4) approximates a value of 3.1 nm for an average hit energy of 60 eV and 2.9 nm for an average hit energy of 51 eV.

9.3 Libamtrack

The libamtrack¹ open-source computational library is intended to provide a platform for amorphous track structure calculations. It provides three ATM algorithms, an implementation of the Katz ion/gamma-kill (IGK) model, a compound Poisson processes using successive convolution (CPP-SC) [Greulich et al., 2012a] and a generic grid summation (GSM) [Greulich et al., 2008] algorithm. Besides these main algorithms it also provides different models for the underlying calculations such as various RDDs and functions to determine the maximum electron range and thus the extension of these RDDs. Furthermore it provides pre-defined photon response characteristics such as generalised multi-target, multi-hit functions, functions describing radioluminescence and linear-quadratic dose-response. With a few exceptions these functions can be combined *ad libitum* [Greulich et al., 2010]. The RE determination in the libamtrack algorithms follows the iso-dose definition (Equation 3.10).

The author contributed to the libamtrack project by testing and debugging. Furthermore, he created the interface between the libamtrack code written in C and the Python programming language.

The IGK algorithm is a flavour of the TST model as described in [Waligorski, 1988], as such it does not take into account the overlapping of particle tracks. The gamma-kill concept does not play a role in the here presented calculations since it only applies for multi-hit detectors.

The CPP-SC algorithm is based on a probabilistic model [Grzanka et al., 2011, Greulich et al., 2012a]. It calculates the probability frequency $f(D)$ of a dose D in a point. $f(D)$ is the derivative of $F_n(D)$, the cumulative distribution function of the local dose for n particle tracks. For a single particle $F_1(D)$ is the ratio of the area covered with dose D to the total track area ($2\pi r_{\max}$),

$$F_1(D) = 1 - \left(\frac{r(D)}{r_{\max}} \right)^2 \quad (9.1)$$

here $r(D) = D^{-1}(r)$ denotes the inverse radial dose distribution. Given the dose probability frequency the detector signal for a traversing particle x can be calculated as

$$S_x(D) = \int_0^{D_{\max}} f(D) S_\gamma(D) dD \quad , \quad (9.2)$$

the probability weighted integral over the γ -response towards all local dose levels. The cumulative distribution function for a number of tracks larger than one is calculated using compound Poisson statistics, as the name of the algorithm indicates.

¹<http://libamtrack.dkfz.de>

In the case of a single traversing particle results of Equation 9.2 and Equation 4.9 are equal. This in mind deviations between the CPP-SC and the IGK algorithms should only occur in cases of overlapping tracks.

In a study [Herrmann et al., 2011a] the results of the IGK and the CPP-SC algorithms applied on alanine had been compared with literature data. The physics models for both algorithms were chosen equally. The electron range implementation based on [Waligorski et al., 1986] and a formulation of the RDD by [Edmund et al., 2007] were used.

The a_0 parameter was determined by comparison with experimental carbon ion data [Herrmann et al., 2011b] for each algorithm, respectively. The best agreement between the IGK algorithm and the data was achieved with an a_0 value of 2.0 nm and 3.4 nm for the CPP-SC algorithm.

Besides the deviation of the a_0 value, the results of the two algorithms also deviated for low particle energies and heavy ions which is not expected.

In the study a D_{37} value of 105 kGy as reported by Hansen was used. The study had been conducted with the libamtrack code revision number 453 (April 2010).

The libamtrack library is now (April 2012) at code revision number 1208. In this revision the CPP-SC and the IGK algorithm yield identical results for one-hit detectors at fluences at which overlapping tracks can be neglected if the calculations only differ in the algorithm.

After introduction of the D_{37} value for NPL dosimeter the a_0 values were adapted to 4.9 nm for the IGK and the CPP-SC algorithm to yield best agreement with the before mentioned carbon ion data. For the calculations presented in the following the CPP-SC algorithm was used since it should consider overlapping-track effects. However, it did not in the used version of libamtrack and thus the CPP-SC calculations are representing the case of a single ion crossing the detector.

9.4 Lithium formate

The lithium formate detector – being a one-hit detector– can easily be integrated in the above mentioned codes by feeding in the material parameter as D_{37} and stopping force and adapting the a_0 values.

The characteristic dose of lithium formate has been determined by Waldeland *et al.* [Waldeland et al., 2011] for peak-to-peak ($D_{37}=40.8$ kGy) and area ($D_{37}= 53.5$ kGy) evaluation. With this information the a_0 value can be obtained by fitting RE calculations to measurements.

Relative effectiveness values of lithium formate towards proton and nitrogen beams have been reported by Waldeland *et al.* [Waldeland et al., 2010]. The RED in this experiment was determined by integration over the EPR-spectrum. However, the RE of a detector should at low doses not be dependent of the dose evaluation method, as long as the same method is used for

the evaluation of the EPR-spectra of the reference radiation and the test radiation. For very high doses changes in EPR-spectra could create differences between the two methods. Since the data were taken at doses below 20 Gy these data can also be used to determine the a_0 value for RE calculations for predictions of measurements evaluated with the peak-to-peak assessment.

The RE was measured along a depth dose curve for 175 MeV protons and 550 MeV nitrogen ions and is reported as a function of the average LET in a detector.

The RE data, including the uncertainties, have been extracted from graphs in the publication. Figure 9.4 shows response calculations with the modified code described in Section 9.2 for different a_0 values together with the reported data. The reported values for the RE towards protons are below unity. Waldeland *et al.* could reproduce this values with a ATM by using a point target RDD and using the D_{37} value as a free parameter. They achieved best agreement for a D_{37} value of 18 ± 3 kGy. However, with the given experimental determined D_{37} values the proton RE values can not be reproduced by the here applied model, while agreeing with the RE values for nitrogen ions. Since in the experiments described in this thesis nitrogen ions and heavier ions are applied a bias towards the nitrogen data exists. Additionally, at the used proton energy a RE close to unity, similar to the RE of alanine would be expected, since the D_{37} of lithium formate is close to the one of alanine. The a_0 value is thus determined to yield the best agreement with the reported RE towards nitrogen ions, neglecting the proton data. Best agreement was found for a_0 value of 5 nm.

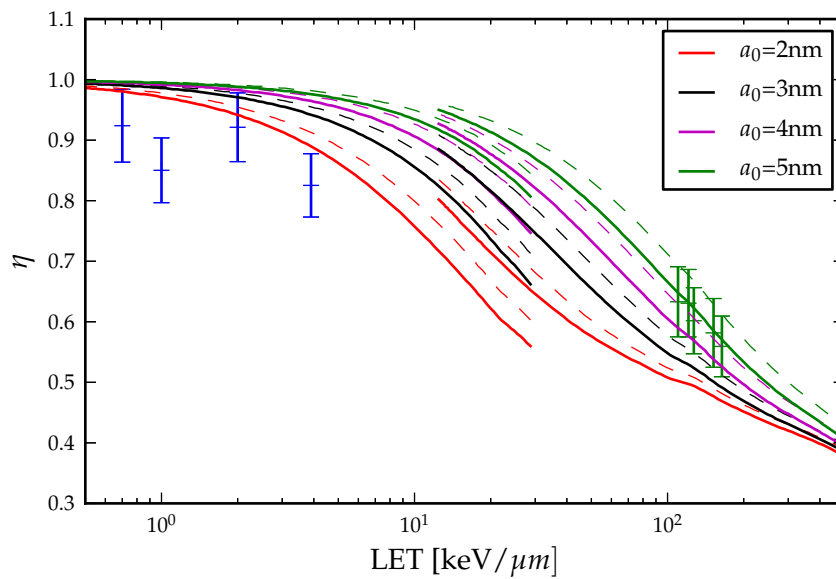


Figure 9.4: RE of lithium formate towards protons and nitrogen ions as a function of the average LET in the detector. The blue and green crosses represent data for proton and nitrogen ions, respectively, extracted from [Waldeland et al., 2010]. The solid line represent RE calculations with $D_{37}=40.8$ kGy for different values of a_0 . The dashed lines represent RE calculations for $D_{37}=53.5$ kGy

10. Comparison of model calculations with measurements

In this chapter the results of calculations with the three codes for RE calculations presented in Chapter 9 is compared with the measured data presented in Chapter 7 and Chapter 8. In the last section the calculations will be compared with data from literature.

10.1 Alanine - own data

Signal stability

Hansen's and Olsen's model predicts fading of up to four percent for 9.3 MeV/u xenon ions 41 days after irradiation. The predicted fading values for used ion/energy combinations applied in the here presented experiments for 41 days after irradiation are compiled in Table 10.1. All but the value for xenon are smaller than the uncertainty of the alanine signal measurements and thus can neither be confirmed nor rejected.

In general no increased signal fading for heavy ions compared to signal fading reported for γ -rays could be found in the here presented experiments. Thus signal fading is not regarded as a special issue in the following considerations.

ion	initial energy [MeV/u]	signal fading [%]
N	9.3	3.0
Fe	5.8	2.9
Fe	9.3	2.8
Kr	5.0	2.6
Kr	9.3	2.3
Xe	9.3	4.0

Table 10.1: Percentage signal fading in alanine predicted with the model of Hansen and Olsen [Hansen and Olsen, 1989] for 41 days after irradiation

Crossing regime

Figure 10.1 compares the measured data for protons (blue) and carbon ions (black) with results of calculations with the codes presented in Chapter 9. The black and the blue line represent calculations with the modified code for carbon ions and protons, respectively. The red lines represent calculations with the original model by Hansen and Olsen. The calculations for the green lines were conducted with the CPP-SC algorithm in libamtrack.

The results of calculations with the libamtrack algorithm and the modified code are close at energies above 10 MeV/u. They start to deviate significantly for energies below 10 MeV/u downwards, both for carbon ions and protons. The agreement with the measured carbon ion data for both is enforced, since the a_0 value has been chosen to fit these data. Libamtrack calculates the relative effectiveness following the iso-dose definition. Close to a RE of unity two very similar numbers are divided by each other, which may introduce rounding errors. The zigzag in the libamtrack calculations for protons close to a RE of unity are contributed to this numerical artefact.

The calculations with the original code from Hansen and Olsen deviate both for protons and for carbon ions from the latter two codes two. For protons a lower RE for energies below 10 MeV is predicted. The RE reaches values above unity for protons with energies above ≈ 30 MeV as previously discussed. Calculations with the reference code for carbon ions are below the corresponding values by the other codes below an particle energy of 200 MeV/u. They agree with all carbon ion measurements but the two with the lowest particle energy, within the experimental uncertainties.

Stopping regime

The relative effectiveness (RE) values of the experiment described in Chapter 8 are plotted in Figure 10.2 together with response prediction calculated with the three discussed models. The calculated RE values for all three codes are close to each other. Data values for irradiations with non-degraded beams at 9.3 MeV/u agree with the calculations of the original and the modified model within one standard uncertainty for all but xenon. For 9.3 MeV/u xenon ions the original models deviates by 15 %, the CPP-SC calculations by 16 % and the modified Hansen model by 19 %, whereas one standard deviation equals 13 %. However, all three models are within two standard uncertainties. Neither model agrees with the values found for 5.8 MeV/u iron or 5.0 MeV/u krypton ion beams, with the latter one already discussed in Section 8.3.

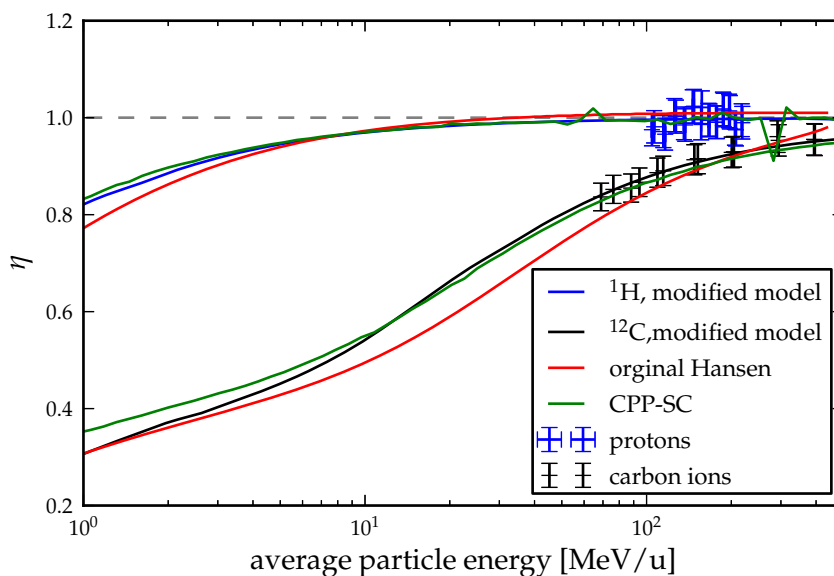


Figure 10.1: Comparison of measured relative effectiveness for protons (blue data points) and carbon ions [Herrmann et al., 2011b] (black data points) as a function of the average particle energy with model calculations. The blue and black lines represent calculations with the modified model for protons and carbon ions, respectively. The red lines originate from calculations with the original model and the green lines from calculations with the libamtrack CPP-SC algorithm. Error bars on measured data indicate one standard deviation.

10.2 Lithium formate

Figure 10.3 compares the measured relative effectiveness for stopping ions in lithium formate with calculations done with the modified model. The model calculations are based on the a_0 value found in Section 9.4. As already discussed in Section 8.3 the RE values for degraded ion beams are unexpected high. They do not match with calculated values.

The measured values for 9.3 MeV/u iron and xenon ions agree within their uncertainties with the model predictions. However, the measurements for nitrogen and krypton ions do not. As mentioned in Section 8.3 from comparison with the values reported by Waldeland *et al.* [Waldeland et al., 2010] the value for nitrogen ions would be expected to be lower.

Increasing the a_0 value elevates the RE. However, the total agreement between measurements and calculations is not improved, if the degraded energies are ignored.

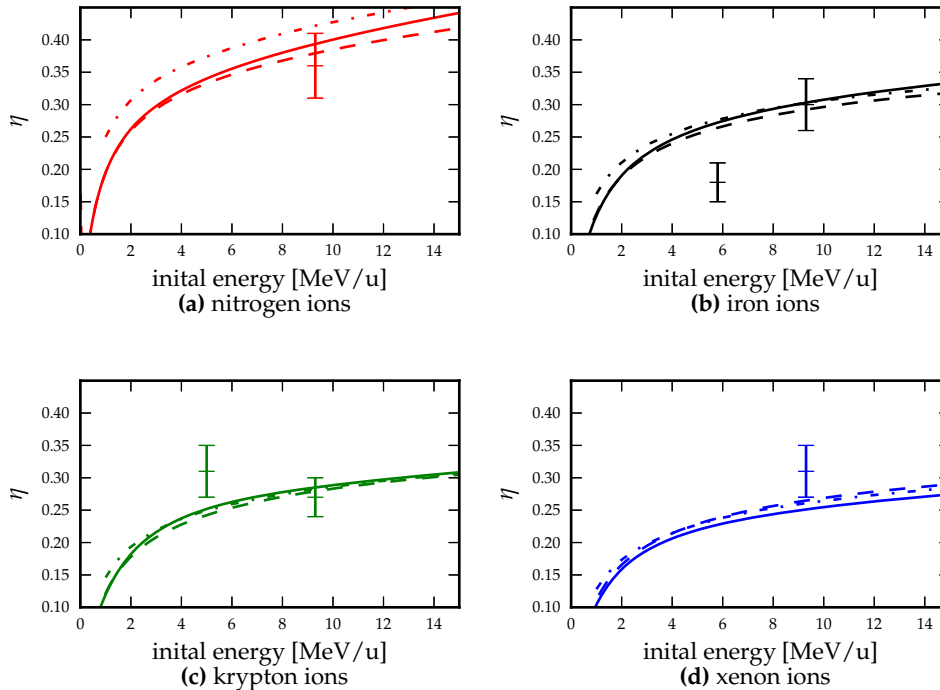


Figure 10.2: Comparison of the resulting RE (η) for alanine of the stopping ion measurements as a function of the initial particle energy with model calculations. Solid lines represent calculations with the modified model, the dashed lines calculations with the original model and the dash-dotted lines calculations with the libamtrack CPP-SC algorithm. Error bars indicate one standard deviation.

10.3 Alanine response data from literature

A comparison of the model calculations with literature data is difficult, since neither the alanine species nor the dose characteristics of the used detectors are known for all used alanine detectors. As listed in Table 5.1 the characteristic dose and thus the response behaviour of the detectors varies significantly. Especially for protons the available data consist of measurements with protons stopping in the detector and measurements where the protons cross the detector with a significant energy loss in the detector. For comparison of measurements with different detector thickness a representation of the RE depending on a single parameter would be desirable.

For particle energies at which the energy loss in a detector is significant ($> \approx 5\%$) the detector thickness has an influence on the RE. Figure 10.4a and Figure 10.4b show the relative effectiveness of alanine for protons and carbon ions as a function of the initial particle energy for five different detector set-

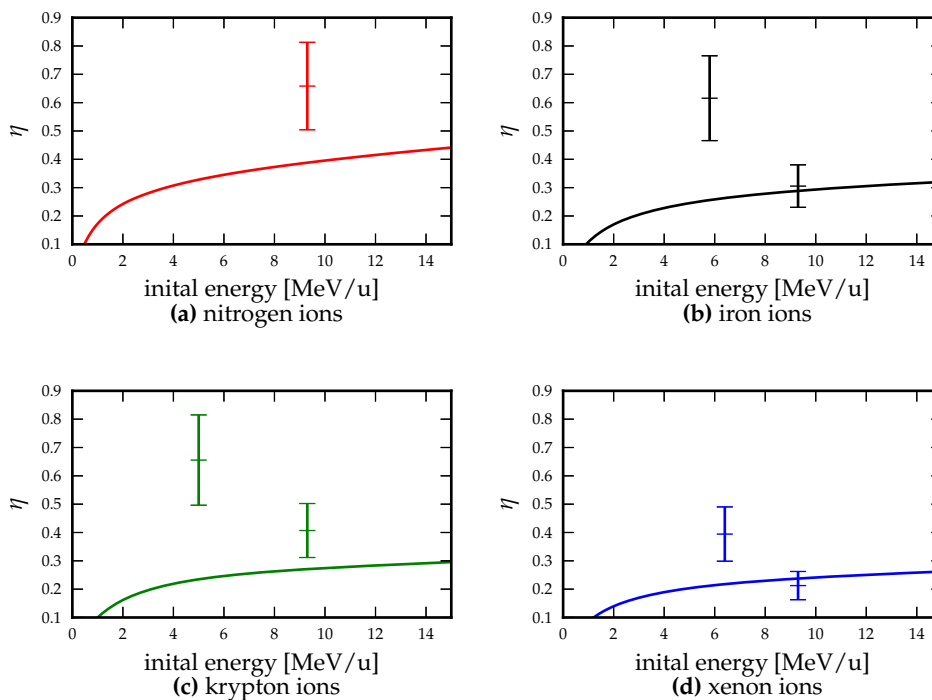


Figure 10.3: Comparison of the RE measured for stopping ions in lithium formate as a function of the initial particle energy with model calculations. Lines indicate calculations with them modified response model. Error bars indicate one standard deviation. Note, that for 9.3 MeV/u xenon ions the average RE of the two measurements with the lowest doses is plotted.

color	detector thickness
red	$\rightarrow \infty$
black	$\rightarrow 0$
blue	1 mm
magenta	2 mm
green	3 mm

Table 10.2: Color code for Figure 10.4

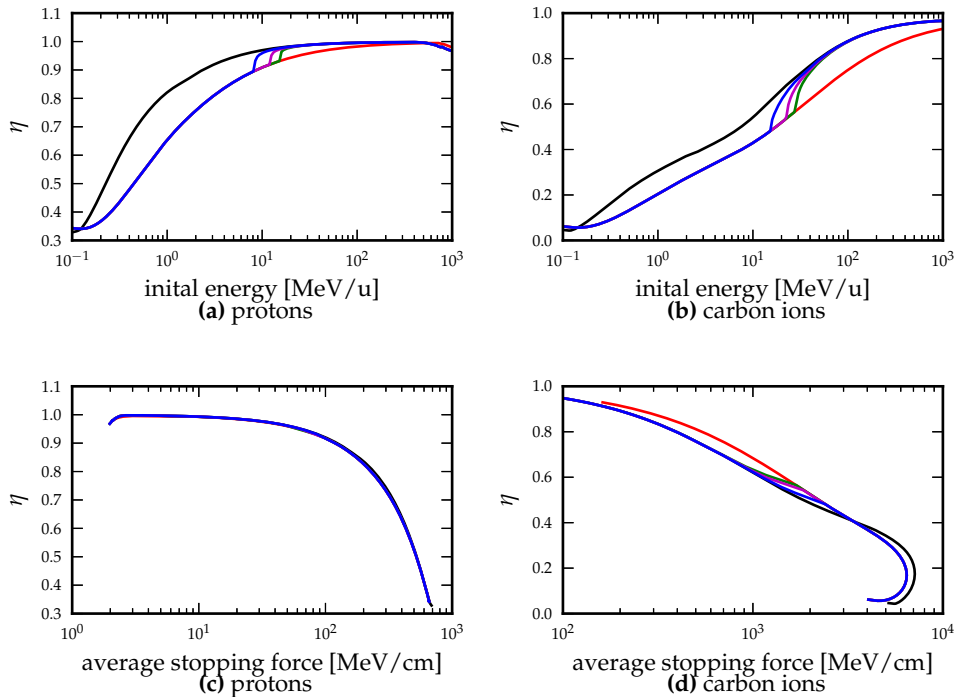


Figure 10.4: RE of alanine towards protons and carbon ions for different detector thicknesses, as a function of the initial particle energy (Figure 10.4a & Figure 10.4b) and the average LET (Figure 10.4c & Figure 10.4d). The red lines represent infinitesimal thick, the black lines represent infinitesimal thin detectors. The color code is given in Table 10.2.

tings. Extreme cases are when the detector thickness can be neglected (black line) and when all particle energies stop in the detector (red line). These two curves build the boundaries in which the RE curves for all detector thickness values lie. For illustration the curves for three different detectors of thickness 1 mm, 2 mm and 3 mm are plotted (For the color code see Table 10.2).

Palmans [Palmans, 2003] suggested to report RE values as function of an effective energy as a solution for this problem. He defined the effective energy as the particle energy corresponding to the average LET in the detector, or in the case of a fully stopping particle the average LET in the irradiated volume. This equals *de facto* the report of the RE as function of the average LET in the detector. In Figure 10.4c and Figure 10.4d the RE of protons and carbon ions, respectively, is plotted as a function of the average LET in the irradiated detector volume for the same five detector sizes as mentioned previously. While for carbon ions the RE is still dependent on the thickness of the detector, for protons the curves overlap. They are not identical, however,

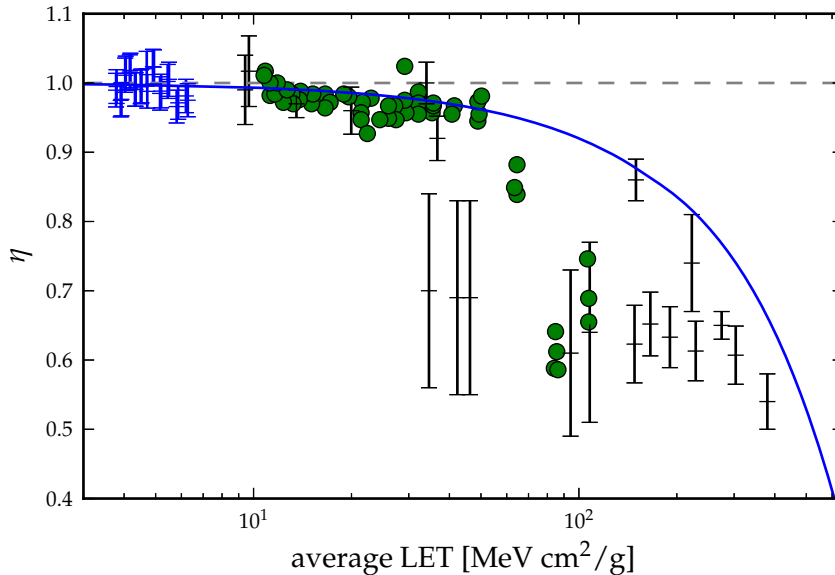


Figure 10.5: Comparison of literature data for the RE of alanine towards protons as a function of the average LET with calculations done with the modified model (blue line). The black crosses represent the data already shown in Figure 5.8, the green dots show data extracted from [Palmans et al., 2007]. The blue data points represent the data presented in Chapter 7

very close to each other.

While for heavier ions the detector thickness has an influence on the RE and has thus to be considered in comparisons between different experiments, for protons the detector thickness can be neglected if the RE is reported as function of the average LET in the irradiated volume.

Figure 10.5 shows a comparison of literature data of the RE of alanine towards protons as function of the average LET with calculations done with the modified model. The average LET has been calculated with the information on detector density and thickness given in the publications, respectively. The black crosses represent the data already shown in Figure 5.8. Additionally data extracted from a graph ¹ in a report by Palmans *et al.* [Palmans et al., 2007] is shown as green dots in the figure. The graph from which these data are extracted shows the RE as function of the LET weighted effective energy. The data are marked as preliminary in the publication, thus no uncertainties are given, introduced inaccuracy by the graphical extraction are below the size of the representing symbols in the graph. The data discussed in Chapter 7 is drawn as blue crosses.

¹Data have been extracted with the g3data software <http://www.frantz.fi/software/g3data.php>

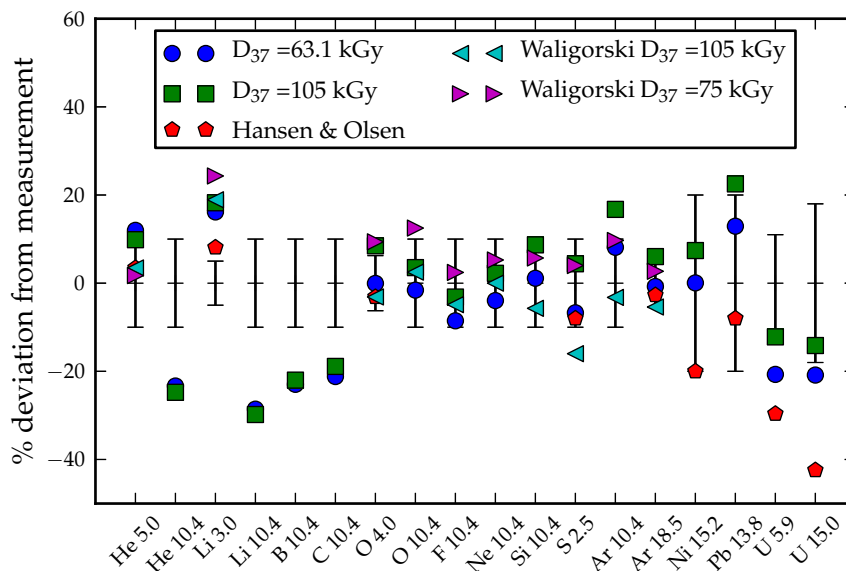


Figure 10.6: Deviation of model calculations from reported data. The abscissa names the ion and the initial energy in MeV/u . Values are listed in Table A.6. Where no uncertainty was given a uncertainty of 10 % has been assumed.

The depiction of the RE of protons as a function of the average LET removes the influence of detector thickness, compared to Figure 5.8. However, as seen in Figure 10.5 the scatter in the data available in literature can not be explained with the influence of the thickness of the detectors.

Reported RE values for ions heavier than protons and the corresponding calculated values are listed in Table A.6. Figure 10.6 compares the deviations between measured values and model calculations for the experimental data with model calculations reported in literature.

RE values are calculated for a characteristic dose of 63.1 kGy and for 105 kGy to account for the influence of different detector characteristics. The error bars indicate the reported experimental uncertainties. The deviation drawn at ordinate is calculated as

$$\%dev = \frac{\eta_{calc}}{\eta_{meas}} - 1.$$

The abscissa names the ion and the initial energy in MeV/u . The calculations are done for particles stopping in the detector. For the values for 10.4 MeV/u helium, lithium, boron and carbon ions reported by [Henriksen, 1966] it can be assumed, that the particle did not fully stop in the detector, see discussion of this values in [Waligorski et al., 1989].

11. Discussion

11.1 Comparison of the modified with the original model

The model by Hansen and Olsen was developed for an energy range in which relativistic effects could be neglected. It is thus surprising how well the results of the model agree with measured data at high energies. As shown in [Herrmann et al., 2011b] for carbon ions with energies from 100 -400 MeV/u the model agreed better than 4 %.

The change in the integration procedures solved the problem of the RE exceeding unity. The original code did not account for increased dose of the extended target dose distribution over the point target distribution in the region $a_0 < r < 3 \cdot a_0$.

Figure 11.1a shows the ratio between the non relativistic calculated and the relativistic calculated relative speed (β_{nr}/β_r). The relative particle speed affects the model calculations in determination of the dose to a point target and thus also the dose to an extended target (see Equation 4.15). This effect is mediated through addition of the energy difference between the RDD and the stopping force to the core region. More important is that the maximum electron range in the model is proportional to $\left(\frac{\beta^2}{1-\beta^2}\right)^{1.676}$. As β_{nr} approaches unity for a particle energy of approximately 465 MeV/u the function and also the maximum electron range diverges. However, as seen in Figure 11.1b the calculated RE for carbon ions deviates by less than four percent and for protons less than one percent when only the calculation of β is changed in the code. This shows how insensitive the RE calculations towards the track width in the energy regime above approximately 10 MeV/u are.

11.2 Comparison of model calculations with experimental data

Relative effectiveness of high energy protons

The measured RE values for protons in the energy range from 110 to 220 MeV agree well with calculations by all investigated models. As mentioned in Section 7.3 the aim of measuring the transition from a RE of unity to lower values was not reached.

The determination of the RE in the transition energy range would be crucial to judge over the RDD formulations. With a variation of the a_0 value

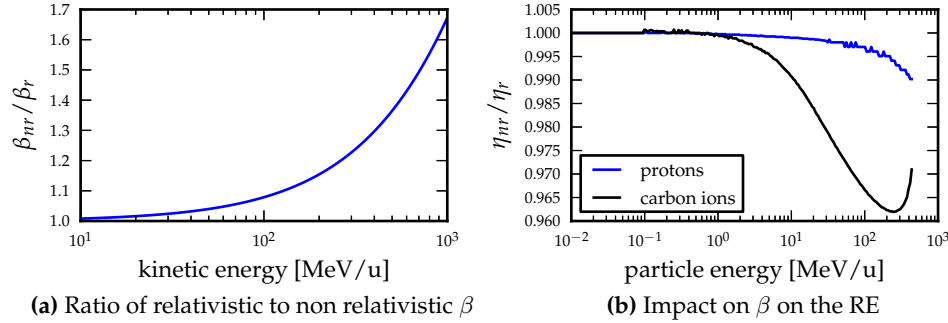


Figure 11.1: Figure 11.1a shows the the ratio of relativistic to non relativistic β as function of the kinetic energy. Figure 11.1 shows the ratio of the RE calculated with the original code by Hansen and a code which only deviates in the calculation of β . The deviations are shown for protons and for carbon ions.

the effective RDD formulations with an elevated dose in the track centre, as the formulations base on the original Katz approach, can be brought in agreement with the existing carbon ion RE data set. This is due to the fact that they mainly deviate in the value of the dose in the track centre for a given a_0 value when applied on extended targets. These changes in the a_0 values, however, also change the results of RE calculations for other ions. A benchmark of the RDD formulations could be conducted by comparison of model calculations with data sets of two ions species in the transition energy range. The energy range of the described experiments unfortunately does not extend to energies low enough to observe this effects.

The data set mentioned in [Palmans et al., 2007] and included in Figure 10.5 would be very valuable since it has been taken with NPL alanine detectors and thus could be directly compared with the existing RE measurements for carbon ions. Additionally, the data seems to cover the transition region and to lie between the RE values reported by [Olsen and Hansen, 1990] and the values by [Fattibene et al., 2002]. However, this are just speculations since the data set is not yet published. The data extracted and plotted in Figure 10.5 were not been used for comparison with calculations since they are plotted as a function of the effective energy correspondent to the average LET in the publication. Palmans mentions in [Palmans et al., 2007] that these values have high uncertainties due to mixed energy spectrum in which the pellets have been irradiated.

Generally, as seen in Figure 10.5 the here presented model seems to overestimate the RE of low energy protons. A quantitative statement is not possible, though.

However, previously measured proton depth dose curves in ala-

nine had been normalised in the entrance region to diode measurements [Nichiporov et al., 1995] or have been scaled to yield best agreement with ionisation chamber measurements [Gall et al., 1996]. According to the here presented measurements the absolute dose to alanine in entrance region of proton beams with energies above 120 MeV can be measured without corrections.

Relative effectiveness of heavy stopping particles

The data set resulting from the experiment described in Chapter 8 is ambiguous. The uncertainties are immensely increased due to the unknown field homogeneity and the deviation between reported and measured fluence. Additionally, the reason for the increased RE for degraded energies in the lithium formate detector is not known.

However, for alanine dosimeter the measured relative effectiveness for three 9.3 MeV/u ions agrees with predicted values within one standard uncertainty. The found value for xenon ions agrees within 2 standard deviations.

An exchange of the formalism describing the maximal extension of the track did change the agreement with the measured only slightly. The formulae listed in Appendix B.1 have been tested. The quality of agreement was judged by a χ^2 analysis. The best agreement was found with the formalism by Hansen [Hansen, 1984]. The RE values found with the formulae by Waligórski *et al.* [Waligorski et al., 1986], Tabata *et al.* [Tabata et al., 1972], Scholzet *al.* [Scholz and Kraft, 1996] and Elsässer *et al.* [Elsässer et al., 2008] deviated slightly more.

Track width calculations for 9.3 MeV/u particles in water with the Hansen formula yield 8.5 μm , 2.2 μm with the Scholz formula, 2.7 μm with the Elsässer approach and 42 μm with the Tabata formulation. A simulation of a 9.3 MeV/u particle with TRAX yields a track width of 2.5 μm . A variation of the Hansen width by factors 0.2, 0.5, 2.0 or 5.0 resulted in a worse agreement with the measured data.

However, the deviations in the calculated relative effectiveness for the different formulae are small compared to the uncertainties of the measurements, therefore, no judgement on the quality of the track extension models can be passed based on these data.

Calculations for lithium formate only partially match the measured values. Given the lower characteristic dose of lithium formate a lower RE compared to alanine is expected. However, the measured values are above the values measured for alanine. The deviations of the degraded beams have been discussed in Section 8.3.

The final measurements of the detector response in lithium formate have not been received at the moment of writing this thesis. There is some confidence that the final results may solve some of the open questions on the

lithium formate response variations. However, the 12 % uncertainty due to the fluence determination will still remain.

The relative effectiveness at high fluence level

The dependence of the saturation response of alanine as reported by Hansen and Olsen [Hansen et al., 1987] is in contrast to the assumptions of target theory and also has an impact on the validity of TST calculations. As shown in Equation 4.21 and Equation 4.23 the calculation of the relative effectiveness following Equation 4.18 is only valid, if the ratio of saturation responses is unity. Olsen and Hansen [Olsen and Hansen, 1985] suggested the dose rate might be the reason for the found differences, whereas Rotblat and Simmons [Rotblat and Simmons, 1963] predicted those differences for different characteristic doses. However, following their formulation in Equation 5.5 the maximum response ratio would be equal to the ratio of characteristic doses of different radiation types.

With the obtained data on the RE of alanine towards xenon an estimate of the maximum deviation between the saturation response of alanine towards ^{60}Co γ -rays and the saturation dose towards 9.3 MeV/u xenon can be done. Figure 11.2 shows the relative effectiveness as function of dose for four different maximum response ratios. Dotted lines represent the corresponding dose response curves. The RE curves have been calculated based on the measured average value for 9.3 MeV/u xenon ions and Equation 4.23. Note, that a lower $S_0^\gamma/S_0^{\text{ion}}$ ratio implies also a lower value of D_{37}^{ion} for the same RE value.

The knowledge of the saturation dose level is of importance for measurements of effects of overlapping tracks. At sufficiently high particle fluences the range of secondary electrons overlap. An overlap of tracks increases the local dose in the overlapping area, which leads to a decrease in the relative effectiveness if the higher dose exceeds the dose range, where linear dose response can be assumed. If the saturation response level of alanine would depend on radiation quality it would have to be taken into account for measurements.

A rough estimation for the onset of effects of overlapping tracks can be done by the following geometrical considerations. Figure 11.3 illustrates the discussion.

Given a parallel, mono-energetic particle field with fluence Φ , the average amount of particles crossing a cylindrical shell with an inner radius r and an outer radius $r + \Delta r$ around a particle track is given as the shell area times the fluence

$$\mathfrak{N} = \Phi \cdot \pi \cdot ((\Delta r)^2 + 2r\Delta r) \quad (11.1)$$

where \mathfrak{N} denotes the number of tracks crossing. To simplicity all tracks are considered to be a distance $R_{\text{eff}} = r + \frac{\Delta r}{2}$ from the central track. If they are placed equidistant from each other the angle between two tracks ϕ is given

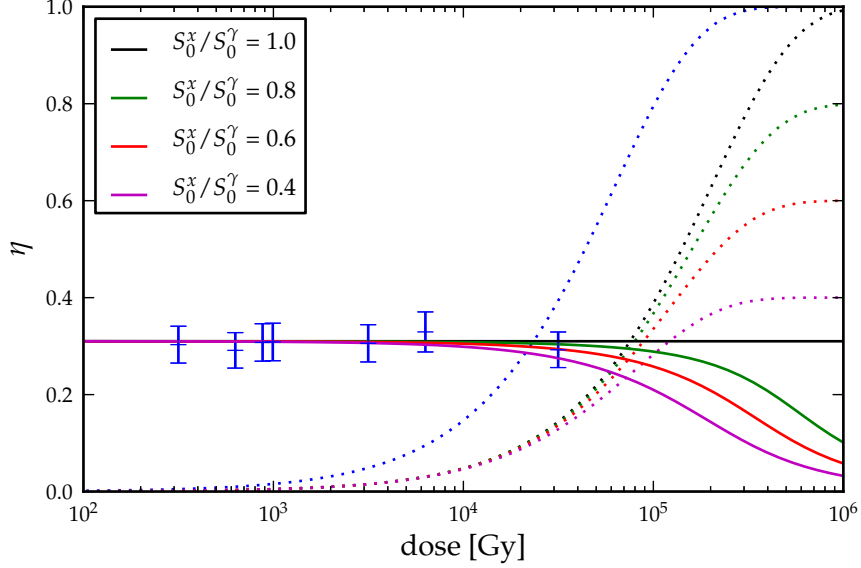


Figure 11.2: Influence on the saturation signal of 9.3 MeV/u xenon on the RE. The solid lines represent the RE for different ratios of the saturation signal of xenon to the saturation signal of ^{60}Co , respectively. The dotted lines represent the dose response curves, respectively. Track overlap effects are not included in these calculations.

as

$$\phi = i \cdot \frac{2\pi}{\mathfrak{N}}, \quad i \in [0, \dots, \mathfrak{N}] \quad (11.2)$$

The distance T from the tracks in this shell to the point x_0 is given as

$$T = \sqrt{R_{\text{eff}}^2 - x_0 R_{\text{eff}} \cos \phi + x_0^2} \quad (11.3)$$

Given a radial dose distribution $D(t)$ the dose contribution to the dose in point x_0 from the tracks in the interval $[r; r + dr]$ can be estimated as

$$D_{+,r}(x_0) = \sum_{i=0}^{\mathfrak{N}} D(T(x_0, 2\pi/i)) \quad , \quad (11.4)$$

where $D_r^+(x_0)$ denotes the dose added to point x_0 by the tracks in the shell at radius r . Integration over all distances ($x_0 < r_{\text{max}}$) and all shell radii ($r < x_0 + r_{\text{max}}$) would eventually yield a radial dose distribution around on particle track which would include overlapping tracks. r_{max} represents the maximal track extension. However, for higher particle energies the track *area* ($r_{\text{max}}^2 \pi$) increases and thus the amount of particles contributing to the dose in one point. The calculation time would increase rapidly.

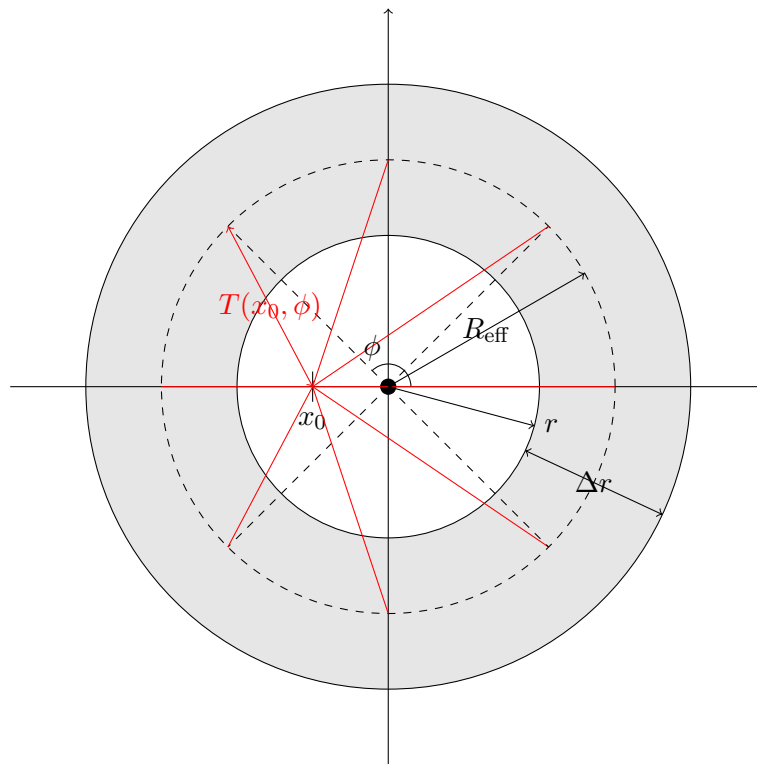
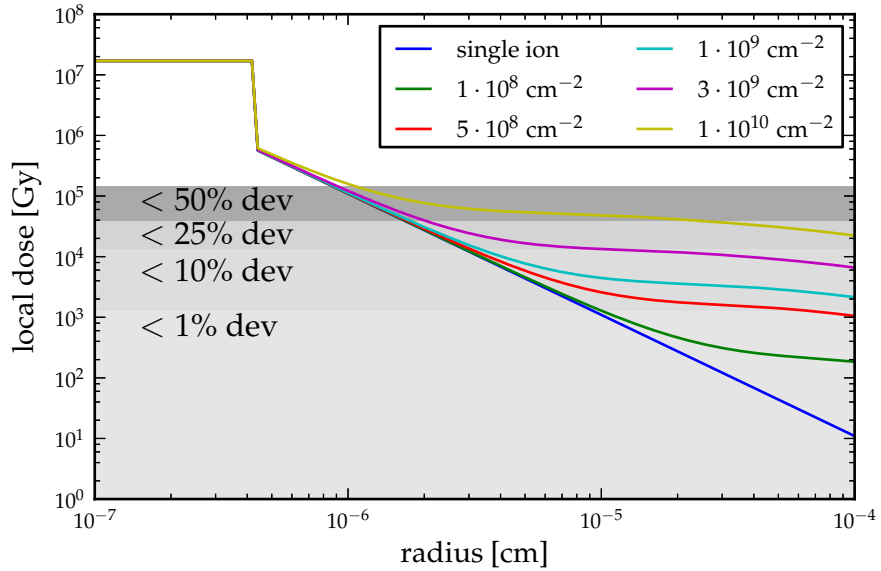


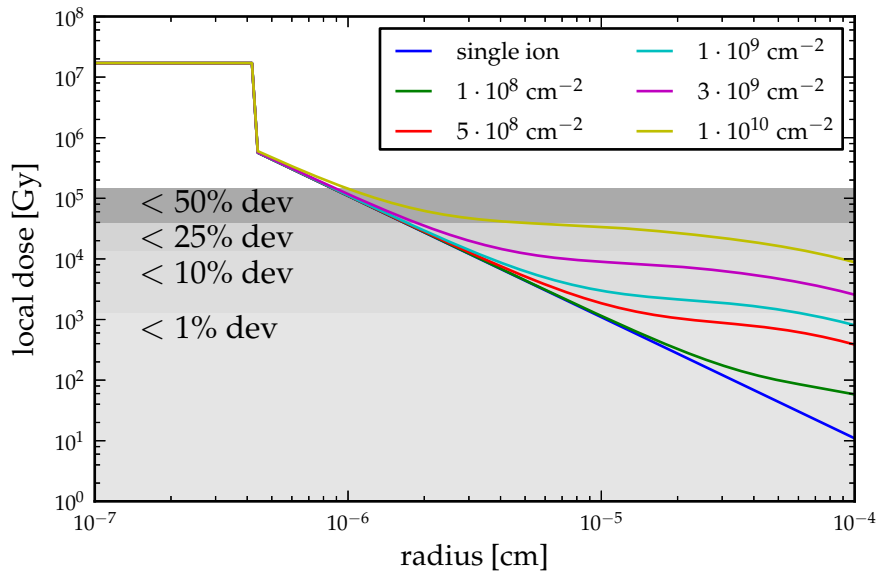
Figure 11.3: This figure aids the discussion of the track overlap effect estimation. In this case eight tracks are crossing the grey area and are equidistant placed at distance R_{eff} from the central track.

In the here discussed case of a particle energy of 9.3 MeV/u and fluence of at maximum $3 \cdot 10^9 \text{ cm}^{-2}$ approximately 2500 particle tracks contribute to the dose in one point, depending on the calculation of the track extension. Figure 11.4 shows the resulting RDDs for different fluences. Figure 11.4a shows calculations conducted with the track extension formalism from [Hansen, 1984]. The RDDs in Figure 11.4b are calculated with the track extension following [Elsässer et al., 2008]. The dose level at same fluence is higher in Figure 11.4a since here more tracks contribute to the dose in one point. Areas of different gray shade indicate the maximal deviation from linearity in this dose range. The *deviation from linearity* is calculated according to the definition in Equation 5.3.

As seen in Figure 11.4 at a fluence of $3 \cdot 10^9 \text{ cm}^{-2}$ the local dose is increased by $\approx 7 \text{ kGy}$ over the whole track area. This increase is not high enough to expect significant changes in the RE since the deviation from linearity is only slightly increased. Comparing Figure 11.4a with Figure 11.4b one can estimate that at a fluence of approximately $1 \cdot 10^{10} \text{ cm}^{-2}$ a significant reduction in the RE would be expected according to the Hansen formulation



(a) Track width Hansen



(b) Track width Elsässer

Figure 11.4: Radial dose distribution for 9.3 MeV/u xenon ions in alanine for different fluences. Figure 11.4a shows calculations conducted with the track extension formalism from [Hansen, 1984]. The RDDs in Figure 11.4b are calculated with the track extension following [Elsässer et al., 2008]. Different shades of gray indicate different levels of deviation from linearity as defined in Equation 5.3.

but also at the maximal applied fluence in the experiment a decrease would be expected. Alanine has the advantage that track overlap effects can be neglected over a wide fluence range. However, this implies that it is not a good system to measure such effects since very high fluences are needed. Unfortunately the measurements with the lithium formate detector show high fluctuations as seen in Figure 8.10. Due to the lower characteristic dose effects of overlapping tracks should be seen at the applied fluences.

The simplification of a homogeneous track distribution in this track overlap model may account for 10 % variation in the resulting dose level. An over- or underestimation in this order of magnitude would not have an impact on the previous discussion.

Data from literature

Figure 10.6 shows the deviations of model calculations from measured data for stopping heavy ions reported in literature. A judgement of the agreement for the different models is difficult. The average absolute deviation for the calculations from the respective data set of the calculations by Hansen and Olsen is 18 %. For the same data set it is 12 % for the modified model, regardless of the D_{37} value. For the data set used by Waligórski *et al.* their calculations deviate in average by 9 % for a D_{37} value of 105 kGy and 10 % for a D_{37} value of 75 kGy. The latter value is a parameter chosen to yield the best results with a modified electron range and is not found by measurements. The deviations of the here presented model for this data set are 7 % for a D_{37} value of 63.1 kGy and 9 % for a D_{37} value of 105 kGy.

The here presented model is in slightly better agreement with data reported in literature than the original model by Hansen and Olsen and the calculations by Waligórski. This is attributed to the new stopping force values, since the impact of the deviation of the here presented model from the original Hansen model is mainly at higher particle energies. Additionally, the available data is for stopping particles, so particle transport calculations based on the stopping force influence the results. The calculated RE for protons is not in agreement with the published data on proton RE. However, this data are very heterogeneous. The values are scattered and partially contradicting each other. Additionally, the values have been measured with detectors with different characteristic doses.

11.3 The definition of the relative effectiveness

The different definitions of the RE do not result in numerical different values for alanine in a dose range below 10 kGy. However, the determination of the RE as done in the experiments and application for dose determination is only possible if the iso-response definition is applied.

For detectors with a lower saturation dose and a none one-hit dose characteristic the difference between definitions also becomes numerical visible.

11.4 Detector response prediction with ATMs

ATMs offer a phenomenological approach to describe and predict the behaviour of detectors in particle beams. The strongest argument for their validity is their good agreement with measured data. The concept of an amorphous track as substitute for a considerations of the stochastic nature of dose deposition can be motivated by its analogy to stopping force calculations.

The alanine detector allows to neglect impact factors as overlapping tracks which makes it a rewarding work to model its response. This is illustrated by the good agreement of the original code by Hansen and Olsen with experimental data at energies above 100 MeV/u even though the track extension was diverging due to the non relativistic calculation of the particle speed. This *robustness* of the alanine detector makes it hard to judge over underlying physics model without going to very high fluences. On the other hand this robustness makes alanine a perfect candidate for practical dosimetry, since overlapping tracks can be neglected in every possible clinical setting, contrary to other solid state detectors.

Track-structure theory and target theory are successful in the description of one-hit response towards particle beams. The main free parameter in the here applied model calculations is the radius a_0 of the hypothetical target area. However, with a variation of a_0 the dose in central part of the particle track is changed. This is the actual parameter which influences the RE, at least in the model calculations. Further investigations in models for the radial dose distributions should also include this factor and not keep it as a free parameter to fit the energy deposition to the LET.

12. Application of the alanine detector in clinical settings

In this chapter the findings of the previous chapters are transferred to clinical problems and energies. The successful application of the response model in a pilot study for a particle facility audit is presented as well as the possible application of alanine as LET estimator. Finally, an analytical formula is introduced to determine the dose to water with alanine measurements in proton and carbon ion beams.

12.1 Ion therapy facility audit with alanine detectors

Inter-facility dosimetry comparisons and audits provide the possibility to find systematic errors in the dosimetric procedures of participating facilities. This is important for new facilities and even more for new techniques. Further standardisation in dosimetry is necessary for exchanging research results and clinical experience.

Assuming an audit, where a dosimetry system gets irradiated at the facilities and evaluated at a third, independent laboratory. Dosimeters should fulfil several requirements, some mandatory, some optional. Mandatory are a reliable and stable readout protocol and predictable detector behaviour. Furthermore the detector signal must not be object of fading over time, or if so a reliable model must exist. Detector response should be least possible influenced by environmental conditions as humidity, air pressure, ambient light or temperature. The dosimeter should be easy to setup and handle, so that no additional uncertainties are introduced. Compact systems have an advantage both in shipping but also a faster installation time allows fewer interference with the normal clinical routine at the facility.

The features of alanine as described in Chapter 5 and the above listed requirements suggest alanine as a suitable dosimeter for inter-facility comparisons. It already has been applied for audits for IMRT [Budgell et al., 2011]. However, for the use of alanine detectors for audits of ion-beam facilities response modelling is inevitable.

A feasibility study has been performed at the Heidelberg Ion-Beam Therapy Center (HIT) and is described by Ableitinger *et al.* [Ableitinger et al., 2012]. While the study covered the development of a whole end-to-end auditing procedure, this discussion mainly focuses on the applicability of the response model in clinical situations. The concept

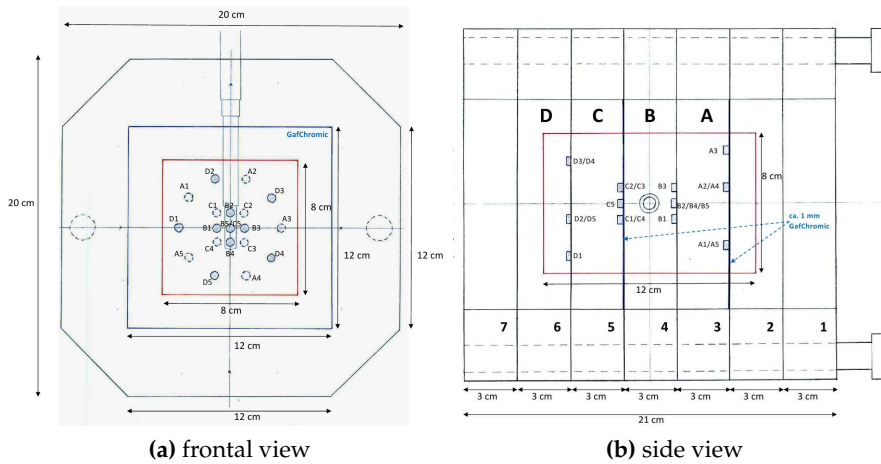


Figure 12.1: Schematic drawing of the phantom used for the study. Figure 12.1a shows the phantom in the beams eye of view. Figure 12.1b shows the phantom as seen from the side. The beam incidents from the left side. The red boxed area represents the target volume. The blue cylinders denote the position of alanine detectors.

and results of the study are presented in this section.

Methods

An octagonal prism, resembling a head phantom consisting of seven slaps of 3 cm thickness was used. The octagonal base has a span of 20 cm. The phantom consists of black polystyrene. Five alanine pellets can be mounted in depths of 5.8, 11.8, 14.8 and 17.8 cm, respectively. A schematic drawing of the phantom and the arrangement of the pellets is shown in Figure 12.1. The red boxed area represents the target volume. The positions of the alanine dosimeter is indicated by blue cylinders. The positions are described by a capital letter indicating the depth in the phantom and a number indicating the position in the slice.

Alanine dosimeters provided by NPL as described in Section 5.3 have been used. They have been readout at the NPL according to standard procedure.

A computer tomography (CT) of the phantom was taken and based on this CT a irradiation plan was created with the local treatment planning system (TPS). A homogeneous dose of 10 Gy has been described to the target volume, a 8 cm x 8 cm x 12 cm rectangular parallelepiped, starting at 4.5 cm depth in the phantom. One irradiation plan was created for irradiation with protons and one with carbon ions.

In order to predict the relative effectiveness for every pellet, the irradiation

tions were simulated in FLUKA. For the irradiation with protons the same procedure as described in Section 7.1 was applied to simulate the beamline.

For carbon ions, additionally, a ripple-filter [Weber and Kraft, 1999], as used during irradiation, was implemented in the calculations. A ripple filter widens mono-energetic Bragg peaks and thus allows to create flat SOBP with less energy steps. It consists of periodic wedge structure. The ripple-filter has been implemented using the method described by Bassler *et al.* [Bassler and others, 2010].

The slice width, and thus the depth resolution of a normal patient CT is 3 mm. The thickness of an alanine pellet, however, is 2.2 mm. In order to increase the quality of the Monte Carlo dose calculations they are based on the actual geometry of the phantom and detectors instead of the information from the CT.

For the calculation of average RE, $\bar{\eta}$, the FLUKA user-routine *comscw* has been modified, as described in [Herrmann *et al.*, 2011b]. Following Equation 3.13 the RE has been calculated as a dose-weighted average of the RE of all energy depositing particles.

With the calculated RE values the physical dose in the pellets can be derived through the iso-response definition of the RE (Equation 3.9). For comparisons with the doses planned by the TPS the dose to water has to be calculated. This is done by multiplication of the physical dose to the alanine pellets with the stopping force ration as defined in Equation 3.5.

The dose to water is then given as:

$$D_w = \frac{1}{\bar{\eta}} \cdot RED_{60Co,w} \cdot S_{(water,alanine)} \quad (12.1)$$

To calculate the stopping force ratio the particle energy spectra in every pellet have been scored using the FLUKA *usrtrack* estimator together with a modified *fluscw* user-routine. The stopping force ratio calculations are based on stopping force values from tables in ICRU report 73 [Sigmund *et al.*, 2005] provided by libdEdx.

Results

The measured RED as well as the dose to water given by the TPS and the calculated values for the RE, the stopping force ratio and the resulting dose to water are given in Table A.3 and Table A.4 in Appendix A. The deviation from the dose to water in the alanine pellets based on the alanine measurements to the values provided by the TPS are in average below 1 % and maximal 4.3 %.

Discussion

The study demonstrates that an inter-facility comparison with alanine pellets is feasible. However, the calculation of the RE required a full Monte Carlo

simulation of the applied treatment in the facility specific beam line setting.

The experiment was designed to verify the dose delivery, with the validity of the alanine-response model postulated. Nevertheless, the overall agreement between calculated and measured dose is a further indication for the validity of the applied track-structure response model.

12.2 Estimation of the dose averaged LET with alanine

As previously mentioned the relation between average LET and biological effects is a discussed topic. However, a recent literature study by Sørensen *et al.* [Sørensen *et al.*, 2011] found indications for a LET dependence of RBE for several cell lines, independent of the ion species. Furthermore, Wenzl *et al.* [Wenzl and Wilkens, 2011] reviewed experimental data from literature and related the OER with the LET, regardless of the ion type. Motivated by these findings an additional biological optimisation of the LET distribution in treatment planing, the so-called *LET-painting* has been proposed [Bassler *et al.*, 2010].

A plan verification of a LET-optimised treatment plan requires a method of measuring the LET. A possibility to estimate the dose-averaged LET with the help of alanine is presented in this section.

Hypothesis

Following the model assumptions on detector response of alanine discussed in Chapter 4 the relative effectiveness η at low doses can be calculated as

$$\eta = D_{37}^{\gamma} \cdot \sigma(E, Z) \left(\frac{S}{\rho} \right)^{-1} \quad (12.2)$$

where D_{37}^{γ} is the characteristic photon dose of the detector, $\sigma(E, Z)$ the activation cross section and $\frac{S}{\rho}$ the mass stopping force of the detector material towards the particle. At a given LET value, different particles have different kinetic energies which - in the model- only affect the maximum extension of the RDD. Thus, the maximum dose inside the track is only minimal affected, as shown in Figure 12.2. As discussed in Chapter 4 the extension of the track has the largest impact for particles at low energies and high stopping forces. For intermediate particle energies, the activation cross section σ does not vary much for different particles with the same LET in an one-hit detector with a high characteristic dose. This behaviour of one-hit detectors has already been postulated by Katz *et al.* [Katz *et al.*, 1972b]. Figure 12.3 demonstrates the influence of the characteristic dose on the RE of a detector towards different particle types. Figure 12.3a shows the relative effectiveness of alanine as a function of particle LET for the lightest six ions. Figure 12.3b shows the same calculations with a detector having a ten times lower characteristic dose. In

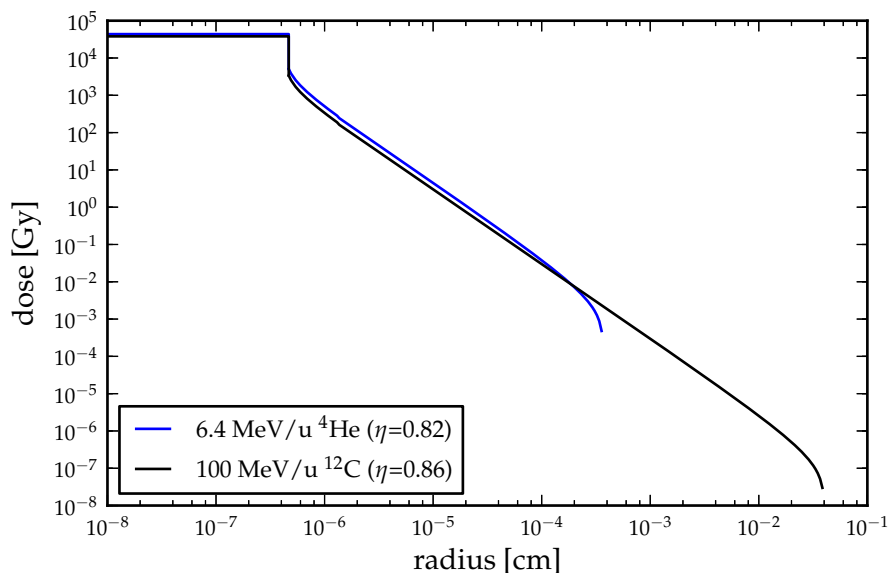


Figure 12.2: Dose in a particle track as a function of distance from particle trajectory for 6.4 MeV/u helium ions and 100 MeV/u carbon ions both with a stopping force of $256 \text{ MeVcm}^2/\text{g}$ in alanine.

Figure 12.3a the curves for all particles are close to each other for LET values below $\approx 200 \text{ keV}/\mu\text{m}$ except for protons. In Figure 12.3b they are further apart.

In a therapeutic carbon ion SOBP the dose-averaged LET does not exceed $\approx 200 \text{ keV}/\mu\text{m}$ [Bassler et al., 2010]. Furthermore, Lühr *et al.* [Lühr et al., 2011a] showed that the primary ion dominates the stopping-force ratio in a therapeutic SOBP. This implies that the dose-averaged LET is also dominated by the primary ion. This assumption can of course only be valid as long as the primary particles is dominating the energy deposition, *i.e.* before and in the Bragg peak, but not in the fragmentation tail. The highest deviation would be expected at the distal end of a Bragg peak, where the amount of secondary particles is highest.

Based on this assumptions the dose-averaged LET could be estimated if the relative effectiveness of the alanine detector is known at this point. In Chapter 7 a method to determine the RE with a combination of alanine dosimeters and a Markus chamber is described. This method, however, could be improved by placing only a single, thin dosimeter in front of the Markus chamber. This would reduce the perturbation of the radiation field by the detector and would minimise the difference in dose between alanine detector and Markus chamber.

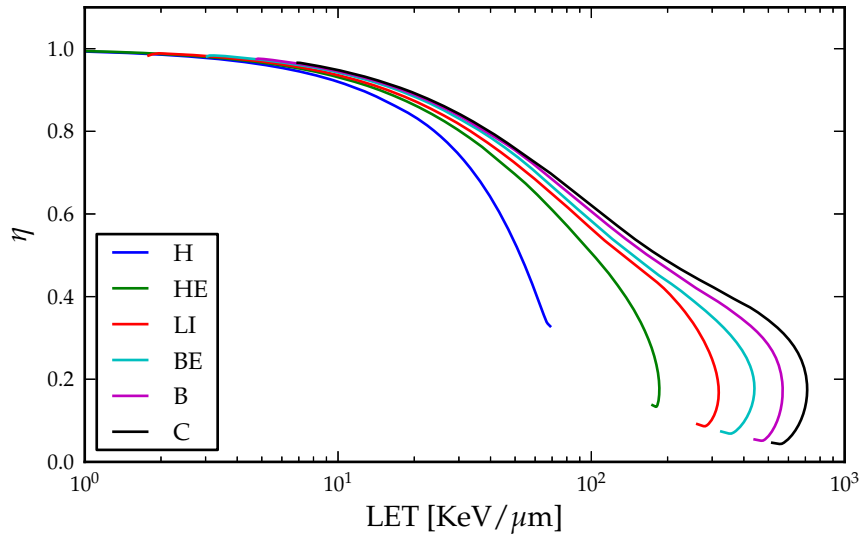
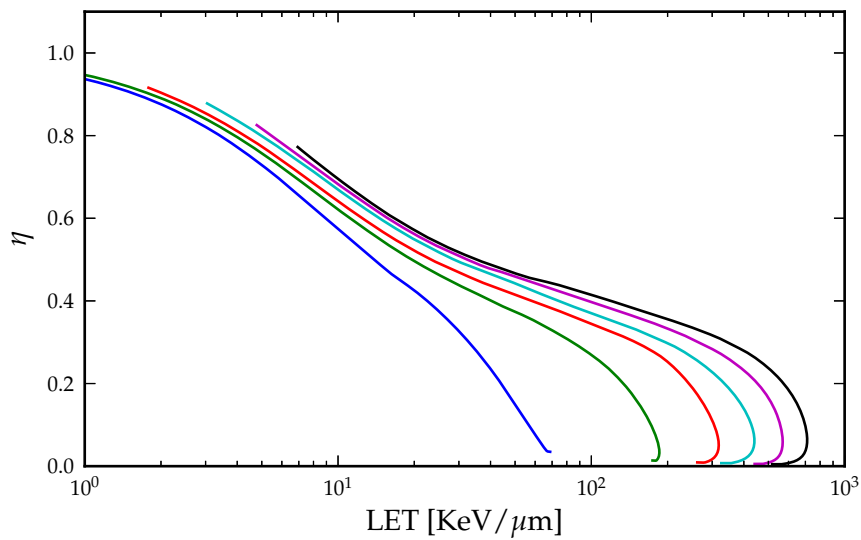
(a) $D_{37} = 63.1$ kGy(b) $D_{37} = 6.31$ kGy

Figure 12.3: Figure 12.3a shows the relative effectiveness of alanine as a function of particle LET for the lightest six ions. Figure 12.3b shows the same calculations with a one-hit detector having a ten times lower characteristic dose. Calculations are done for infinitesimal thin detectors.

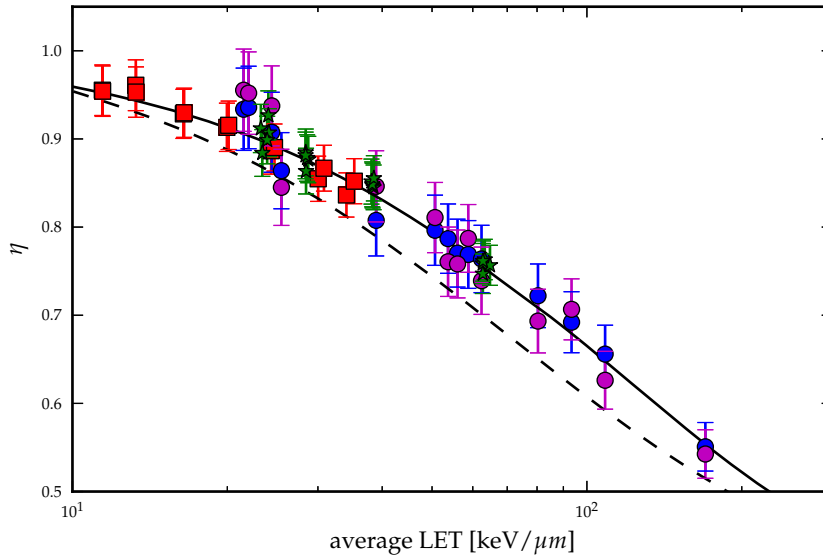


Figure 12.4: The relative effectiveness of alanine towards carbon ions as a function of LET, compared with RE values derived from previous experiments. The solid black line represents the RE of alanine towards carbon ions for infinitesimal thin detectors calculated with the modified response model. The dashed line represents the same calculations done with the original model by Hansen and Olsen. See text for description of the data points.

Results

Figure 12.4 shows the relative effectiveness of alanine towards carbon ions as a function of the LET calculated with the model described in Section 9.2 (black solid line) compared with RE data from previous experiments [Herrmann et al., 2011b, Ableitinger et al., 2012]. The model calculations have been done for infinitesimal thin detectors. For comparison the results of original model by Hansen and Olsen are plotted as dashed black line.

The relative effectiveness data set from the experiment, described in Section 12.1, been calculated from the dose given by the TPS corrected by the stopping force ratio from water to alanine and the RED of the alanine detectors. These data are represented in Figure 12.4 by green stars.

One part of the RE values from [Herrmann et al., 2011b] are directly measured values for mono-energetic carbon ion beams (red squares in Figure 12.4). These values are measured with the method described in Chapter 7. However, these data have been used to estimate the a_0 value for the model calculations. Their agreement with the calculations is obvious. The second part are RE values derived from depth-dose curves of a SOBP, thus in mixed

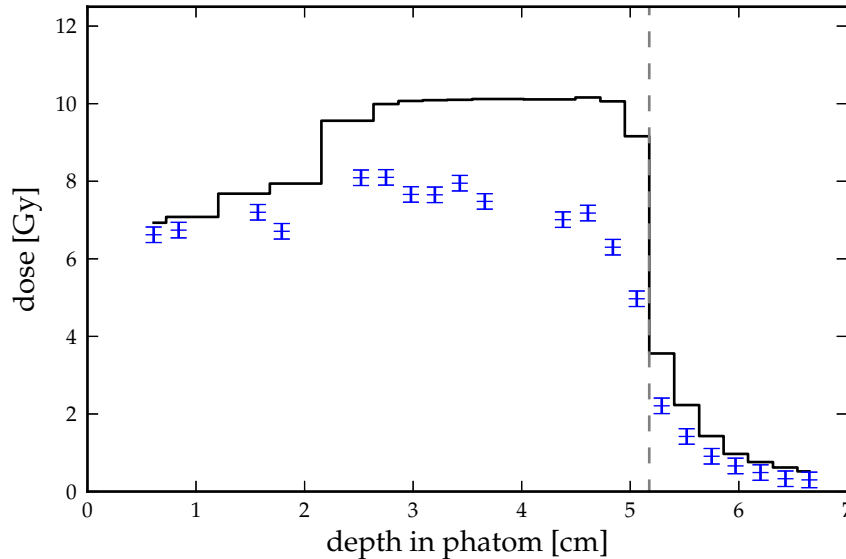


Figure 12.5: Carbon ion SOBP measured with alanine pellets. The blue crosses indicate alanine RED measurements, the black lines the corresponding dose calculated with FLUKA. The data from the region with the gray background is not included in Figure 12.4.

radiation fields (blue circles). The RED in the pellets has been measured, but the dose has been calculated using FLUKA. Error bars indicate 5 % uncertainty due to geometrical uncertainties in the Monte Carlo dose simulations, which are discussed in [Herrmann et al., 2011b]. Following the assumptions only the measured RE data in the entrance and peak region of a SOBP, as indicated in Figure 12.5, have been used. The magenta coloured circles are unpublished data originating from the same experiment and setup as described in [Herrmann et al., 2011b]. The alanine RED data and the calculated doses for this experiment are shown in Figure 12.5. The region of the plot with the gray background is regarded as fragmentation tail. The radiation field region in this region is not dominated by the primary carbon ions. The RE values from this region are thus not included in Figure 12.5.

The corresponding LET values for the extracted RE values have been calculated using FLUKA. The experimental setup has been implemented in FLUKA and the energy-resolved particle spectrum in the pellets has been scored using the *usrtrack* detector combined with a modified *fluscw* user-routine. The dose averaged LET has been calculated by weighting the spectra with stopping force values extracted from SRIM, in order to be consistent with the model calculations.

Discussion

As seen in Figure 12.4 the available experimental data on the relative effectiveness of alanine in a carbon ion beams agree within the experimental uncertainties well with the RE curve calculated for mono-energetic carbon ion beams.

Other authors [Waligorski et al., 1989, Olsen and Hansen, 1988] criticised the presentation of the RE as function of the LET. However, for a single ion the RE can be expressed as a function of LET, as it can as a function of the particle energy. Here, it is shown that in the investigated parameter space, the dose average LET of a radiation field is sufficient to describe the RE, under the assumption that it is dominated by the primary ion.

Horowitz [Horowitz et al., 2003] discussed the topic of LET dependence of relative effectiveness in the context of thermoluminescence (TL) and concluded a) that track structure theory does not allow a dependence of RE on LET only and b) the techniques and protocols of TL dosimetry are not stable enough for this purpose. However, those two points of criticism do not apply to the here suggested estimation of LET, since point a) is taken into account and point b) is fulfilled with the established alanine readout protocols.

The use of alanine for LET determination would have a restricted resolution, though, increasing with higher LET. The limitations on the RE determination are mainly due to the uncertainty of the Markus chamber. An uncertainty of 2 % in the RE results in a uncertainty of 5.5 % at a LET of 136 keV, of 8.0 % at a LET of 23 keV and of 17.5 % at a LET of 23 keV. However, biological effects as OER and RBE are also only elevated at a higher LET values in the order of magnitude of 100 keV and above [Sørensen et al., 2011, Wenzl and Wilkens, 2011]. The here suggested method may serve as a LET estimator in biological experiments with heavy ions.

Even if the here proposed method of LET estimation may not be used for LET measurements, the found relation between dose-averaged LET and the relative effectiveness can instead be used for the calculation of the RE, if the LET of the dominant particle is known.

12.3 Analytic expression for the RE

The findings of the previous section show, that the RE in a carbon ion SOBP is dominated by the primary ions, and that for such a setting the RE can be well described as a function of the LET. In SOBPs with a homogeneous peak dose the LET distribution is similar regardless of the peak width or depth. Therefore, the relative effectiveness in SOBPs can to some extent be described as function of the residual range and the peak width by fitting functions to calculated RE distributions.

The residual range is the distance of a point in a SOBP to the endpoint

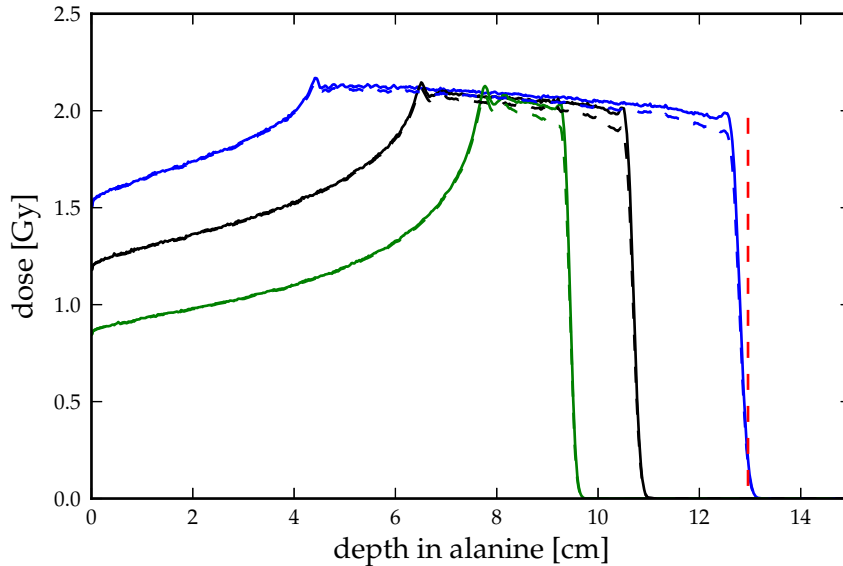


Figure 12.6: Dose as a function of depth for proton SOBPs with different modulation width and total range in alanine. Solid lines represent the dose, dashed lines the predicted RED. The vertical red line indicates the endpoint of the blue SOBP.

of the SOBP. The concept of residual range is motivated by the fact that the radiation field at a certain distance from the endpoint of a dose distribution has the same remaining range, regardless of the initial particle energy. In the CSDA this implies that the particle energy spectra are the same. This is a good assumption for protons, which create only a few fragments and secondary ions. For heavier ions the assumption gets worse with increasing contribution of fragments to the dose. That means that the residual range concept is less valid the higher the initial energy and the heavier the primary particle is.

Here, the endpoint of a proton SOBP is defined in accordance to [Andreo et al., 2004] as the point of 10 % peak dose at the distal dose falloff. For carbon ions the endpoint here is chosen to be at 80 % peak dose.

Figure 12.6 shows the depth dose distributions of three proton SOBPs in alanine calculated with FLUKA. For each of the SOBPs the dose (solid line) as well as the RED (dashed line) is given. The vertical red line gives an example of the endpoint definition.

In proton SOBPs the RE $\eta_{\text{fit}}(R_{\text{res}})$ as a function of the residual range and

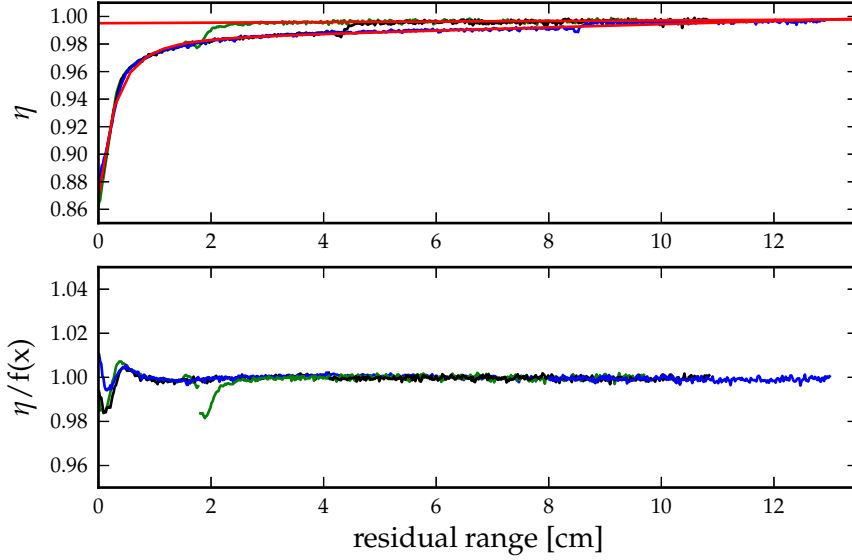


Figure 12.7: The upper part shows the RE as a function of the residual range in the proton SOBPs in alanine shown in Figure 12.6 and fits according to Equation 12.3. The lower part of the figure shows the η to fit ratio.

the width w of the SOBP can be expressed as:

$$\eta_{\text{fit}}(R_{\text{res}}) = \begin{cases} 0.983 - 0.20 \cdot (R_{\text{res}} + 1.16)^{-3.88} + 0.0014 \cdot R_{\text{res}} & : R_{\text{res}} \leq w \\ 2 \cdot 10^{-4} \cdot R_{\text{res}} + 0.995 & : R_{\text{res}} > w \end{cases} \quad (12.3)$$

Figure 12.7 displays in the upper part the RE as function of the residual range for the different SOBPs shown in Figure 12.6 together with the two components of the fitting function. The solid red line represents the fitted function for the peak region ($R_{\text{res}} \leq w$) and the dashed red line the fitted function for plateau region. The lower part of Figure 12.7 shows the ratio of the RE from the Monte Carlo simulation calculation to the RE calculated with the fitted function. The deviation is up to 2 % in the first 2 mm and below 0.2 % thereafter. However, in the transition region $R_{\text{res}} \sim w$ the deviation rises. The deviation rises in this region the narrower the SOBP.

As mentioned previously the residual range concept loses validity for heavier ions thus higher deviations are expected for carbon ion beams. Nevertheless, the RE in a carbon ion SOBP optimised to yield a flat physical dose can also be expressed as function of the residual range.

Through a fit to the three carbon ion SOBPs in alanine shown in Fig-

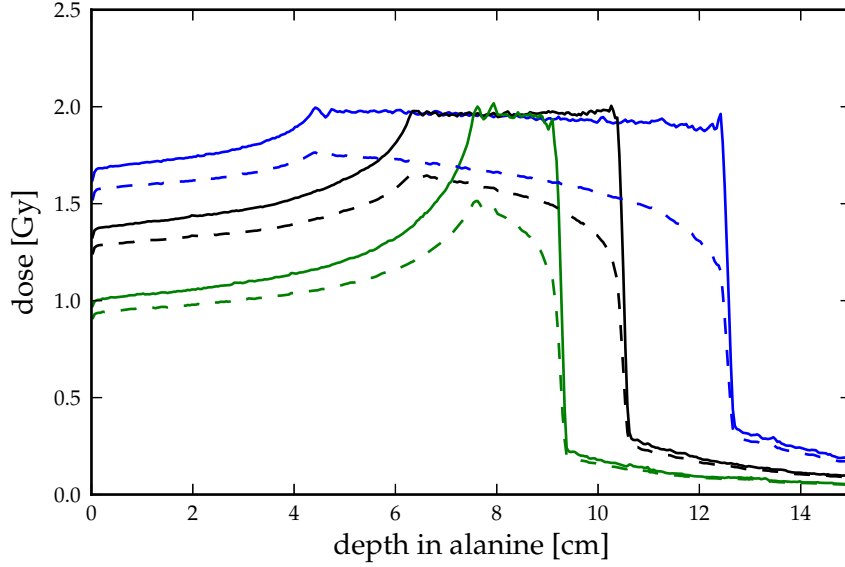


Figure 12.8: Dose as a function of depth for carbon ion SOBPs with different modulation width and total range in alanine. Solid lines represent the dose, dashed lines the predicted RED.

ure 12.8 the following function was found:

$$\eta_{\text{fit}}(R_{\text{res}}) = \begin{cases} 0.963 - 0.235 \cdot (R_{\text{res}} + 0.094)^{-0.294} + 0.0079 \cdot R_{\text{res}} & : R_{\text{res}} \leq w \\ 5.5 - 4.65 \cdot (R_{\text{res}} + \tau)^{-0.03} + 0.007 \cdot R_{\text{res}} & : R_{\text{res}} > w \end{cases} \quad (12.4)$$

The description of the RE in the plateau region ($R_{\text{res}} > w$) is dependent on a value τ which is a linear function of the modulation width w of the investigated SOBP.

$$\tau = 0.155 \cdot w + 0.80 \quad (12.5)$$

Figure 12.9 shows in the upper part the RE as function of the residual range for the SOBPs showed in Figure 12.8. The fitted function describing the RE $\eta(R_{\text{res}}, w)$ is plotted as solid red line in the peak region and dashed red line in the plateau region. The lower part shows the ratio of the RE calculated with the Monte Carlo implementation of the TST and the fitting function. The deviations close to endpoint of the SOBP ($R_{\text{res}} \sim 0$) is up to 4 %. This region is very sensitive to the determination of endpoint and thus to the precision and spatial resolution of the Monte Carlo simulation. Similar to the RE of protons the deviation rises up to 3 % in the border region between peak and plateau. Else the agreement is better than 1 %. Here, the RE in three SOBPs for protons and carbon ions, respectively, with different range and modulation width has been investigated. A simple fitted analytical expression dependent on residual range and modulation width agrees general better than 4 % with results

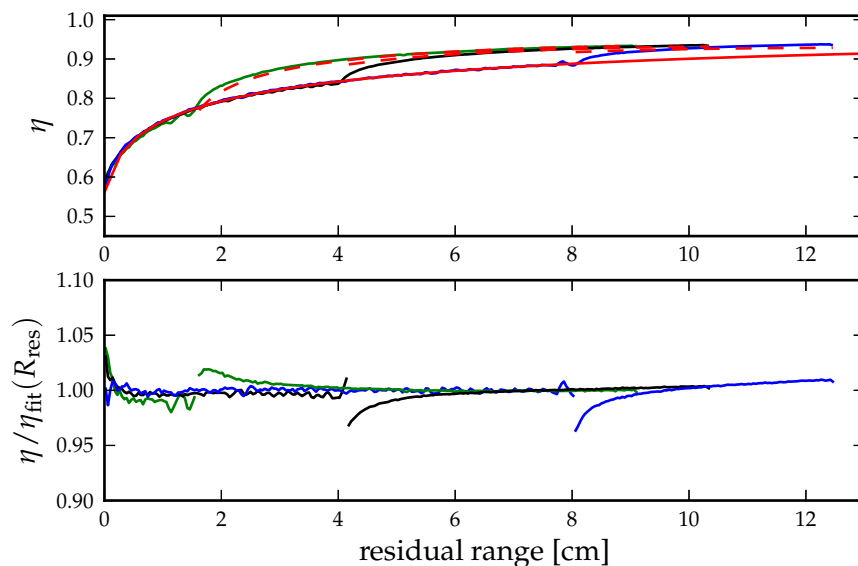


Figure 12.9: The upper part shows the RE as a function of the residual range in the carbon ion SOBPs in alanine shown in Figure 12.8 and fits according to Equation 12.4. The lower part of the figure shows the η to fit ratio. Equation 12.4

of full Monte Carlo simulations. The general validity of the fitted functions is thus proven given the small sample. However, deviations are only to be expected in the order of a view percent in the transition region between peak and plateau, also for SOBPs combinations not explicitly investigated in this study.

The analytic function agrees with the RE values extracted from Section 12.1 as described in Section 12.2 better than 1.6 % for protons and carbon ions. These SOBPs had a total depth of 16.5 cm and a modulation width of 12 cm. All detectors have been placed in the peak region. The residual range has been determined from the extension of the planed SOBP. Since the phantom consisted of polystyrene and the fitting functions have been found for SOBPs in alanine the residual range has been scaled by the density ratio of the two materials.

Lühr *et al.* [Lühr et al., 2011a] suggested that stopping force ratios can be analytically expressed as a function of the residual range. Combined with the here found fitting function for the RE, the dose to water can be determined from the RED with correction factors, which are only dependent on residual range and peak width.

The dose to water D_w can be calculated as

$$D_w = \text{RED} \cdot \eta(R_{\text{res}}, w)^{-1} \cdot S_{(\text{water, alanine})}(R_{\text{res}}) \quad . \quad (12.6)$$

With this formulation alanine can be used to determine dose to water in SOBP without the need of a full Monte Carlo simulation of the set up. The uncertainty level should be below 5 %. Thus, given further experimental validation, this formulation is suitable for use in clinical practise, *e.g.* for the control and documentation of machine output.

13. Conclusions

Synopsis

In this thesis, important steps towards the use of the alanine radiation detector for dosimetry in clinical particle beams have been taken. An existing response model has been adapted for the particle energies used in therapy and its validity was verified using measured data. The definition of the relative effectiveness of detectors has been discussed and arguments favouring an iso-response definition are provided.

It has been shown that alanine dosimeters in combination with track-structure based response models are suitable for dosimetric comparisons or external audits of particle therapy facilities. A simple formalism to estimate the dose to water with alanine dosimeters within a few percent is proposed.

Alanine is a good test system for detector response models because of its one-hit characterisation which prevents supralinearity and since dose contributions of overlapping tracks can be neglected over a wide dose range. A further important advantage is the existence of reliable and comparable read-out protocols. The drawback as test system is that very high fluences have to be applied to see effects from overlapping tracks in alanine. A reliable one-hit detector system with a lower characteristic dose would be desirable for investigation of underlying physical assumptions. Further experiments with the lithium formate one-hit detector have to show if it can be used as such.

Measured data does not allow to draw conclusions on specific assumptions of track structure models. However, the agreement of the response models with the acquired data over a wide energy and dose regime supports the validity of the used model.

Résumé

I nærværende afhandling er væsentlige skridt blevet foretaget i anvendelsen af alanin strålingsdetektorer til dosimetri i kliniske partikelstråler. En eksisterende responsmodel blev tilpasset de partikelenergier som anvendes i stråleterapi, og blev valideret med målte data. Definitionen af den relative effektivitet af detektorer er blevet diskuteret, og argumenter for en iso-respons definition er blevet fremført.

Det er blevet vist, at alanindosimetre i kombination med sporstruktur-baserede responsmodeller er velegnede for klinisk dosimetri eller eksterne revisioner af partikelterapifacilitieter. Der foreslås en simpel formalisme for estimering af dosis til vand indenfor få procent.

Alanin er et velegnet testsystem for detektorresponsmodeller grundet dets et-hit karakteristik, som udelukker supralinearitet og idet dosisbidrag af overlappende spor kan negligeres over et bredt dosisområde. Endvidere er en vigtig fordel tilstedeværelsen af pålidelige og sammenlignelige udlæseprotokoller. Ulempen ved testsystemet er dog, at meget høje fluenser er nødvendige for at se effekter fra sporoverlap i alanin. Et pålideligt et-hit detektorsystem med en lavere karakteristisk dosis ville her være ønskværdig for undersøgelser af de underliggende fysiske antagelser. Eksperimenter med et-hit detektoren lithiumformat må vise om denne kan bruges som sådan.

De målte data tillader ikke konklusioner om specifikke antagelser af sporstrukturmodeller. Imidlertid understøtter overensstemmelsen af responsmodellerne med indsamlede data over et bredt energi- og dosisområde gyldigheden af den anvendte model.

When you finish reading this scroll, tie a stone to it
and throw it into the Euphrates.

JEREMIA 51:63

Appendices

A. Tables

A.1 Relative effectiveness of alanine in carbon ion beams

mean energy [MeV/u]	energy spread [MeVu]	η	uncert.
68.94	3.25	0.836	0.028
76.22	3.50	0.852	0.029
88.16	3.25	0.855	0.029
94.33	3.00	0.867	0.029
109.3	2.70	0.887	0.030
114.6	2.50	0.890	0.030
147.8	2.20	0.913	0.031
152.1	2.00	0.915	0.031
200.7	1.80	0.928	0.032
204.3	1.50	0.930	0.032
291.8	1.15	0.961	0.033
294.6	1.15	0.953	0.032
393.5	1.05	0.955	0.032
395.9	1.05	0.954	0.032

Table A.1: Measured relative effectiveness in carbon ion beams from [Herrmann et al., 2011b].

A.2 Relative effectiveness of alanine in proton beams

mean energy [MeV]	energy spread [MeV]	η	uncert.
104.5	0.7	0.975	± 0.024
106.4	0.6	0.981	± 0.024
114.7	0.6	0.971	± 0.024
116.4	0.6	0.966	± 0.024
125.5	0.6	1.005	± 0.028
127.1	0.5	1.002	± 0.026
135.7	0.6	0.988	± 0.042
137.2	0.6	0.985	± 0.042
145.9	0.6	1.023	± 0.026
147.4	0.5	1.024	± 0.025
156.3	0.6	0.988	± 0.044
157.1	0.5	1.021	± 0.025
166	0.5	0.996	± 0.027
167.3	0.5	0.994	± 0.026
176.6	0.5	0.991	± 0.024
177.8	0.5	0.991	± 0.024
186.7	0.5	1.018	± 0.025
187.9	0.5	1.016	± 0.024
196.4	0.5	1.014	± 0.024
197.6	0.5	1.011	± 0.024
206.0	0.5	0.976	± 0.024
207.7	0.4	0.975	± 0.024
217.7	0.5	0.995	± 0.024
218.8	0.4	0.990	± 0.024

Table A.2: Measured relative effectiveness of alanine in proton beams. The measurements are described in Chapter 7

A.3 Results of the HIT audit study

Tables A.3 and A.4 are listing the results of the audit study conducted at HIT described in Section 12.1 for proton and carbon ion irradiation, respectively. The pellets are named according to Figure 12.1. TPS_{corr} denotes the dose planned by the TPS, corrected by a machine output factor, which varies daily. RED denotes the response equivalent dose in the alanine detectors determined at NPL. The average RE $\bar{\eta}$ and the stopping force ratio $S_{(w,a)}$ have been calculated in FLUKA. The physical dose and the dose to water in the detectors were determined according to Equation 12.1. The deviation between the expected dose TPS_{corr} and the measured dose D_w is calculated as

$$\text{dev} = 1 - \frac{D_w}{\text{TPS}_{\text{corr}}}$$

Pellet	TPS_{corr} [Gy]	RED [Gy]	$\bar{\eta}$	$S_{(w,a)}$	D_{physical} [Gy]	D_w [Gy]	dev
A1	9.87	9.29	0.965	1.023	9.62	9.85	0.20%
A2	9.88	9.27	0.966	1.023	9.60	9.82	0.53%
A3	9.93	–	0.965	1.023	–	–	–
A4	9.93	9.34	0.965	1.023	9.67	9.90	0.28%
A5	9.88	9.31	0.965	1.023	9.65	9.87	0.03%
B1	9.87	9.60	0.988	1.023	9.72	9.95	-0.81%
B2	9.85	9.50	0.987	1.023	9.63	9.85	-0.04%
B3	9.89	9.67	0.987	1.023	9.80	10.02	-1.40%
B4	9.90	9.60	0.987	1.023	9.72	9.95	-0.54%
B5	9.84	9.62	0.985	1.023	9.77	10.00	-1.62%
C1	9.85	9.52	0.989	1.024	9.63	9.86	-0.12%
C2	9.87	9.60	0.991	1.024	9.69	9.92	-0.55%
C3	9.91	9.64	0.991	1.024	9.73	9.96	-0.50%
C4	9.89	9.65	0.991	1.024	9.73	9.96	-0.76%
C5	9.77	9.71	0.989	1.024	9.82	10.05	-2.86%
D1	9.88	9.52	0.991	1.024	9.61	9.85	0.31%
D2	9.91	9.54	0.992	1.024	9.61	9.85	0.58%
D3	9.86	9.68	0.992	1.024	9.76	10.00	-1.43%
D4	9.88	9.69	0.991	1.024	9.78	10.02	-1.44%
D5	9.93	9.66	0.990	1.024	9.75	9.99	-0.64%

Table A.3: Measured and calculated data of the proton irradiation described in Section 12.1

Pellet	TPS _{corr} [Gy]	RED [Gy]	$\bar{\eta}$	$S_{(w,a)}$	D_{physical} [Gy]	D_w [Gy]	dev
A1	9.89	7.42	0.748	1.014	9.92	10.06	-1.76%
A2	9.93	7.41	0.748	1.003	9.90	9.94	-0.12%
A3	9.93	7.30	0.741	1.004	9.84	9.89	0.39%
A4	9.88	7.35	0.746	1.002	9.85	9.87	0.07%
A5	9.82	7.36	0.748	1.004	9.83	9.87	-0.51%
B1	9.89	8.27	0.840	1.014	9.85	9.99	-1.02%
B2	9.90	8.22	0.840	1.015	9.78	9.93	-0.40%
B3	9.89	8.23	0.841	1.018	9.79	9.97	-0.86%
B4	9.88	8.24	0.840	1.013	9.80	9.94	-0.62%
B5	9.85	8.28	0.840	1.017	9.86	10.03	-1.88%
C1	9.93	8.55	0.876	1.024	9.75	9.99	-0.63%
C2	9.92	8.56	0.876	1.025	9.76	10.01	-0.93%
C3	9.91	8.40	0.876	1.026	9.59	9.84	0.66%
C4	9.92	8.62	0.876	1.024	9.84	10.08	-1.65%
C5	9.93	8.60	0.876	1.026	9.82	10.08	-1.43%
D1	9.90	8.59	0.900	1.017	9.55	9.72	1.81%
D2	9.90	8.86	0.900	1.031	9.85	10.16	-2.62%
D3	9.89	9.00	0.899	1.029	10.01	10.30	-4.24%
D4	9.87	8.79	0.899	1.031	9.78	10.08	-2.19%
D5	9.93	8.76	0.899	1.030	9.75	10.04	-1.20%

Table A.4: Measured and calculated data of the carbon ion irradiation described in Section 12.1

A.4 Data from literature

ion	energy [MeV/u]	η	σ_η	D_{37} [kGy]	mode	source
H	1	0.54	0.04	105	stopping	[Olsen and Hansen, 1990]
H	1.63	0.607	0.042	72.6	stopping	[Fattibene et al., 2002]
H	2	0.65	0.02	105	stopping	[Olsen and Hansen, 1990]
H	2.85	0.613	0.043	72.6	stopping	[Fattibene et al., 2002]
H	3	0.74	0.07	105	stopping	[Olsen and Hansen, 1990]
H	3.97	0.633	0.044	72.6	stopping	[Fattibene et al., 2002]
H	5.05	0.652	0.046	72.6	stopping	[Fattibene et al., 2002]
H	6	0.86	0.03	105	stopping	[Olsen and Hansen, 1990]
H	6.1	0.623	0.056	72.6	stopping	[Fattibene et al., 2002]
H	10.2	0.64	0.13		stopping	Ebert 1965 +
H	12.6	0.61	0.12		stopping	Ebert 1965 +
H	14	0.69	0.14		stopping	Bradshaw 1962 +
H	14.5	0.69	0.14		stopping	Ebert 1965 +
H	15.6	0.92	0.032	72.6	crossing	[Bartolotta et al., 1999]
H	15.8	0.7	0.14		stopping	Ebert 1965 +
H	16	1	0.03	105	stopping	[Olsen and Hansen, 1990]
H	24.9	0.96	0.034	72.6	crossing	[Bartolotta et al., 1999]
H	62	0.97	0.02	72.6	crossing	[Onori et al., 1997]
H	40	1.017	0.051	72.6	crossing	[Cuttone et al., 1999]
H	60	0.99	0.05	72.6	crossing	[Cuttone et al., 1999]
H	160	1	./.	110	crossing	Bermann 1978 +
He	5	0.58	./.	105	stopping	[Hansen et al., 1987]
He	10.4	0.99	./.		crossing	[Henriksen, 1966]*
He	58.6	1	./.	110	stopping	Bermann 1978 +
He	162.5	1	./.	110	crossing	Bermann 1978 +
Li	3	0.7	./.	105	stopping	[Hansen et al., 1987]
Li	10.4	0.88	./.		crossing	[Henriksen, 1966] *
B	10.4	0.61	./.		crossing	[Henriksen, 1966] *
C	10.4	0.55	./.		crossing	[Henriksen, 1966] *
O	4	0.32	0.02	105	stopping	[Olsen and Hansen, 1990]
O	10.4	0.41	0.04		stopping	[Henriksen, 1966] *
F	10.4	0.41	0.04		stopping	[Henriksen, 1966] *
Si	10.4	0.35	0.04		stopping	[Henriksen, 1966] *
S	2.5	0.25	./.	105	stopping	[Hansen et al., 1987]
Ar	18.5	0.37	0.02	105	stopping	[Olsen and Hansen, 1990]
Ar	10.4	0.31	0.04		stopping	[Henriksen, 1966] *
Ni	15.4	0.35	0.07		stopping	[Olsen and Hansen, 1990]
Pb	13.8	0.25	0.05	105	stopping	[Olsen and Hansen, 1990]
U	15	0.33	0.06	105	stopping	[Olsen and Hansen, 1990]
U	5.9	0.27	0.03	105	stopping	[Olsen and Hansen, 1990]

Table A.5: Collection of literature data on the RE of alanine. If sources are marked with “+” the values have been given in [Waligorski et al., 1989], if marked with “*” values have been extracted from graphs in original article. The column *mode* indicates if the particles stopped in the detector or crossed the detector.

ion	energy [MeV/u]	η_{meas}	σ_{η}	η_{calc}^+	dev	η_{calc}^*	dev
He	5.0	0.58	0.03	0.65	-12%	0.64	-10%
He	10.4	0.99		0.76	23%	0.74	25%
Li	3.0	0.37	0.04	0.43	16%	0.44	18%
Li	10.4	0.88		0.63	29%	0.62	30%
B	10.4	0.61		0.47	23%	0.48	22%
C	10.4	0.55		0.43	21%	0.45	19%
O	4.0	0.41	0.02	0.32	22%	0.35	15%
O	10.4	0.32		0.39	-23%	0.41	-29%
F	10.4	0.41		0.38	9%	0.40	3%
Ne	10.4	0.38		0.37	4%	0.39	2%
Si	10.4	0.35		0.35	-1%	0.38	-9%
S	2.5	0.25	0.25	0.23	7%	0.26	-4%
Ar	10.4	0.31		0.34	-8%	0.36	-17%
Ar	18.5	0.37	0.02	0.37	1%	0.39	-6%
Ni	15.2	0.35	0.07	0.35	-0.1%	0.38	-7%
Ca	15.4	0.34	0.02	0.33	3%	0.35	-4%
Pb	13.8	0.25	0.05	0.28	-13%	0.31	-23%
U	5.9	0.27	0.03	0.21	21%	0.24	12%
U	15.0	0.33	0.06	0.26	21%	0.28	14%

Table A.6: Comparison of RE data from literature for ions heavier than protons with model calculations for $+D_{37} = 63.1$ kGy and $*D_{37} = 105$ kGy. The data is visualised in Figure 10.6.

B. Track-structure formulations

In the following formulae m_e and e denotes the rest mass and charge of an electron, retrospectively. β denotes the speed of the projectile ion relative to the speed of light and E its kinetic energy in MeV/u .

B.1 Track extension formulae

[Hansen, 1984]

$$r_{max} = 0.5962 \cdot \left(\frac{\beta^2}{1 - \beta^2} \right)^{1.676} \quad [\text{gcm}^{-2}] \quad (\text{B.1})$$

[Waligorski et al., 1986]

$$r_{max} = 6 \cdot 10^{-6} \cdot \left(2m_e \frac{\beta^2}{1 - \beta^2} \right)^\alpha \quad [\text{gcm}^{-2}] \quad (\text{B.2})$$

$$\alpha = \begin{cases} 1.079 & : \text{ for } \beta < 0.03 \\ 1.667 & : \text{ for } \beta > 0.03 \end{cases} \quad (\text{B.3})$$

[Scholz and Kraft, 1996]

$$r_{max} = 5 \cdot 10^{-6} \cdot (E)^{1.7} \quad [\text{gcm}^{-2}] \quad (\text{B.4})$$

[Elsässer et al., 2008]

$$r_{max} = 6.2 \cdot 10^{-6} \cdot (E)^{1.7} \quad [\text{gcm}^{-2}] \quad (\text{B.5})$$

[Tabata et al., 1972]

$$r_{max} = a_1 \left[\frac{1}{a_2} \log(1 + a_2 \tau) - a_3 \tau (1 + a_4 \tau^{a_5}) \right] \quad [\text{gcm}^{-2}] \quad (\text{B.6})$$

where $\tau = 2 \cdot \frac{\beta^2}{1 - \beta^2}$ and a_i is defined as:

$$\begin{aligned} a_1 &= \frac{b_1 A_T}{Z_T^{b_2}} \\ a_2 &= b_3 Z_T \\ a_3 &= b_4 - b_5 Z_T \\ a_4 &= b_6 - b_7 Z_T \\ a_5 &= \frac{b_8}{Z_T^{b_9}} \end{aligned} \quad (\text{B.7})$$

with Z_T representing the average atomic number and A_T representing the average atomic mass of the target material. The parameter b_i are determined as :

i	b_i	
1	0.2335	± 0.0091
2	1.290	± 0.015
3	(1.78	$\pm 0.36) \cdot 10^{-4}$
4	0.9891	± 0.001
5	(3.01	$\pm 0.35) \cdot 10^{-4}$
6	1.468	± 0.09
7	(1.180	$\pm 0.097) \cdot 10^{-2}$
8	1.232	± 0.067
9	0.109	± 0.017

Acknowledgements

This project has been supported by CIRRO - The Lundbeck Foundation Center for Interventional Research in Radiation Oncology and The Danish Council for Strategic Research. It also received support from the Danish Cancer Society.

I am grateful to these organisations for financing this PhD project. I am obliged to Jens Overgaard who facilitated the financial support.

I am grateful to Søren Pape Møller for being main supervisor of this PhD project and always having an open ear.

Most of all I have to thank Niels Bassler, who guided my scientific career since the start of my Master project four years ago. He is the one who offered me the *adventure* Denmark and at times helped to keep the time adventurous. I learned a lot, not only with regard to physics and Linux. Thank you for these sometimes a little stressful, sometimes a little challenging but always interesting times.

I thank Jørgen B. B. Petersen for the insight into the clinical point of view on dosimetry and the shared wisdom and some crazy ideas.

I am thankful for the many hours of discussions with Armin Lühr, on physics, university and the rest of the world. It is also partly thanks to his merits, that this thesis is in a somewhat readable English.

I am grateful to Oliver Jäkel for the continued cooperation with his group and hosting my visits at the DKFZ. I thank Steffen Greulich for the discussions on detectors, track-structure models and what else matters in the world and the breakfasts in Heidelberg.

I am deeply indebted to Peter Sharpe and Hugo Palmans from the NPL not only for providing and analysing the alanine detectors but also the discussions of my alanine project and the implications of the experimental results.

I received help from a number of people during the last three years to whom I owe gratitude: Ari Virtanen, who made the experiments at RADEF possible; Heikki Kettunen and Mikko Rossi for the technical support during the experiment; Ingerid Knudtsen for the help and company during the RADEF beam time, even though the experiment was not related to her research. Furthermore for the help and hospitality during my short stay in Oslo; Eirik Malinen and Andre Krivokapic from The Norwegian Radium Hospital, Oslo University Hospital for provision and readout of the lithium formate detectors; Julia-Maria Osniga and Grischa Klimpski for the readout of the FNTD at the DKFZ; Stefan Brons for the help during the experiment at

HIT; Jacques Chevalier for taking pictures of alanine pellets with the AFM;
Bjarne Thomsen for providing and administrating the cluster;

Bibliography

- [Ableitinger et al., 2012] Ableitinger, A., Vatrinsky, S., Herrmann, R., Bassler, N., Palmans, H., Sharpe, P., Jäkel, O., Ecker, S., Chaudhri, N., and Georg, D. (2012). Dosimetry auditing procedure with alanine dosimeters for particle therapy. *in preparation* .
- [Ahlers and Schneider, 1991] Ahlers, F. J. and Schneider, C. C. J. (1991). Alanine ESR Dosimetry: An Assessment of Peak-to-Peak Evaluation. *Radiat. Prot. Dosim.*, 37(2):117–122.
- [Akselrod and Sykora, 2011] Akselrod, M. S. and Sykora, G. J. (2011). Fluorescent nuclear track detector technology – A new way to do passive solid state dosimetry. *Radiation Measurements*, 46(12):1671–1679. Proceedings of the 16th Solid State Dosimetry Conference , September 19-24 , Sydney , Australia.
- [Andreo, 2009] Andreo, P. (2009). On the clinical spatial resolution achievable with protons and heavier charged particle radiotherapy beams. *Phys. Med. Biol.*, 54:205–215.
- [Andreo et al., 2004] Andreo, P., Burns, D. T., Hohlfeld, K., Huq, M. S., Kanai, T., Laitano, F., Smyth, V., and Vynckier, S. (2004). Absorbed Dose Determination in External Beam Radiotherapy: An International Code of Practice for Dosimetry based on Standards of Absorbed Dose to Water. Technical Report 398.
- [Anton, 2005] Anton, M. (2005). Development of a secondary standard for the absorbed dose to water based on the alanine EPR dosimetry system. *Appl. Radiat. Isotopes*, 62(5):779–95.
- [Arber and Sharpe, 1993] Arber, J. M. and Sharpe, P. H. G. (1993). Fading Characteristics of Irradiated Alanine Pellets: The Importance of Pre-Irradiation Conditioning. *Appl. Radiat. Isotopes*, (44):19–22.
- [Bartolotta et al., 1999] Bartolotta, A., Barone Tonghi, L., Brai, M., , G., Fatibene, P., Onori, S., Raffaele, L., Rovelli, A., Sabini, M. G., and Teri, G. (1999). Response Characteristics of Thermoluminescence and Alanine-based Dosimeters to 16 and 25 MeV Proton Beams. *Radiat. Prot. Dosim.*, 85(1-4):353–356.

- [Bartolotta et al., 1984] Bartolotta, A., Indovina, P. L., Onori, S., and Rosati, A. (1984). Dosimetry for cobalt-60 gamma rays with alanine. *Radiat. Prot. Dosim.*, 9(4):277.
- [Bassler et al., 2008] Bassler, N., Hansen, J. W., Palmans, H., Holzscheiter, M. H., Kovacevic, S., and the AD-4/ACE collaboration (2008). The Antiproton Depth Dose Curve Measured with Alanine Detectors. *Nucl. Instrum. Meth. B*, 266(6):929–936.
- [Bassler et al., 2010] Bassler, N., Jäkel, O., Søndergaard, C. S., and Petersen, J. B. (2010). Dose- and LET-painting with particle therapy. *Acta Oncol.*, 49(7):1170–6.
- [Bassler and others, 2010] Bassler, N. and others, a. (2010). Comparison of optimized single and multifield irradiation plans of antiproton, proton carbon ion beams. *Radiother. Oncol.*, 95:87–93.
- [Battistoni et al., 2007] Battistoni, G., Muraro, S., Sala, P. R., Cerutti, F., Ferrari, A., Roesler, S., Fassò, A., and Ranft, J. (2007). FLUKA: a multi-particle transport code. *Proceedings of the Hadronic Shower Simulation Workshop 2006, Fermilab 6–8 September 2006, M. Albrow, R. Raja eds., AIP Conference Proceeding*, 896:31–49.
- [Baumert et al., 2001] Baumert, B., Lomax, A., Miltchev, V., and Davis, J. (2001). A comparison of dose distributions of proton and photon beams in stereotactic conformal radiotherapy of brain lesions. *Int. J. Radiat. Oncol., Biol., Phys.*, 49(5):1439–1449.
- [Berger et al., 2005] Berger, M. J., Coursey, J. S., Zucker, M. A., and Chang, J. (2005). ESTAR, PSTAR, and ASTAR: Computer Programs for Calculating Stopping-Power and Range Tables for Electrons, Protons, and Helium Ions (version 1.2.3).
- [Bernier et al., 2004] Bernier, J., Hall, E., and Giaccia, A. (2004). Radiation oncology: a century of achievements. *Nature Reviews Cancer*, 4(9):737–747.
- [Boag and Curren, 1980] Boag, J. W. and Curren, J. (1980). Current Collection and Ionic Recombination in Small Cylindrical Ionization Chambers Exposed to Pulsed Radiation. *Brit. J. Radiol.*, 53:471–478.
- [Bradshaw et al., 1962] Bradshaw, W. W., Cadena, D. G., Crawford, G. W., and Spetzler, H. A. W. (1962). The Use of Alanine as a Solid Dosimeter. *Radiat. Res.*, 17:11–21.
- [Bragg and Kleeman, 1905] Bragg, W. H. and Kleeman, R. (1905). On the Alpha Particles of Radium and Their Loss of Range in Passing Through Various Atoms and Molecules. *Philos. Mag.*, 10:318–340.

- [Brahme, 1984] Brahme, A. (1984). Dosimetric precision requirements in radiation therapy. *Acta Oncol.*, 23(5):379–391.
- [Budgell et al., 2011] Budgell, G., Berresford, J., Trainer, M., Bradshaw, E., Sharpe, P., and Williams, P. (2011). A national dosimetric audit of IMRT. *Radiother. Oncol.*, 99(2):246–52.
- [Butts and Katz, 1967] Butts, J. J. and Katz, R. (1967). Theory of RBE for Heavy Ion Bombardment of Dry Enzymes and Viruses. *Radiat. Res.*, 30:855–871.
- [Chappell and Fowler, 1994] Chappell, R. and Fowler, J. (1994). Steepness of dose-response curve for larynx cancer. *Radiother. Oncol.*, 30(1):90.
- [Chatterjee and Schaefer, 1976] Chatterjee, A. and Schaefer, H. J. (1976). Microdosimetric structure of heavy ion tracks in tissue. *Radiat. Environ. Bioph.*, 13(3):215–227.
- [Ciesielsk et al., 1998] Ciesielsk, B., Stuglik, Z., Wielopolski, L., and Zvara, I. (1998). The Effect of High-Linear Energy Transfer Ions on the Electron Paramagnetic Resonance Signal Induced in Alanine. *Radiat. Res.*, 150:498–474.
- [Ciesielski et al., 1988] Ciesielski, B., Wielopolski, L., and Reinstein, L. E. (1988). The energy response of agar-alanine phantom dosimeter to gamma radiation. *Med. Phys.*, 15:380.
- [Cuttone et al., 1999] Cuttone, G., Raffaele, L., Barone Tonghi, L., Rovelli, A., Sabini, M. G., Egger, E., Kacperek, A., Brai, M., Bartolotta, A., Teri, G., et al. (1999). First dosimetry intercomparison results for the CATANA project. *Phys. Medica.*
- [De Ruyscher et al., 2012] De Ruyscher, D., Mark, L., Jones, B., Brada, M., Munro, A., Jefferson, T., and Pijls-Johannesma, M. (2012). Charged particles in radiotherapy: A 5-year update of a systematic review. *Radiother. Oncol.*
- [Delaney et al., 2005] Delaney, G., Jacob, S., Featherstone, C., and Barton, M. (2005). The role of radiotherapy in cancer treatment. *Cancer*, 104(6):1129–1137.
- [Dementyev and Sobolevsky, 1999] Dementyev, A. V. and Sobolevsky, N. M. (1999). SHIELD – universal Monte Carlo hadron transport code: scope and applications. *Radiat. Meas.*, 30(5):553–557.
- [Dertinger and Jung, 1969] Dertinger, H. and Jung, H. (1969). *Molekulare Strahlenbiologie*. Springer-Verlag.

- [Durante and Loeffler, 2010] Durante, M. and Loeffler, J. S. (2010). Charged particles in radiation oncology. *Nat Rev Clin Oncol*, 7(1):37–43.
- [Ebert et al., 1965] Ebert, P. J., Hardy, K. A., and Cadena, D. G. (1965). Energy Dependence of Free Radical Production in Alanine. *Radiat. Res.*, 26(2):178–197.
- [Edmund et al., 2007] Edmund, J. M., Andersen, C. E., and Greulich, S. (2007). A track structure model of optically simulated luminescence from $\text{Al}_2\text{O}_3\text{:C}$ irradiated with 10-60 MeV protons. *Nucl. Instrum. Meth. B*, 262:261–275.
- [Elsässer et al., 2008] Elsässer, T., Krämer, M., and Scholz, M. (2008). Accuracy of the Local Effect Model for the Prediction of Biologic Effects of Carbon Ion Beams in vitro and in vivo. *Int. J. Radiat. Oncol., Biol., Phys.*, 71(3):886–872.
- [Fassò et al.,] Fassò, A., Ferrari, A., Ranft, J., and Sala, P. R. The FLUKA code: Description and Benchmarking. *CERN-2005-10 (2005), INFN/TC 05/11, SLAC-R-773*.
- [Fattibene et al., 2002] Fattibene, P., De Angelis, C., Onori, S., and Cherubini, R. (2002). Alanine Response to Proton Beams in the 1.6 - 6.1 MeV Energy Range. *Radiat. Prot. Dosim.*, 101(1-4):465–468.
- [Fettouhi et al., 2006] Fettouhi, A., Geissel, H., Schinner, A., and Sigmund, P. (2006). Stopping of high-Z ions at intermediate velocities. *Nucl. Instrum. Meth. B*, 245(1):22–27.
- [Gall et al., 1996] Gall, K., Desrosiers, M., Bensen, D., and Serago, C. (1996). Alanine EPR Dosimeter Response in Proton Therapy Beams. *Appl. Radiat. Isotopes*, 47(11/12):1197–1199.
- [Geiß et al., 1998] Geiß, O. B., Krämer, M., and Kraft, G. (1998). Efficiency of thermoluminescent detectors to heavy charged particles. *Nucl. Instrum. Meth. B*, 142:592–598.
- [Gerstenberg et al., 1990] Gerstenberg, H. M., Hansen, J. W., Coyne, J. J., and Zoetelief, J. (1990). Calculations of the Relative Effectiveness of Alanine for Neutrons with Energies up to 17.1 MeV. *Radiat. Prot. Dosim.*, 31(1/4):85–9.
- [Giesen et al., 2007] Giesen, U., Brede, H. J., and Greif, K.-D. (2007). Dosimetry with a transportable water calorimeter in neutron, proton and heavy-ion radiation fields. *Radiat. Prot. Dosim.*, 126(1-4):600–603.
- [Glasser et al., 1952] Glasser, O., Quimby, E. H., Taylor, L. S., and Weatherwax, J. L. (1952). *Physical Foundations of Radiology*. Cassell and Company Limited, 2. edition.

- [Greilich et al., 2008] Greilich, S., Edmund, J. M., Jain, M., and Andersen, C. E. (2008). A coupled RL and transport model for mixed-field proton irradiation of Al₂O₃:C. *Radiat. Meas.*, 43(2–6):1049–1053. Proceedings of the 15th Solid State Dosimetry (SSD15).
- [Greilich et al., 2010] Greilich, S., Grzanka, L., Bassler, N., Andersen, C. E., and Jäkel, O. (2010). Amorphous track models: A numerical comparison study. *Radiat. Meas.*, 45(10):1406–1409.
- [Greilich et al., 2012a] Greilich, S., Hahn, U., Kiderlen, M., Andersen, C. E., and Bassler, N. (2012a). An algorithm for rapid calculation of solid-state detector efficiency. *submitted to PMB*.
- [Greilich et al., 2012b] Greilich, S., Osinga, J., Lauer, F., Niklas, M., Akselrod, M. S., and Jäkel, O. (2012b). Quantative read-out of Al₂O₃:C,Mg-based fluorescent nuclear track detectors using a commercial confocal microscope. *in preparation*.
- [Grzanka et al., 2011] Grzanka, L., Greilich, S., Korcyl, M., Jäkel, O., Waligórski, M., and Olko, P. (2011). The application of amorphous track models to study cell survival in heavy ions beams. *Radiat. Prot. Dosim.*
- [Hansen et al., 2012a] Hansen, D. C., Lühr, A., Herrmann, R., Sobolevsky, N., and Bassler, N. (2012a). Recent Improvements in the SHIELD-HIT Code. *Int. J. Rad. Biol.*, 88(1-2):195–9.
- [Hansen et al., 2012b] Hansen, D. C., Lühr, A., Sobolevsky, N., and Bassler, N. (2012b). Optimizing SHIELD-HIT for carbon ion treatment. *Phys. Med. Biol.*
- [Hansen, 1984] Hansen, J. W. (1984). *Experimental Investigation of the Suitability of the Track Structure Theory in Describing the Relative Effectiveness of High-LET Irradiation of Physical Radiation Detectors*. PhD thesis, Risø National Laboratory.
- [Hansen and Olsen, 1984] Hansen, J. W. and Olsen, K. J. (1984). Experimental and Calculated Response of a Radiochromic Dye Film Dosimeter to High-LET Radiations. *Radiat. Res.*, 91:1–15.
- [Hansen and Olsen, 1985] Hansen, J. W. and Olsen, K. J. (1985). Theoretical and Experimental Radiation Effectiveness of the Free Radical Dosimeter Alanine to Irradiation with Heavy Charged Particles. *Radiat. Res.*, 104(1):15–27.
- [Hansen and Olsen, 1989] Hansen, J. W. and Olsen, K. J. (1989). Predicting Decay in Free-radical Concentration in L- α -Alanine Following High-LET Radiation Exposures. *Appl. Radiat. Isotopes*, 40(10-12):935–939.

- [Hansen et al., 1987] Hansen, J. W., Olsen, K. J., and Wille, M. (1987). The Alanine Radiation Detector for High and Low LET Dosimetry. *Radiat. Prot. Dosim.*, 19(1):43–47.
- [Henriksen, 1966] Henriksen, T. (1966). Production of Free Radicals in Solid Biological Substances by Heavy Ions. *Radiat. Res.*, 27(4):676–693.
- [Herrmann et al., 2011a] Herrmann, R., Greilich, S., Grzanka, L., and Bassler, N. (2011a). Amorphous track predictions in ‘libamtrack’ for alanine relative effectiveness in ion beams. *Radiat. Meas.*, 46(12):1551–1553.
- [Herrmann et al., 2011b] Herrmann, R., Jäkel, O., Palmans, H., Sharpe, P., and Bassler, N. (2011b). Dose Response of Alanine Detectors Irradiated with Carbon Ion Beams. *Med. Phys.*, 38(4):1859–1866.
- [Herrmann et al., 2009] Herrmann, R., Petersen, J., and Bassler, N. (2009). Monte Carlo calculations of dose to medium and dose to water for carbon in beams in various media. In *Proc. 48th Meeting of the Particle Therapy Co-Operative Group (PTCOG)*, page 124, Düsseldorf. German Medical Science Publishing House.
- [Holzscheiter et al., 2004] Holzscheiter, M. H. et al. (2004). Biological Effectiveness of Antiproton Annihilation. *Nucl. Instrum. Meth. B*, 221:210–214.
- [Horowitz et al., 2003] Horowitz, Y. S., Satinger, D., Fuks, E., Oster, L., and L., P. (2003). ON THE USE OF LiF:Mg,Ti THERMOLUMINESCENCE DOSEMETERS IN SPACE — A CRITICAL REVIEW . *Radiat. Prot. Dosim.*, 106(1):7–24.
- [Hubert et al., 1989] Hubert, F., Bimbot, R., and Gauvin, H. (1989). Semi-empirical formulae for heavy ion stopping powers in solids in the intermediate energy range. *Nucl. Instrum. Meth. B*, 36(4):357–363.
- [ICRU, 1993] ICRU (1993). Stopping powers and ranges for protons and alpha particles. Technical Report 60, International Commission on Radiation Units and Measurements.
- [ICRU, 1998] ICRU (1998). Fundamental Quantities and Units for Ionizing Radiation. Technical Report 60, International Commission on Radiation Units and Measurements.
- [ICRU, 2008] ICRU (2008). Dosimetry Systems. *Journal of the ICRU*, 8(2).
- [ISO/ASTM, 2002] ISO/ASTM (2002). ISO/ASTM 51261: Guide for Selection and Calibration of Dosimetry Systems for Radiation Processing. Technical report, ISO/ASTM, ASTM International, West Conshohocken, PA.

- [ISO/ASTM, 2004] ISO/ASTM (2004). ISO/ASTM 51607: Practice for Use of an Alanine-EPR Dosimetry System. Technical report, ISO/ASTM, ASTM International, West Conshohocken, PA.
- [ISP Technologies inc., 1996] ISP Technologies inc. (1996). *GAFCHROMIC HS radiochromic dosimetry films for high energy photons configuration, specification and performance data*.
- [Javanainen et al., 2009] Javanainen, A. et al. (2009). Experimental Linear Energy Transfer of Heavy Ions in Silicon for RADEF Cocktail Species. *IEEE Transactions on Nuclear Science*, 56(4):2242–2246.
- [Jirasek and Duzenli, 2002] Jirasek, A. and Duzenli, C. (2002). Relative effectiveness of polyacrylamide gel dosimeters applied to proton beams: Fourier transform Raman observations and track structure calculations. *Med. Phys.*, 29(4):569–577.
- [Kaiser et al., 2010] Kaiser, F.-J., Bassler, N., Tölli, H., and Jäkel, O. (2010). Ionization chambers for LET determination. *Radiat. Meas.*, In Press, Accepted Manuscript.
- [Kanai et al., 1998] Kanai, T., Sudo, M., Naruhiro, M., and Yasuyuki, F. (1998). Initial recombination in a parallel-plate ionization chamber exposed to heavy ions. *Phys. Med. Biol.*, 43:3549–3558.
- [Karger et al., 2010] Karger, C., Jäkel, O., Palmans, H., and Kanai, T. (2010). Dosimetry for ion beam radiotherapy. *Phys. Med. Biol.*, 55:193–234.
- [Karger and Jäkel, 2007] Karger, C. P. and Jäkel, O. (2007). Current status and new developments in ion therapy. *Strahlenther Onkol*, 183(6):295–300.
- [Katz, 1978] Katz, R. (1978). Track Structure Theory in Radiobiology and in Radiation Detection. *Nucl. Track Detect.*, 2(1):1–28.
- [Katz, 1993] Katz, R. (1993). Relative Effectiveness of Mixed Radiation Fields. *Radiat. Res.*, 133(3):390.
- [Katz, 2003] Katz, R. (2003). COMMENTARY: The Parameter-Free Track Structure Model of Scholz and Kraft for Heavy-Ion Cross Sections. *Radiat. Res.*, 160:724–728.
- [Katz et al., 1971] Katz, R., Ackerson, B., Homayoonfar, M., and Sharma, S. C. (1971). Inactivation of Cells by Heavy Ion Bombardment. *Radiat. Res.*, 47:402–425.
- [Katz et al., 1996] Katz, R., Cucinotta, F., and Zhang, C. (1996). The calculation of radial dose from heavy ions: predictions of biological action cross sections. *Nucl. Instrum. Meth. B*, 107(1):287–291.

- [Katz et al., 1972a] Katz, R., Sharma, S. C., and Homayoonfar, M. (1972a). Detection of Energetic Heavy Ions. *Nucl. Instrum. Methods*, 100:13–32.
- [Katz et al., 1972b] Katz, R., Sharma, S. C., and Homayoonfar, M. (1972b). The structure of particle tracks (Delta ray particle track structure theory for radiation dosimetry and biological cell response to heavy ions, fast neutrons, stopped pions and mixed radiation fields). *Topics in radiation dosimetry. (A 73-25420 11-14) New York, Academic Press, Inc., 1972,,* pages 317–383.
- [Kirby et al., 2010] Kirby, D., Green, S., Palmans, H., Hugtenburg, R., Wojnecki, C., and Parker, D. (2010). LET dependence of GafChromic films and an ion chamber in low-energy proton dosimetry. *Phys. Med. Biol.*, 55(2):417–33.
- [Klein et al., 2011] Klein, F. A., Greulich, S., Andersen, C. E., Lindvold, L. R., and Jäkel, O. (2011). A thin layer fiber-coupled luminescence dosimeter based on Al₂O₃:C. *Radiat. Res.*, 46(12):1607–1609.
- [Koizumi et al., 1996] Koizumi, H., Ichikawa, T., and Yoshida, H. (1996). Radiation chemistry in alanine irradiated with [gamma]-rays and ion beams. *Appl. Radiat. Isotopes*, 47(11-12):1205–1209. ESR Dosimetry and Applications: Proceedings of the 4th International Symposium.
- [Kojima et al., 1992] Kojima, T., Chen, L., Haruyama, Y., Tachibana, H., and Tanaka, R. (1992). Fading characteristics of an alanine-polystyrene dosimeter. *Nucl. Instrum. Meth. A*, 43(7):863–867.
- [Kojima and Tanaka, 1989] Kojima, T. and Tanaka, R. (1989). Polymer-alanine dosimeter and compact reader. *Nucl. Instrum. Meth. A*, 40(10-12):851–857.
- [Kraft et al., 1992] Kraft, G., Krämer, M., and Scholz, M. (1992). LET, track structure, and models. *Radiat. Environ. Bioph.*, 31:161–180.
- [Krämer, 1995] Krämer, M. (1995). Calculation of heavy-ion track structure. *Nucl. Instrum. Meth. B*, 105(1–4):14–20. Ionizing Radiation and Polymers.
- [Krämer et al., 2000] Krämer, M., Jäkel, O., Haberer, T., Kraft, G., Schardt, D., and Weber, U. (2000). Treatment Planning for Heavy-Ion radiotherapy: Physical Beam Model and Dose Optimization. *Phys. Med. Biol.*, 45:3299–3317.
- [Krushev et al., 1994] Krushev, V. V., Koizumi, H., Ichikawa, T., Yoshida, H., Shibata, H., Tagawa, S., and Yoshida, Y. (1994). Relation between track structure and LET effect on free radical formation for ion beam-irradiated alanine dosimeter. *Radi. Phys. Chem*, 44(5):521–526.

- [Kumazaki et al., 2007] Kumazaki, Y., Akagi, T., Yanou, T., Suga, D., Hishikawa, Y., and Teshima, T. (2007). Determination of the mean excitation energy of water from proton beam ranges. *Radiat. Meas.*, 42(10):1683–1691.
- [Lomax et al., 1999] Lomax, A., Bortfeld, T., Goitein, G., Debus, J., Dykstra, C., Tercier, P., Coucke, P., and Mirimanoff, R. (1999). A treatment planning inter-comparison of proton and intensity modulated photon radiotherapy. *Radiother. Oncol.*, 51(3):257–271.
- [Lühr et al., 2011a] Lühr, A., Hansen, D. C., Jäkel, O., Sobolevsky, N., and Bassler, N. (2011a). Analytical expressions for water-to-air stopping-power ratios relevant for accurate dosimetry in particle therapy. *Phys. Med. Biol.*, 56(8):2515–33.
- [Lühr et al., 2011b] Lühr, A., Hansen, D. C., Sobolevsky, N., Palmans, H., Rossomme, S., and Bassler, N. (2011b). Fluence Correction Factors and Stopping Power Ratios for Clinical Ion Beams. *Acta Oncol.*, 50(6):797–805.
- [Lühr et al., 2011] Lühr, A., Toftegaard, J., Kantemiris, I., Hansen, D. C., and Bassler, N. (2011). Stopping power for particle therapy: The generic library libdEdx and clinically relevant stopping-power ratios for light ions. *Int. J. Rad. Biol.*, 88(1):209–212.
- [Malinen et al., 2003a] Malinen, E., Heydari, M. Z., Sagstuen, E., and Hole, E. O. (2003a). Alanine radicals, Part 3: Properties of the components contributing to the EPR spectrum of X-irradiated alanine dosimeters. *Radiat. Res.*, 159(1):23–32.
- [Malinen et al., 2003b] Malinen, E., Hult, E. A., Hole, E. O., and Sagstuen, E. (2003b). Alanine Radicals, Part 4: Relative Amounts of Radical Species in Alanine Dosimeters after Exposure to 6–19 MeV Electrons and 0 kV–15 MV Photons. *Radiat. Res.*, 159:149–153.
- [Malinen et al., 2007] Malinen, E., Waldeland, E., Hole, E. O., and Sagstuen, E. (2007). The energy dependence of lithium formate EPR dosimeters for clinical electron beams. *Phys. Med. Biol.*, 52:4361–4369.
- [Marrale et al., 2007] Marrale, M., Brai, M., Gennaro, G., Triolo, A., Bartolotta, A., D’Oca, M. C., and Rosi, G. (2007). Alanine blends for ESR measurements of thermal neutron fluence in a mixed radiation field. *Radiat. Prot. Dosim.*, 126(1-4):631–5.
- [Marrale et al., 2011] Marrale, M., Longo, A., Spanò, M., Bartolotta, A., D’Oca, M., and Brai, M. (2011). Sensitivity of Alanine Dosimeters with Gadolinium Exposed to 6 MV Photons at Clinical Doses. *Radiat. Res.*, 175.

- [Martisíková and Jäkel, 2010] Martisíková, M. and Jäkel, O. (2010). Dosimetric properties of Gafchromic(R) EBT films in medical carbon ion beams. *Phys. Med. Biol.*, 55(18):5557–67.
- [Nichiporov et al., 1995] Nichiporov, D., Kostjuchenko, V., Puhl, J. M., Bensen, D. L., Desrosiers, M. F., Dick, C. E., McLaughlin, W. L., Kojima, T., Coursey, B. M., and Zink, S. (1995). Investigation of applicability of alanine and radiochromic detectors to dosimetry of proton clinical beams. *Appl. Radiat. Isotopes*, 46(12):1355–1362.
- [Ohno et al., 2001] Ohno, S.-i., Furukawa, K., Taguchi, M., Kojima, T., and Watanabe, H. (2001). An ion-track structure model based on experimental measurements and its application to calculate radiolysis yields. *Radi. Phys. Chem*, 60(4-5):259–262. International symposium on prospects for application of radiation.
- [Olko, 1999] Olko, P. (1999). Calculation of the Relative Effectiveness of Alanine Detectors to X rays and Heavy Charged Particles using Microdosimetric One-Hit Detector Model. *Radiat. Prot. Dosim.*, 84(1-4):63–66.
- [Olko, 2002] Olko, P. (2002). The microdosimetric one-hit detector model for calculating the response of solid state detectors. *Radiat. Meas.*, 35(3):255–267.
- [Olsen and Hansen, 1985] Olsen, K. J. and Hansen, J. W. (1985). Experimental data from irradiation of physical detectors disclose weaknesses in basic assumptions of the δ ray theory of track structure. *Radiat. Prot. Dosim.*, 13(1-4):219–222.
- [Olsen and Hansen, 1988] Olsen, K. J. and Hansen, J. W. (1988). On the Dose-Response Relationships Following the Irradiation of Amino Acids. *Radiat. Res.*, 116(3):547–549.
- [Olsen and Hansen, 1990] Olsen, K. J. and Hansen, J. W. (1990). The Response of the Alanine Dosemeter to Low Energy Protons and High Energy Heavy Charged Particles. *Radiat. Prot. Dosim.*, 31(1/4):81–84.
- [Olsson et al., 2002] Olsson, S., Bergstrand, E. S., Carlsson, Å. K., Hole, E. O., and Lund, E. (2002). Radiation dose measurements with alanine/agarose gel and thin alanine films around a ¹⁹²Ir brachytherapy source, using ESR spectroscopy. *Phys. Med. Biol.*, 47:1333.
- [Olsson et al., 1996] Olsson, S., Lund, E., and Erickson, R. (1996). Dose response and fading characteristics of an alanine/Agarose gel. *Appl. Radiat. Isotopes*, 47(11–12):1211–1217. SR Dosimetry and Applications: Proceedings of the 4th International Symposium.

- [Onischuk et al., 2010] Onischuk, V. A., de Boer, J., Levon, A. I., Maksimenko, V. M., Wurkner, M., Zaitov, V. R., and Bugay, O. A. (2010). Response of alanine and barium dithionate EPR dosimeters. *Health Phys.*, 98(2):412–6.
- [Onori et al., 1997] Onori, S., d’Errico, F., De Angelis, C., Egger, E., Fattibene, P., and Janovsky, I. (1997). Alanine Dosimetry of Proton Therapy Beams. *Med. Phys.*, 24(3):447–453.
- [Paganetti, 2009] Paganetti, H. (2009). Dose to water versus dose to medium in proton therapy. *Phys. Med. Biol.*, 54:4399–4421.
- [Palmans, 2003] Palmans, H. (2003). Effect of Alanine Energy Response and Phantom Material on Depth Dose Measurements in Ocular Proton Beams. *Technol. Cancer Res. Treat.*, 2(6):579–586.
- [Palmans et al., 2007] Palmans, H., Bobrovodsky, J., Durny, D., Gouldstone, C., Kovac, P., Martinkovic, J., Mozolik, M., Rosser, K., Sharpe, P., and Szöloes, O. (2007). Experimental Set-Up for Alanine Dosimetry in Protons below 18 MeV. Technical Report 3.
- [Palmans et al., 1996] Palmans, H., Seuntjens, J., Verhaegen, F., Denis, J., Vynckier, S., and Thierens, H. (1996). Water calorimetry and ionization chamber dosimetry in an 85-mev clinical proton beam. *Med. Phys.*, 23:643.
- [Palmans et al., 2002] Palmans, H., Symons, J. E., Denis, J.-M., de Kock, E. A., Jones, D. T. L., and Vynckier, S. (2002). Fluence correction factors in plastic phantoms for clinical proton beams. *Phys. Med. Biol.*, 47(17):3055.
- [Papanikolaou et al., 2004] Papanikolaou, N., Battista, J., Boyer, A., Kappas, C., Klein, E., Mackie, T., Sharpe, M., and Van Dyk, J. (2004). Tissue inhomogeneity corrections for megavoltage photon beams. Technical Report 85, AAPM Task Group.
- [Parodi et al., 2010] Parodi, K., Mairani, A., Brons, S., Naumann, J., Krämer, M., Sommerer, F., and Haberer, T. (2010). The influence of lateral beam profile modifications in scanned proton and carbon ion therapy: a Monte Carlo study. *Phys Med Biol*, 55(17):5169–87.
- [Paul, 2010] Paul, H. (2010). Recent results in stopping power for positive ions, and some critical comments. *Nucl. Instrum. Meth. B*, 268:3421–3425.
- [Paul and A., 2001] Paul, H. and A., S. (2001). An empirical approach to the stopping power of solids and gases for ions from ${}^3\text{Li}$ to ${}^{18}\text{Ar}$. *Nucl. Instrum. Meth. B*, 179:299–315.

- [Paul et al., 2007] Paul, H., Geithner, O., and Jäkel, O. (2007). The ratio of stopping powers of water and air for dosimetry applications in tumor therapy. *Nucl. Instrum. Meth. B*, 256(1):561–564.
- [PTCOG, 2012] PTCOG (2012). Hadron therapy patient statistics. http://ptcog.web.psi.ch/patient_statistics.html.
- [PTW Freiburg, 2005] PTW Freiburg (2005). Information on PTW Markus Chambers Type 23343 and Type 34045 (D273.200.0/2). Technical Note, Lörracher Str. 7, 79115 Freiburg - Germany.
- [Regulla, 2009] Regulla, D. (2009). Alanine Dosimetry—A Versatile Dosimetric Tool. In Dössel, O. and Schlegel, W. C., editors, *World Congress on Medical Physics and Biomedical Engineering, September 7-12, 2009, Munich, Germany*, pages 478–481.
- [Regulla and Deffner, 1982] Regulla, D. F. and Deffner, U. (1982). Dosimetry by ESR Spectroscopy of Alanine. *Appl. Radiat. Isotopes*, 33:1101–1114.
- [Rotblat and Simmons, 1963] Rotblat, J. and Simmons, J. A. (1963). Dose-response relationship in the yield of radiation-induced free radicals in amino acids. *Phys. Med. Biol.*, 7:489.
- [Sagstuen et al., 1997] Sagstuen, E., Eli, O., Haugedal, S. R., and Nelson, W. H. (1997). Alanine radicals: Structure determination by EPR and ENDOR of single crystals x-irradiated at 295 K. *J. Phys. Chem. A*, 101(50):9763–9772.
- [Sakama et al., 2005] Sakama, M., Kanai, T., Kase, Y., Komori, M., Fukumura, A., and Toshiyuki, K. (2005). Responses of a Diamond Detector to High-LET Charged Particles. *Phys. Med. Biol.*, 50:2275–2289.
- [Sbalzarini and Koumoutsakos, 2005] Sbalzarini, I. F. and Koumoutsakos, P. (2005). Feature point tracking and trajectory analysis for video imaging in cell biology. *J. Struct. Biol.*, 151(2):182–195.
- [Schaeken et al., 2011] Schaeken, B., Cuypers, R., Lelie, S., Schroeyers, W., Schreurs, S., Janssens, H., and Verellen, D. (2011). Implementation of alanine/EPR as transfer dosimetry system in a radiotherapy audit programme in Belgium. *Radiother. Oncol.*
- [Schaeken and Scalliet, 1996] Schaeken, B. and Scalliet, P. (1996). One Year of Experience with Alanine Dosimetry in Radiotherapy. *Appl. Radiat. Isotopes*, 47(11/12):1177–1182.
- [Schardt et al., 2010] Schardt, D., Elsässer, T., and Schulz-Ertner, D. (2010). Heavy-ion tumor therapy: Physical and radiobiological benefits. *Rev Mod Phys*, 82(1):383–425.

- [Schneider et al., 2006] Schneider, U., Lomax, A., Pemler, P., Besserer, J., Ross, D., Lombriser, N., and Kaser-Hotz, B. (2006). The impact of imrt and proton radiotherapy on secondary cancer incidence. *Strahlenther. Onkol.*, 182(11):647–652.
- [Scholz and Kraft, 1996] Scholz, M. and Kraft, G. (1996). Track Structure and the Calculation of Biological Effects of Heavy Charged Particles. *Adv. Space Res.*, 18:5–14.
- [Scholz and Kraft, 2004] Scholz, M. and Kraft, G. (2004). COMMENTARY: The Physical and Radiobiological Basis of the Local Effect Model: A Response to the Commentary by R. Katz. *Radiat. Res.*, 161:612–620.
- [Schultka et al., 2006] Schultka, K., Ciesielski, B., Serkies, K., Sawicki, T., Tarnawska, Z., and Jassem, J. (2006). EPR/alanine dosimetry in LDR brachytherapy—a feasibility study. *Radiat. Prot. Dosim.*, 120(1-4):171–175.
- [Sharpe, 2012] Sharpe, P. (2012). private communication.
- [Sharpe et al., 2009] Sharpe, P. H. G., Miller, A., Sephton, J. P., Gouldstone, C. A., Bailey, M., and Helt-Hansen, J. (2009). The effect of irradiation temperatures between ambient and 80° C on the response of alanine dosimeters. *Radi. Phys. Chem*, 78(7-8):473–475.
- [Sharpe and Sephton, 1999] Sharpe, P. H. G. and Sephton, J. P. (1999). Alanine Dosimetry at NPL - the Development of a Mailed Reference Dosimetry Service at Radiotherapy Dose Levels. Technical report. IAEA-SM-356/65.
- [Sigmund, 2000] Sigmund, P. (2000). Stopping power: wrong terminology. *ICRU News*, 1(17).
- [Sigmund, 2004] Sigmund, P. (2004). *Stopping of heavy ions: a theoretical approach*, volume 204 of *Springer Tracts in Modern Physics*. Springer.
- [Sigmund et al., 2005] Sigmund, P., Bimbot, R., Geissel, H., Paul, H., and Schinner, A. (2005). Stopping of ions heavier than helium. *Journal of the ICRU*, 5(1).
- [Sigmund et al., 2009] Sigmund, P., Schinner, A., and Paul, H. (2009). Errata and Addenda: ICRU Report 73 (Stopping of Ions Heavier than Helium).
- [Simmons and Bewley, 1976] Simmons, J. A. and Bewley, D. K. (1976). The Relative Effectiveness of Fast Neutrons in Creating Stable Free Radicals. *Radiat. Res.*, 65(2):197–201.
- [Sleptchonok et al., 2000] Sleptchonok, O. F., Nagy, V., and Desrosiers, M. F. (2000). Advancements in accuracy of the alanine dosimetry system. Part 1. The effects of environmental humidity. *Radi. Phys. Chem*, 57(2):115–133.

- [Snipes and Horan, 1967] Snipes, W. and Horan, P. K. (1967). Electron Spin Resonance Studies of Free Radical Turnover in Gamma- Irradiated Single Crystals of Alanine. *Radiat. Res.*, 30:307–315.
- [Sørensen et al., 2011] Sørensen, B. S., Overgaard, J., and Bassler, N. (2011). In vitro RBE-LET dependence for multiple particle types. *Acta Oncol.*, 50(6):757–62.
- [Spielberger et al., 2002] Spielberger, B., Scholz, M., Krämer, M., and Kraft, G. (2002). Calculation of the x-ray film response to heavy charged particle irradiation. *Phys. Med. Biol.*, 47:4107–4120.
- [Suit et al., 2010] Suit, H., DeLaney, T., Goldberg, S., Paganetti, H., Clasié, B., Gerweck, L., Niemierko, A., Hall, E., Flanz, J., Hallman, J., and Trofimov, A. (2010). Proton vs carbon ion beams in the definitive radiation treatment of cancer patients. *Radiother. Oncol.*, 95(1):3–22.
- [Tabata et al., 1972] Tabata, T., Ito, R., and Okabe, S. (1972). Generalized semiempirical equations for the extrapolated range of electrons. *Nucl. Instrum. Meth. B*, 103(1):85 – 91.
- [Tölli et al., 2010] Tölli, H., Sjögren, R., and Wendelsten, M. (2010). A two-dose-rate method for general recombination correction for liquid ionization chambers in pulsed beams. *Phys. Med. Biol.*, 55(15):4247.
- [Vestad et al., 2003] Vestad, T. A., Malinen, E., Lund, A., Hole, E. O., and Sagstuen, E. (2003). EPR dosimetric properties of formates. *Appl. Radiat. Isotopes*, 59:181–188.
- [Vestad et al., 2004] Vestad, T. A., Malinen, E., Olsen, D. R., Hole, E. O., and Sagstuen, E. (2004). Electron paramagnetic resonance (EPR) dosimetry using lithium formate in radiotherapy: comparison with thermoluminescence (TL) dosimetry using lithium fluoride rods. *Phys. Med. Biol.*, 49:4701–4715.
- [Virtanen, 2006] Virtanen, A. (2006). The use of particle accelerators for space projects. In *Journal of Physics: Conference Series*, volume 41, page 101.
- [Vörös et al., 2012] Vörös, S., Anton, M., and Boillat, B. (2012). Relative response of alanine dosimeters for high-energy electrons determined using a Fricke primary standard. *Phys. Med. Biol.*, 57(5):1413.
- [Waldeland et al., 2011] Waldeland, E., Helt-Hansen, J., and Malinen, E. (2011). Characterization of lithium formate EPR dosimeters for high dose applications - Comparison with alanine. *Radiat. Meas.*, 46:213–218.

- [Waldeland et al., 2010] Waldeland, E., Hole, E. O., Stenerlöv, B., Grusell, E., Safstuen, E., and Malinen, E. (2010). Radical Formation in Lithium Formate EPR Dosimeters after Irradiation with Protons and Nitrogen Ions. *Radiat. Res.*, 174:251–257.
- [Waligorski, 1988] Waligorski, M. P. R. (1988). A model of heavy ion detection in physical and biological systems. Habilitation.
- [Waligorski et al., 1989] Waligorski, M. P. R., Danialy, G., Loh, K. S., and Katz, R. (1989). The Response of the Alanine Detector After Charged-particle and Neutron Irradiations. *Appl. Radiat. Isotopes*, 40(10-12):923–933.
- [Waligorski et al., 1986] Waligorski, M. P. R., Hamm, R. N., and Katz, R. (1986). The Radial Distribution of Dose around the Path of a Heavy Ion in Liquid Water. *Nucl. Tracks Rad. Meas.*, 11(6):309–319.
- [Weber and Kraft, 1999] Weber, U. and Kraft, G. (1999). Design and Construction of a Ripple Filter for a Smoothed Depth Dose Distribution in Conformal Particle Therapy. *Phys. Med. Biol.*, 44(11):2765–2775.
- [Wenzl and Wilkens, 2011] Wenzl, T. and Wilkens, J. J. (2011). Modelling of the oxygen enhancement ratio for ion beam radiation therapy. *Phys. Med. Biol.*, 56(11):3251.
- [Weyrather et al., 1999] Weyrather, W. K., Ritter, S., Scholz, M., and Kraft, G. (1999). RBE for carbon track-segment irradiation in cell lines of differing repair capacity. *Int. J. Rad. Biol.*, 75(11):1357–1364.
- [Wieser et al., 1993] Wieser, A., Lettau, C., Fill, U., and Regulla, D. F. (1993). The influence of non-radiation induced ESR background signal from paraffin-alanine probes for dosimetry in the radiotherapy dose range. *Appl. Radiat. Isotopes*, 44(1–2):59–65.
- [Wilkens and Oelfke, 2004] Wilkens, J. and Oelfke, U. (2004). A phenomenological model for the relative biological effectiveness in therapeutic proton beams. *Phys. Med. Biol.*, 49:2811.
- [Wilson, 1946] Wilson, R. (1946). Radiological use of fast protons. *Radiology*, 47:487–491.
- [Zhao and Das, 2010] Zhao, L. and Das, I. J. (2010). Gafchromic EBT film dosimetry in proton beams. *Phys. Med. Biol.*, 55(10):N291–301.
- [Ziegler et al., 2010] Ziegler, J. F., Ziegler, M. D., and Biersack, J. P. (2010). SRIM—The stopping and range of ions in matter (2010). *Nucl. Instrum. Meth. B*, 268(11):1818–1823.

[Ziegler, J. F., 1977] Ziegler, J. F. (1977). *Handbook of Stopping Cross-Sections for Energetic Ions in All Elements*, volume 5 of *The Stopping and Ranges of Ions in Matter*. Pergamon Press, New York, USA.

Acronyms

APTG	Aarhus Particle Therapy Group iv
ATM	amorphous track model 45
CPP-SC	compound Poisson processes using successive convolution 74
CSDA	continuous slowing down approximation 12
CT	computer tomography 96
DKFZ	Deutsches Krebsforschungszentrum [German Cancer Research Center] 56
EPR	electron paramagnetic resonance (see ESR) 32
ESA	European Space Agency 53
ESR	electron spin resonance (see EPR) 20
FCF	fluence correction factor 15
FNTD	fluorescent nuclear track detector 56
FWHM	full width at half maximum 50
HCP	heavy charged particle 22
HF	high frequency 36
HIT	Heidelberg Ion-Beam Therapy Center 48
IAEA	International Atomic Energy Agency 48
ICRU	International Commission on Radiation Units & Measurements 9
IFA	Institut for Fysik og Astronomi, Aarhus Universitet [Department of Physics and Astronomy, Aarhus University] iv
IGK	ion/gamma-kill 74
IMRT	intensity modulated radiotherapy 2
LET	linear energy transfer 16
LINAC	linear accelerator 2
MC	Monte Carlo 59
MWPC	Multiwire Proportional chamber 48
NIST	National Institute of Standards and Technology 12

NPL	National Physical Laboratory	42
OER	oxygen enhancement ratio	16
OSL	optical stimulated luminescence	18
PMMA	polymethyl methacrylate	48
PTB	Physikalisch- Technische Bundesanstalt	49
PTW	PTW Freiburg GmbH	48
QA	quality assurance	48
RADEF	RADiation Effect Facility, Department of Physics, University of Jyväskylä	53
RBE	relative biological effectiveness	5
RDD	radial dose distribution	22
RE	relative effectiveness (η)	18
RED	response equivalent dose	20
AFM	atomic force microscopy	
Shield-HIT10a	Shield-HIT version 10a	58
SI units	International System of Units, [French: Système international d'unités]	70
SOBP	spread-out Bragg peak	3
TL	thermoluminescence	103
TLD	thermoluminescent dosimeter	18
TPS	treatment planning system	96
TST	track-structure theory	6
WEPL	water-equivalent path-length	48

List of Figures

1.1	Therapeutic window	2
1.2	Comparison of DDD's of different radiation types	3
1.3	Comparison of SOBPs for protons and carbon ions	4
2.1	Electronic stopping force in water	11
2.2	Schematic range	12
3.1	Schematic illustration of both RE definitions	19
4.1	100 MeV/u ^{12}C in water	23
4.2	Cylindrical iso-dose shell around an ion trajectory.	26
4.3	Extended target	28
4.4	Extended target dose vs. Hansen RDD	32
5.1	Structural formula of L- α -alanine	34
5.2	Zeeman effect	35
5.3	EPR-spectrum of an irradiated alanine sample	36
5.4	Extracted dose response data	40
5.5	Alanine saturation for different ions	41
5.6	Predicted signal fading in alanine	42
5.7	Dose response of NPL batch 65	43
5.8	Proton RE from literature	45
7.1	Setup for proton measurements	49
7.2	Alanine RE in proton beams	51
8.1	RADEF collimators	53
8.2	Lithium formate calibration	55
8.3	Detector setup at RADEF	57
8.4	Stopping force in pristine alanine and NPL dosimeter	58
8.5	Pellet geometry	60
8.6	AFM-picture of the edges of one alanine pellet.	60
8.7	Fluence gradient measured on a FNTD	61
8.8	Particle tracks in $\text{Al}_2\text{O}_3:\text{C,Mg}$	62
8.9	Signal stability of alanine irradiated at RADEF	64
8.10	RE of 9.3 MeV/u Xenon in alanine	64
8.11	Degraded energies	67

9.1	Comparison original code to re-implementation	71
9.2	Impact of a_0 on the RE	72
9.3	Impact of a_0 value	73
9.4	Determination of a_0 for lithium fromate	77
10.1	Crossing regime results	80
10.2	Stopping regime results	81
10.3	Stopping regime results	82
10.4	RE for different detector thickness.	83
10.5	Proton RE as function of the LET	84
10.6	Literature data for heavier ions	85
11.1	Impact of β	87
11.2	Saturation response towards xenon ions	90
11.3	Geometrical considerations for track overlap estimation.	91
11.4	Track overlap for 9.3 MeV/u Xe	92
12.1	Schematic drawing of the phantom.	96
12.2	RDD for helium and carbon ions with same LET	99
12.3	RE as a function of the LET	100
12.4	RE(LET) in carbon ion beams with data	101
12.5	Carbon ion SOBP measured with alanine pellets.	102
12.6	Proton SOBPs in alanine	104
12.7	RE in proton SOBPs in alanine	105
12.8	Carbon SOBPs in alanine	106
12.9	RE in carbon ion SOBPS in alanine	107

List of Tables

5.1	D ₃₇ values from different authors	38
5.2	Legend of Figure 5.8	44
8.1	Ions used for detector irradiation.	56
8.2	Degrader materials	56
8.3	FNTD fluence measurements	62
8.4	Measured and calculated particle ranges in Al ₂ O ₃	63
8.5	Alanine RE from high-LET measurements	65
8.6	Lithium formate RE from high-LET measurements	65
8.7	Uncertainty budget- RADEF experiment	68
10.1	Predicted signal fading	78
10.2	Color code for Figure 10.4	82
A.1	Relative effectiveness in carbon ion beams	113
A.2	Alanine RE in proton beams	114
A.3	Proton results for Section 12.1	115
A.4	Carbon ion results for Section 12.1	116
A.5	Overview over literature data	117
A.6	Comparison literature data and model calculations	118